Experimental Investigation of Cusp Magnetic Field assisted GTAW of Similar and Dissimilar Low Carbon Steels and AISI 304 Stainless Steel

A thesis submitted
in partial fulfillment of the requirements
for the degree of

Doctor of Philosophy

By

Kelli Durga Prasad

Roll No.-146103013

Department of Mechanical Engineering

Indian Institute of Technology Guwahati

Guwahati, India

July, 2023

Department of Mechanical Engineering
Indian Institute of Technology Guwahati
Guwahati-781039
INDIA

CERTIFICATE

It is certified that the work contained in the thesis entitled "**Experimental Investigation of Cusp Magnetic Field assisted GTAW of Similar and Dissimilar Low Carbon Steels and AISI 304 Stainless Steel**", submitted by **Kelli Durga Prasad**, Roll No. 146103013 to the Indian Institute of Technology Guwahati for the degree of Doctor of Philosophy has been carried out under our supervision in the Department of Mechanical Engineering, Indian Institute of Technology Guwahati. This work has not been submitted elsewhere for the award of any other degree or diploma.

Manas Das 20/07/23

Dr. Manas Das
Department of Mechanical Engineering
Indian Institute of Technology Guwahati
Guwahati-781039, Assam, India
Date: 20.07.2023

SPal 20/7/2023

Dr. Sukhomay Pal
Department of Mechanical Engineering
Indian Institute of Technology Guwahati
Guwahati-781039, Assam, India
Date: 20.07.2023

Declaration

I declare that this written submission represents my idea in my own words and where others' ideas or words have been included, I have adequately cited and refernced the original sources. I also declare that I have adhered to all principles of academic honesty and integrity and have not misrepresented or fabricated or falsified any idea/data/fact/source in my submission. I understand that any violation of the above will be cause for disciplinary action by the institute can also evoke penal action from the sources which have thus not been properly cited or from whom proper permission has not been taken when needed.

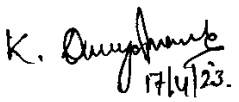

Date: 17/04/2023 Kelli
Durga Prasad

Roll No.: 146103013

Dedicated to

My Family

ACKNOWLEDGEMENT

I start this by thanking almighty for keeping me healthy and giving patience throughout my research work. I wish to express my deep gratitude to all those who have helped me in various ways directly or indirectly during the tenure of my research work at Indian Institute of Technoloyg Guwahati.

I express my sincere gratitude and appreciation to my supervisors **Dr. Manas Das**, Associate Professor, Department of Mechanical Engineering, Indian Institute of Technoloyg Guwahati and **Dr. Sukhomay Pal**, Professor, Department of Mechanical Engineering, Indian Institute of Technoloyg Guwahati for their valuable suggestions, resourceful guidance, inspiring instructions, active supervision and constant encouragement without which it would not have been possible for me to reach to this point. I feel privileged for having such personalitites as my supervisors during the research work at Indian Institute of Technoloyg Guwahati. I pray to almighty for their good health and success and wish they reach greater heights with time.

I also wish to thank to my doctoral committee members, Dr. Ganesh Narayanan, Dr. S. Senthilvelan, and Dr. Tamal Banerjee for their guidance, moral support and encouragement to my ideas in the subject as well as other areas of innovations. I must not miss the opportunity to thank all the Professors of Mechanical Engineering Department, Indian Institute of Technology Guwahati, whose motivation and timely help molded me in all possible forms.

I would also like to thank workshop superintendent Mr. N. K. Das and workshop technicians for their support in carrying out my work at central work shop. I am very much thankful to Mr. Gakul Das for his help to fabricate my experimental setup and workpieces. My sincere thank to laboratory superintendents Mr. S. Sarma, Mr. S. Ahmed, and Mr. J. Basumatary for their help and support. I would like to acknowledge Central instrument facility (CIF) of IIT Guwahati for kind assistance to carry out my research work.

I would like to thank my labmates at IIT Guwahati, Dr. Anupam Alok, Dr. Chandan Kumar, Dr. Anwesa Barman, Atul Singh Rajput, Manjesh Kumar, Abhinav Kumar, Ambrish Singh, Hari Narayan Singh Yadav, who maintained the research life cheerful.

I am also thankful to my friends at IIT guwahtai, Dr. E Satyanarayana, Dr. T Ramesh, Dr. Nagireddi Srinu, Dr. Mirzaul, Dr. J. Sunku Prasad, U K tarai, Dr. Vivek, Dr. Kaushik, Nagendra Prasad, Pilli Rajasekhar, Dr. Naik, Dr. Prudhi, Dr. Malli and my colleagues at AITAM, Dr. Dubba, Dr. Sreeramulu, Dr. Srihari, Raghuveer and Ms. Menaka for their valuable support, love and motivation throughout my research tenure.

I have missed some names in the above list and my sincere apologies are due in such inadvertent oversight.

Last, but not least, I am deeply indebted to my parents, grand parents, parents-in-law, and pinni for their sacrifices they have borne to ensure the fulfillment of my dreams. I would like to thank my wife and daughter (Lucky) for their support and love during my tenure at IIT Guwahati.

Kelli Durga Prasad

Abstract

Gas tungsten arc welding (GTAW) is a widely used welding technique for steels due to its ability to produce high-quality welds. GTAW is the best suitable method ranging between high heat input and high-density energy beam processes. GTAW process has better control over heat input with a minimum distortion, extends its application in various sectors such as aerospace and transportation. Unlike laser beam and electron beam welding of steels, the conventional GTAW process has lesser efficiencies and shallow penetrations at higher welding speeds. In this regard, cusp magnetic field assisted GTAW of steels is one of the most useful welding techniques to achieve a better weld bead aspect ratio at higher welding speeds.

The present study investigates the gas tungsten arc welding process for similar welding of low carbon steels (AISI 1008) and AISI 304 stainless steel (SS 304) plates, as well as dissimilar welding of low carbon steels and SS 304, with and without the influence of an external magnetic field. A specially designed fixture was developed to accommodate both the permanent magnet setup and the welding torch to generate the external magnetic field. The three primary process parameters considered in this study are welding speed, current, and magnetic field. This study examines the impact of cusp magnetic field on various weld bead features such as weld bead width, depth of penetration, average size of heat affected zone (HAZ), weld bead microstructure, and mechanical properties of the weldments. The quality of weldments is investigated via bead appearance under an optical microscope, energy dispersive X-ray spectroscopy analysis, metallographic characterization of weld bead and testing the weldment's mechanical properties using a Vickers microhardness tester and a universal testing machine. The weld bead microstructure is observed under optical microscope and their morphologies are compared using field emission scanning electron microscope (FESEM). Additionally, FESEM images of the fractured surfaces are analyzed to confirm different modes of fracture. Furthermore, a 3D finite element analysis was carried out to measure the magnetic flux density along the electrode tip and observed the similar results as compared to experimental methods with an acceptable error of 5-10%. The application of a cusp magnetic field resulted in notable differences in the macrostructure, microstructure, and mechanical properties.

From the experimental investigation, it is observed that penetration depth in base plate is primarily controlled by heat input on the work piece surface. The application of CMF results in the constriction of arc, leading to increased arc density and narrower weld beads, as well as larger depths of penetration were achieved in all weldments. Furthermore, stirring action in the

molten pool leads to higher convection rate resulting in lower peak temperatures in magnetic field assisted welds. In similar welding of SS 304, due to higher arc energy densities, the thermal energies attained in CMF assisted weld pool is higher and the cooling rate is little slower resulting in favorable conditions for precipitation of austenite. Also, resulted in decrease of columnar dendrites and transformation of columnar dendrites to equiaxed dendrites in the weldment. The decrease in heat affected zone thickness was also observed in all cases. The additional magnetic field caused a stirring action in the weld pool, which enhanced grain refinement and ferrite reduction. A better corrosion rate was achieved due to homogenous distribution of alloying elements in stainless steel weldments. In dissimilar welding, microstructure of magnetic field assisted weld region consists of fine austenite grains and equally distributed delta ferrite grains as compared to conventional GTAW. The ultimate tensile strength was increased with increase in heat input for both the cases. Under the influence of CMF, tensile strength of all weldments was increased as compared to conventional welds and exhibited much higher elongations than the welds without magnetic fields. Fracture morphology shows that an increase in heat input results in the formation of coarser and elongated dimples in both cases. Without the application of CMF, coarser dimples along with intergranular cleavage fracture were observed at lower welding speeds, and coalescence of finer and deeper dimples were observed in welds assisted by CMF.

CONTENTS

List of Figures

List of Tables

NOMENCLATURES

GTAW	Gas tungsten arc welding
LCS	Low carbon steels
ASS	Austenitic stainless steel
HAZ	Heat affected zone
LMF	Longitudinal-magnetic field
AMF	Axial-magnetic field
TMF	Transverse-magnetic field
CMF	Cusp-type magnetic field
TIG	Tungsten inert gas
DC	Direct current
EDX	Energy-dispersive X-ray
FZ	Fusion zone
OM	Optical microscope
FESEM	Field emission scanning electron microscope
XRD	X-ray diffraction
UTS	Ultimate tensile strength
YS	Yield strength
UTM	Universal Testing Machine
AF	Acicular ferrite
WF	Widmanstatten ferrite
FWHM	Full width at half-maximum
OCP	Open circuit potential
CNC	Computer numerical control
EDM	Electrical discharge machining
$\vec{A}$	Magnetic vector potential (Wb/m)
$\vec{B}$	Magnetic flux density (T)
H	Magnetic field strength (A/m)
M	Magnetization (A-m^2/Kg)
μ_0	Permeability of free space (Wb/A.m)
I_{corr}	Corrosion current density
E_{corr}	Corrosion potential

h	Depth of penetration
w	Bead width

Chapter 1 Introduction

1.1 Overview of gas tungsten arc welding process

Joining is a vital processing step as it requires to alleviate the complexity of manufacturing large structures. Welding is one of the permanent joining techniques which creates intricate items that are challenging to make as a single component. It is basically defined as the joining of two or more similar or dissimilar materials with the application of heat and with or without the application of pressure. Numerous welding techniques are employed on a big scale for various applications. Among them, the process which enjoy the status of the most preferred joining techniques in the industries is the fusion welding.

In fusion welding, two metals are fused together to form a continuous metallic bond. Fusion welds are produced by the application of intense heat and subsequent solidification of the molten metal. During the welding process, the interaction between the base metal and heat source results in a series of physical and chemical changes that determine the weld geometry, microstructure, and mechanical properties of the joint. Heat flux from the top surface and heat loss via conduction and radiation maintains the energy balance in the fusion welding process. The molten pool is driven by surface and body forces. The surface tension force acting on the top surface of the weld pool is the driving force of liquid metal movement and the volume of molten metal is driven by buoyancy force, and, also by the electromagnetic force when an electric arc is present. Furthermore, the ensuing heat transfer and fluid flow influence the cooling rate, weld pool size, shape, and the kinetics and magnitude of various solid-state transitions in the fusion zone and heat affected zone. The fusion welding processes are extensively used in industry for joining of various types of engineering materials from smaller to larger dimensional components [1,2]. This has been the major motivation behind the expansion of research in fusion welding processes.

Mechanical properties of the weldment are majorly influenced by the heat input, microstructure and solidification behavior of weld metal during the welding process [3,4]. Various fusion welding techniques are used to join engineering materials such as gas tungsten arc welding [5], metal inert gas welding [6], submerged arc welding [7], laser welding [8] and electron beam welding [9]. In welding of steels, low-energy-density arc welding methods such as submerged arc welding and metal inert gas welding can enhance the volume of austenite phase in the weld

joint owing to a slower cooling rate. Laser beam welding and electron beam welding are high energy density welding process featuring the major advantage of narrow heat affected zones and smaller deformations. However, these processes tend to reduce the percentage of austenite quantity in the weld due to faster cooling rate. Among these, gas tungsten arc welding (GTAW) is the best suitable method ranging between high heat input and high-density energy beam welding processes in terms of cooling rate. GTAW process has better control over heat input with a minimum distortion that extends its application in various sectors such as aerospace and transportation [10,11]. GTAW or Heliarc welding are other names for tungsten inert gas (TIG) welding. Russell Meredith, who perfected this procedure in 1941, is responsible for the latter name. This process uses a non-consumable tungsten electrode to create high-quality welds while shielding the arc with inert gases such as Ar, He, N_2, or their mixtures. GTAW process can be used without any filler material (autogenous) for welding plates up to a thickness of 3 mm in a single pass [5,12]. Instead of the above advantages, certain limitations of the process still exist such as: (1) The employed current is relatively low, leading to lesser weld efficiencies, (2) Power densities associated with GTAW are too low, (3) Minimal deposition rates and (4) At higher welding currents, the tungsten electrode may melt leads to inclusion of brittle tungsten in the weldment.

1.2 Motivation and preamble of the research work

Low carbon steel and stainless steels are the two most widely used materials in today's world for various industrial and commercial applications [4,9,13–17]. Autogenous GTAW process is best suitable for welding of low carbon steels (LCS) and stainless steels up to a thickness of 3 mm in a single pass. Similar and dissimilar welding of low carbon steel and stainless steels are carried out by various processes, since weldability of both these materials are relatively better.

In fusion welding of low carbon steel using GTAW, interaction of arc plasma with material leads to formation of weld pool. The molten metal in the weld pool experiences recirculation and flow of liquid metal which in turn effects the thermal cycles and the formation of weld pool geometry. Evolution of grain structure in the weldment has a major effect on the mechanical properties [18]. The grain structure is majorly influenced by the process parameters such as welding current, voltage and weld speed which in turn controls the heat input during welding. In GTAW of low carbon steels, increased heat input results in coarser grains that leads to reduction in mechanical properties of the weld [19]. Higher welding speed leads to reduction in heat input which in turn leads to partial penetrations. In low carbon steels, due to the presence

of acicular and polygonal ferrite the corrosion rates are on a higher side as compared to stainless steels.

In austenitic stainless steel (ASS) group the most popular and widely used member is SS 304. As these alloys are majorly used in manufacturing equipment for many industrial applications, joining and welding of such material are necessary. It is generally known that under equilibrium solidification, the microstructure of SS 304 is primarily constituted of austenite (γ-Fe). However, in a non-equilibrium rapid solidification situation, the high cooling rate results in an incomplete δ-γ transformation, and some metastable δ-Ferrite (δ-Fe) is unavoidably retained [20]. Also, the weld metal solidification structure in ASS is dendritic, with considerable quantities of elemental segregation, both of which cause a significant loss in weld mechanical properties when compared to base metal [21]. To achieve higher mechanical properties, the amount of δ-Fe produced during the welding process must be regulated. The proportion of δ-ferrite is mostly determined by the composition and the cooling rate during solidification. At higher heat inputs, cooling rate is relatively slow resulting in formation of coarser grain and the amount of δ-Fe is increased along with the increase in dendrite thickness and width in the weld region. Finer grains are generated at lower heat inputs, although this may led to a partial penetration [3].

Conventional arc welding is susceptible to the formation of coarse grains and intergranular Cr-rich carbides along the boundary of the heat affected zone (HAZ), deteriorating the joint's mechanical properties. In order to modify the microstructural and mechanical properties of the weld, the current research has been focused on hybrid welding process in attempt to improve the mechanical and metallurgical properties of the weld for the same amount of heat input, either by grain refining or altering ferrite volume.

For the same amount of heat input, deeper penetrations at higher welding speeds with better weld quality can be achieved by increasing the energy density of arc [22]. The energy density of the arc can be increased by constricting the traditional arc [23,24]. Therefore, the shape of arc plasma in GTAW is an important factor for the quality and efficiency of the welding. However, arc plasma is a unique phase that differs from the gas phase primarily due to its collective behavior. It is noteworthy to understand the basic phenomena of the arc plasma.

In autogenous GTAW processes, the arc plasma is a media, through which current flows and heat transfers to the work piece. By the application of an electric discharge between anode and cathode, generates an arc jet that consists of electrons and ions acting as charge carriers in the

direct current (DC) arc welding process. As per Ampere's law, a self-induced magnetic field is produced along the arc-jet in a counterclockwise direction. An electromagnetic pinch force is generated evenly towards the center of the cylindrical arc, according to Fleming's left-hand rule [25]. As a result, the flow of arc-jet is regulated by a combination of the electric field, magnetic field, and pinch effect as shown in **Fig. 1.1** Combination of fields in an electric arc. From the center of axis to the arc border, the magnetic field intensity decreases, resulting in the development of a bell-shaped arc as shown in Fig. 1.2. Due to this, a considerable loss in heat energy can be observed through advection, convection, and radiation, which in turn reduces the arc energy density. Energy density of the arc can be increased by constricting the arc, which in turn maximize the energy concentration to a minimum area on the work piece. As the arc plasma is an excellent electromagnetic conductor, several types of external magnetic fields have been tested to influence the welding thermal-force behavior.

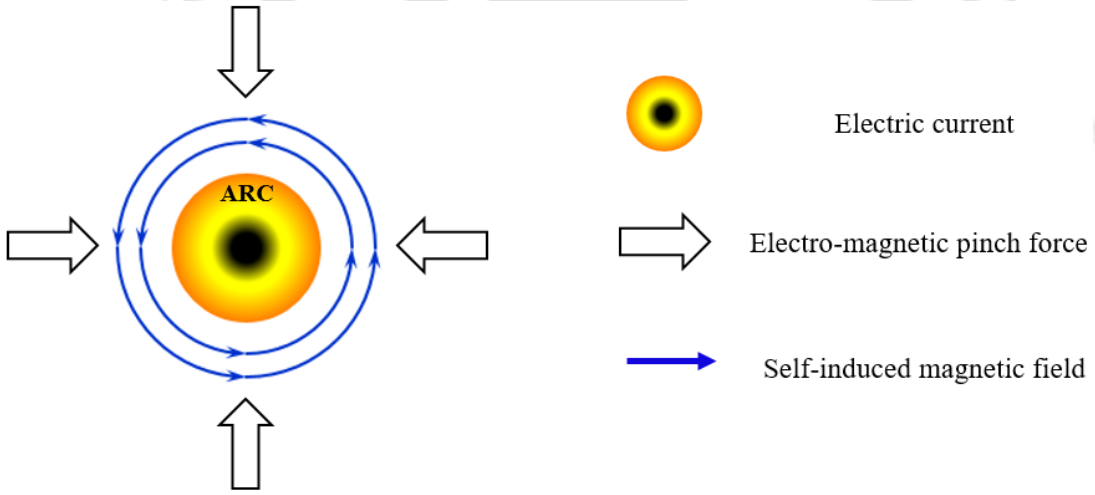

Fig. 1.1 Combination of fields in an electric arc

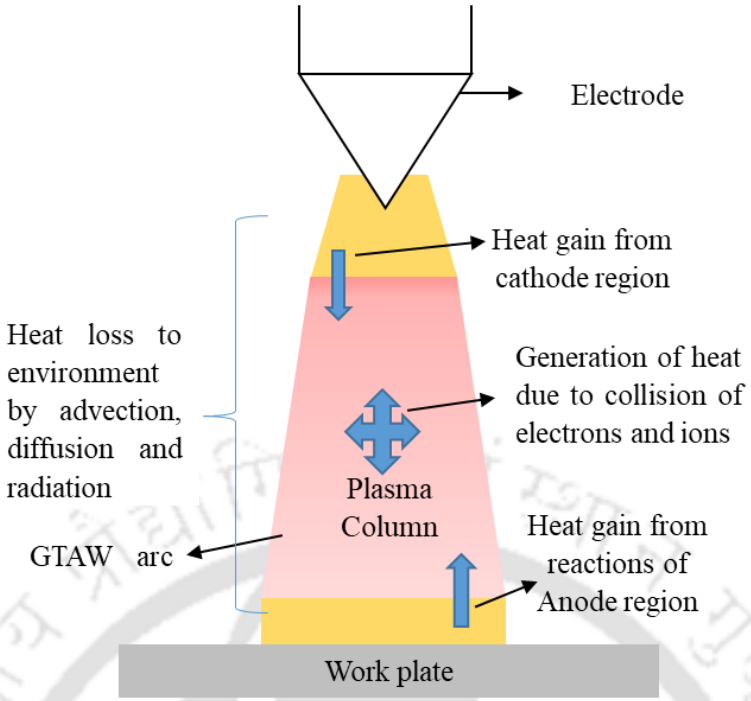

Fig. 1.2 Principle of heat distribution in an GTAW arc

Application of external magnetic field (EMF) during welding is one of the techniques to constrict the arc and to improve the energy density within the arc plasma. From this point of view, conventional studies have been conducted on controlling the arc plasma by EMF for effective welding. An electromagnet or a permanent magnet can be used to acquire the desired magnetic field configuration. While comparing to electromagnet, permanent magnet is more compatible and consumes no power with less space [25–28]. Various configurations of magnetic field were developed, and can be classified as, longitudinal-magnetic field (LMF) [29,30], axial-magnetic field (AMF) [27,28], transverse-magnetic field (TMF) [31,32] and cusp-type magnetic field (CMF) [25]. Furthermore, it has been claimed that the magnetic field can influence atom diffusion in materials, resulting in phase alteration, grain development, and recrystallization [33]. The arc rotates in AMF to improve the stiffness and arc plasma stability by following the Lorentz force action. The effect of AMF, on the other hand, was not substantial in a restricted plasma arc. To increase the quality of the surface, LMF and TMF were applied. In narrow gap welding, LMF was employed to deflect the arc and prevent sidewall fusion failure. Humps and undercuts are eliminated in high speed GMAW using TMF. However, there have been significant methods in controlling the process but still the knowledge available is insufficient in the application of cusp magnetic field in GTAW process. With the application of CMF to GTAW, the arc has been constrained and turned to oval shape which in turn increased the weld bead aspect ratio, improved weld appearance and welding speed

[23,34]. The CMF arrangement has a major impact on welding arc plasma properties and weld quality. Also, it is ideal for real-time application because, considering the contactless nature of the magnetic field and the exertion of electric current during welding is exceptionally tidy. Furthermore, in recent years, the controlling arrangement for magnetic field and electric current has advanced rapidly. The use of a magnetic field during arc welding has been shown to be a cost-effective and efficient way to improve the quality of welding process. Therefore, the relationship between the configurations of magnetic field to the welding arc and the properties of the weldment are addressed in the current research work.

In summary, the advanced welding technique offers the advantages of providing more welding stability, greater melting efficiency, and lower heat input while maintaining the same penetration. In this thesis, an attempt has been made to explore the possibility for the development of cusp magnetic field and its effect on the low carbon steel, SS 304 and dissimilar steel weldments. The analysis is carried out on comparative mode, which may be helpful for the future analysis on various materials. The weld quality is assessed by carefully controlling the process parameters. The present work is the major thrust on the application of cusp magnetic field to GTAW process to weld similar and dissimilar steels for heavy industries and ship building. To achieve this goal, the current study deals with the design and development of permanent magnets, experimental setup, selection of materials and thorough analysis of the weldments.

1.3 Contribution of the thesis

The major contributions of this research work are summarized as follows:

- A detailed experimental and 3D simulation of magnetic flux density distribution are carried out to find the customised shape and size of the permanent magnets.
- A dedicated fixture has been developed to assist the cusp magnetic field to GTAW process. The developed fixture is suitable for holding and positioning of magnets along the electrode holder.
- A detailed experimental investigation was carried out to analyse the effect of magnetic field and heat input on the weld microstructure and mechanical properties of low carbon steels, 304 SS and a dissimilar weld of LCS and 304 SS.
- With the application of CMF, improvement in weld depth of penetration and reduction in bead widths were achieved. Also, a homogenous distribution of alloying elements were observed in the weld zone as compared to conventional welds.

- Improved weld characteristics were achieved in the weldment while using cusp magnetic field assistance during GTAW.
- Experiments were performed in a potentiostat to analyse the corrosion resistance in 304 SS weldments using Tafel polarization curves.

1.4 Outline of the thesis

The theme of the thesis is majorly focused on the enhancement of metallurgical and mechanical properties of low carbon steel, SS 304, and dissimilar welding of low carbon steel and SS 304 using external magnetic fields. The current thesis is organized into eight chapters followed by references at the end. Overviews of those chapters are as follows:

Chapter 1 provides a brief overview of the GTAW process, emphasizing its drawbacks, advantages and applications. In addition, the objectives and contribution of the thesis are discussed herein.

Chapter 2 summarizes brief literature review on the GTAW of low carbon steels, SS 304 and dissimilar welding works carried out by previous researchers. Research work in the area of magnetic field assisted arc welding is discussed in detail. The research gap and objectives are also discussed in this chapter.

Chapter 3 discusses about the selection of magnets suitable for application in GTAW process. The details of numerical simulation performed to finalize the shape and position of magnets to produce cusp magnetic field along the arc is also discussed.

In chapter 4, the experimental procedures, preparation of specimens and development of experimental setup are discussed in detail. Also, summarizes the techniques and methods used to study the microstructure and mechanical properties of the weldments.

Chapter 5 presents the experimental investigation of both conventional and CMF assisted GTAW on low carbon steels. Mechanical and metallurgical properties measurement using XRD, FESEM and optical microscopic of the welded joint are also discussed in this chapter.

Chapter 6 deals with the welding of SS 304 plates using GTAW process under the influence of cusp magnetic field. Phase analysis, mechanical properties, metallurgical characteristics and corrosion resistance are discussed herein.

Chapter 7 deals with the effect of process parameters and magnetic field on dissimilar welding of low carbon steel and SS 304.

Chapter 8 provides the concise overview of the present study followed by the future research scope of the current study.

Chapter 2 Literature Review

2.1 Introduction

Gas tungsten arc welding (GTAW) or heliarc welding are other names for tungsten inert gas (TIG) welding. Russell Meredith, who perfected this procedure in 1941, is responsible for the latter name. In GTAW, an electric discharge can be generated by applying a voltage between two separated electrodes. Electric discharges are of three types namely dark discharge, glow discharge, and arc discharge and are mainly dependent on voltage and current through the arc plasma [35]. Among them, arc discharge is having both non-thermal and thermal regime which can be visible. Due to non-homogeneity in thermal plasma arc structure, the plasma region is sub-categorized into plasma core, cathode region and anode region. Thermal arc discharge can be applicable in material processing [36], cutting, melting and welding. And plasma is an electrically neutral gas having no specific shape until they are surrounded by a container. Plasma is a distinct phase which is separated from gas phase and can adopt a shape under the influence of magnetic field. Charged particles of neither bounded nor free interact with each other (Coulomb interaction) and strongly respond to electromagnetic fields. Also, the charged particles influence each other by inducing electric and magnetic fields. Due to the electric discharge, an electric arc is struck between tungsten electrode and work piece using a non-consumable electrode by passing an electric current. The electric arc produce temperatures of up to 20,000ºC and this can be used to melt and join metals. TIG welding uses non-consumable tungsten electrode to create high-quality welds while shielding the arc and weld zone with inert gas such as Ar, He, N2, or their mixtures. GTAW is one of the most widely used arc welding techniques in industries, such as transportation, aerospace and automobile sectors due to its better control over heat input and minimum distortion [10,11]. GTAW process has abundance of literature in reporting effects of various process parameters on GTAW of similar materials such as steels of different grades [3,37,38], Titanium alloys [39,40], and Inconel alloys [41–43]. The GTAW has found significant use in successfully joining dissimilar materials as well as similar materials.

The review of the available literature is carried out in order to interpret the research trend in accordance with the objectives of the current thesis. To summarize the salient results of the reviewed literature, this chapter is organized into various sections. Investigating the impact of process parameters on the GTAW of similar welding of low carbon steels (LCS) and stainless steels was the first step in the literature study. In this regard, section 2.2 is emphasised to report

the findings of numerous research works regarding the influence of welding current, weld speed, and shielding gas flow rate on GTAW process. This is followed by literature review of dissimilar welding of steels (LCS and stainless steels) in section 2.3. To improve the efficiency of GTAW process, various methods were used such as activated GTAW, and keyhole GTAW. The review of various auxillary methods are reported in section 2.4. The thrust area of this work is to develop a magnetic field within the arc region for effective welding. In this regard, Section 2.5 reports and discusses the relevant research carried out in this area. Finally, a brief summary of the findings is given in Section 2.6, and the research gaps identified during the literature review are discussed in Section 2.7.

2.2 Gas tungsten arc welding of similar steels (Low carbon steels, and SS 304)

The GTAW of steels of various grades depends on several factors, including the welding parameters, welding environment, filler metal, and base metal chemistry. Studies have shown that the choice of welding parameters, such as welding current, voltage, and welding speed, significantly affects the weld quality and properties.

During conventional GTA welding of mild steel, high welding currents and low welding speeds result in wider and deeper welds with higher dilution, leading to increased hardness and reduced toughness. In contrast, low welding currents and high welding speeds result in narrower and shallower welds with lower dilution, leading to lower hardness and increased toughness. Higher heat input results in a coarse grain structure in the weld metal, which in turn leads to a reduction in the strength of the weld [2]. Use of lower heat input, where possible, leads to the formation of smaller grains, which in turn improves the mechanical properties of the welds such as the ductility and fracture toughness in the case of steels [1]. Furthermore, it was observed that high heat input combined with low cooling rates led to the micro-segregation of alloying elements and the development of chromium-depleted zones. These conditions resulted in a decline in the mechanical properties of TIG joint [20]. Growth of grains at low welding speed is able to keep up with the moving heat source in an orderly and symmetrical manner. However, if the welding speed is increased, the shape of liquid isotherm is altered and the growing grains have to make sudden changes in direction at the weld center line in order to maintain continuity of the weld [1]. Abrupt changes in growth direction have been linked to the decrease in toughness of steel welds. Also, the formation of fine grains helps in reducing the susceptibility of the weld metal to solidification cracking during welding. With the

application of pulse current the welding defects such as humping and undercut were minimized in low carbon steel weldments. The tensile strength is increased by 12.5% and hardness by 12% at high speed welding and high mean current [44]. When subjected to high levels of heat input and low cooling rates, the austenite grains become finer, leading to the creation of polygonal ferrites with a smaller grain size at room temperature [19]. The heat-affected zone, which is produced as a result of peak temperatures and rapid cooling, exhibited a varied microstructure located adjacent to the fusion line. This heterogeneous microstructure was comprised of coarse-grained ferrite, acicular ferrite, and small pearlite colonies located at grain boundaries [45]. During medium-slow cooling rates, the weld metal exhibits the formation of large columnar grains of pro-eutectoid ferrite, accompanied by pearlite and side plates of Widmanstatten ferrite [46]. Eroglu, M. et al. [47] studied the effect of initial coarse grain size on microstructural and mechanical proeprties of the low carbon steel. At lower heat inputs of 0.5kJ/mm, the microstructure of HAZ consisting predominantly of martensite, bainite, pearlite and polygonal ferrite. By increasing the heat input to 1 kJ/mm, microstructures consisiting of grain boundary ferrite, martensite, Widmanstaten ferrite and pearlite. By further increasing the heat input, martensite does not seem to be present in microstructure due to complete diffusion of carbon at higher heat inputs. And maximum hardness values were achieved at lower heat inputs. There is an inverse relationship between the amount of heat input and the hardness of the material; as the heat input increases, the hardness decreases, and vice-versa.

In arc welding of SS 304 steels, the formation of Cr-rich carbides leads to the precipitation of these carbides near the grain boundaries, causing depletion zones of Cr in those areas. This phenomenon renders the material, vulnerable to localized forms of corrosion such as intergranular corrosion, intergranular stress corrosion cracking, and pitting corrosion, especially in chloride environments leading to premature failure during service life. To overcome this effect, Curiel, F. F. et al. [48] applied the axial magnetic field during welding to achieve chromium redistribution and reducing chromium depletion leading to increase corrosion resistance. In keyhole TIG welding of SS 316 L, the grain structure reveals the presence of austenite and δ-ferrite, in form of dendritic pattern. The heat-affected zone was observed to be quite narrow due to the growth of base metal grains near the fusion line was not substantial. However, the weld exhibited improved resistance to pitting corrosion compared to base metal due to homogenous distribution of alloying elements [12]. The microstructure of the weld metal and the local corrosion resistance of the piping weld joint are significantly influenced by the cooling rate during the welding process [49–52]. The corrosion resistance of the weld metal is often impacted by the quantity of acicular ferrite and grain boundary ferrite

present within it. Deen, K. et al. [53] investigated the microstructure and electrochemical corrosion behavior of a SA516 weld joint and found that the presence of an acicular ferrite structure resulted in lower corrosion resistance as compared to allotriomorphic and widmanstatten ferrite. Huang, H. et al. [50] investigated the impact of composition and microstructure on the electrochemical behavior of A516 steel weldment. They found that the volume fraction ratio of grain boundary ferrite to acicular ferrite is strongly correlated with the electrochemical behaviour of the weld metal. The quantity of acicular ferrite and grain boundary ferrite is significantly influenced by the welding heat input. Consequently, the correlation between welding heat input and the corrosion performance of the weld metal in diverse environments is crucial to establish. Hence, it is essential to identify the relationship between welding heat input and corrosion performance.

2.3 GTAW of dissimilar materials

Welding has become an essential aspect in numerous industries, including chemical, oil, and gas industries due to its ability to join numerous material combinations [54,55]. The increasing demand for new materials and their applications has led to more stringent requirements for joining dissimilar metals. However, the process of dissimilar joining is challenging due to the intricate mixing behaviours between two different materials within the molten pool. This complexity presents difficulties in analysing the evolution of microstructure and properties of the resulting weld. Therefore, it is crucial to prioritize a systematic investigation of the mechanism of microstructural evolution and its correlation with the properties of dissimilar welds.

Dissimilar welding of SS304 and mild steel are widely used in many potential applications like automobile, chemical, petrochemical, electrical, electronics, structural and ship building industries [55–59]. However, due to differences in carbon content and alloying elements many problems faced during conventional weld processes. The conventional fusion welding techniques can generate various defects like porosity, blow holes, hot cracks, rapid growth of grains, HAZ softening and alloying element segregation due to improper selection of filler materials, welding processes and its operating parameters [55,60]. Lundin, C D. et al. conducted experiments on welding of LCS and stainless steels, which revealed the presence of harmful carbides formed in the resultant weldment [61]. This results in decarburization and grain growth in the carbon steels heat-affected zone (HAZ), resulting in degradation of mechanical properties. In dissimilar welding of steels, the differences in the coefficient of

thermal expansion and thermal conductivity between LCS and stainless steels can pose problems during welding [62,63]. Stainless steel, being a poor conductor of heat, at higher heat inputs it tends to expand and contract significantly during welding. In contrast, LCS, being an excellent heat conductor, experiences quicker cooling and significant shrinkage during the joint cooling process. By increasing the current and decreasing the speed of weld. led to an increase in the heat input, resulting in the formation of coarse grains and an increase in the size of the fusion zone[64]. These variations in microstructure were primarily attributed to the disparities in the heat inputs and solidification rates of the weld metal. During the welding of stainless steel to carbon steels, there is a phenomenon of carbon diffusion that occurs from the material with a higher content of alloying elements towards the material that has a high affinity for carbon. In a study conducted by Xu et al. [65], the unmixed zone in GTAW of 439 ferritic SS to 308 L ASS was investigated and observed a distinct microstructure in the unmixed zone due to different liquidus temperatures and cooling rates. Thakare, J. G. et al. [66] observed the heterogeneity in terms of microstructure and mechanical properties in the weld zone. By conducting post weld heat treatment, the variations in mechanical properties were minimzed and the tensile strength of the weld joint was increased by an efficiency of 140%. Jahanzeb, N. et al. investigated the effect of microstructure on the hardness heterogeneity of dissimilar metal joints between 316L stainless steel and SS400 steel. The microstructure of the weld metal and heat-affected zone significantly influenced the hardness distribution in the joints. Furthermore, it was observed that the weld metal exhibited a higher hardness than the base metals, and the heat-affected zone of the SS400 steel side exhibited the highest hardness values among all regions. The microstructure of the weld metal and heat-affected zone significantly influenced the hardness distribution in the joints. Furthermore, it was observed that the weld metal exhibited a higher hardness than the base metals, and the heat-affected zone of the SS400 steel side exhibited the highest hardness values among all regions.

The problems faced during dissimilar welding of steels are solidification cracking, hydrogen cracking and formation of brittle products that may cause the failure of products before the expected design life [58]. Several studies have been conducted to examine the microstructure development in dissimilar welds of steels. However, to date, no comprehensive quantitative mechanism has been proposed to establish a clear relationship between the microstructure and the mechanical properties under the influence of external magnetic fields.

2.4 Auxillary energy aassisted GTAW

For the same amount of heat input, by increasing the energy density within the arc may result in higher welding speeds and larger depth of penetrations which in turn increase the efficiency of the welding process. Based on these findings, various methods have been developed to enhance the energy density of TIG welding arcs. These including keyhole TIG welding (K-TIG) [67–70], ultrasonic-TIG welding (U-TIG) [71–74], twin electrode TIG welding (T-TIG) [75,76], activated flux TIG welding (A-TIG) [77–79], high-frequency pulse TIG welding (H-TIG) [71,80] and magnetically influenced TIG welding (M-TIG) [81–83].

In 1997, Australia's Commonwealth Scientific and Industrial Research Organisation (CSIRO) introduced the keyhole TIG (K-TIG) welding technique. The K-TIG welding method uses a combination of high energy density, low current, and a keyhole formation mechanism to achieve deep penetration welding with a narrow weld bead. The microstructure formed in the weld zone is more homogenous and lesser deformations were achived as compared to conventional TIG welding [70]. Liu et al., proposed the integration of a sharp magnetic field into the K-TIG welding process as a means to enhance the welding arc performance, lowered the heat input, and ultimately improved the microstructure and properties of the resulting weld.

For solid state welding of metals, ultrasonic welding technology was invented in 1930s. Jiuchun et al. [84] reported that, the application of ultrasonic energy results in transverse compression of the arc, downward expansion of the high-temperature region, increased stiffness of the arc, and ultimately, an increase in the energy density of the arc. In the earlier literature, it is observed that the addition of ultrasonic energy during GTAW led to a refined microstructure of the weld joints and a decrease in the number of blowholes [71,73,74].

In T-TIG welding, multiple electrodes are used to share the current during welding, leading to an increase in the total current flowing through the arc space. This effective coupling of arcs reduces the cross-sectional area of the coupled arc, concentrating the arc energy in a smaller space. Moreover, the increase in total current enhances the electromagnetic contraction effect, resulting in an improvement in the arc energy [23]. Kobayashi. K et al. studied the effect of twin electrodes within a single torch on TIG welding of storage tanks. This method enabled a high deposition rate while reducing arc power in high current areas leading to reducing the time required for welding and improving the joint quality of the weld [23].

The Paton Electric Welding Institute (PWI) in Ukraine developed Activating flux TIG (A-TIG) during the 1960s. Before welding, the activating flux was either applied to both sides of the weld bead or introduced into the welding area using an automated powder feeding device. A-

TIG welding has found extensive application on materials such as stainless steel, aluminum alloy, and titanium alloy, since its invention [79,85,86]. An analysis of A-TIG welded joints was conducted by researchers to examine their microstructure, mechanical properties, and corrosion resistance. This analysis helped reveal the mechanism behind the microstructure refinement and increased penetration in A-TIG welded joints. The combined effect of centripetal Marangoni convection and arc plasma constriction acting as mechanism to increase the quality of weld [87]. Kumar, S. M. et al. studied the welding of AISI 321 steel using A-TIG, observed an increase in delta-ferrite in the weld metal as compared to parent metal leading to improved mechanical properties of the weldment [77]. By addition of fluxes in A-TIG welding, increases the arc voltage during welding resulting in increase of heat input. Due to higher heat inputs, the molten metal experiences higher peak temperatures thereby reducing the cooling rate resulting in increase of retained delta-ferrite in the weldment [88].

TWI firstly introduced the pulsed current in to GTAW for welding of thin plates. The high frequency pulsed current was later developd by USA to produce contraction in arc, enhancement of energy density and stiffness within the arc. The behaviour of arc, weld appearance and arc control was studied in detail by Qi, B. J et al. for high frequency pulsed current GTAW [80]. With the increase in frequency of pulsed current, the root radius of arc was reducing resulting in enhancement of arc force. This leads to the surface deformation of the material, and arc energy was concentrating resulting in narrower and deeper weld penetrations. Balasubramanian, V. et al conducted experiments and observed an equi-axed and finer microstructure with the application of pulsed current [89]. An increase in tensile strength and ductility of material was accompanied by grain refinement. With the application of pulsed current, the weld pool shape is changing continuously resulting in change of temperature gradients at solid-liquid interface. Due to this variations, newer grains gradually develop a favourable orientation. Although each individual grain grows only a short distance, the growth of numerous grains leads to the formation of a fine-grained structure.

An effective tool for controlling and increasing the energy density within the arc plasma is the magnetic field. Tse, H. C. et al. investigated the impact of magnetic field, laser power, weld speed, and field direction on the penetration depth and bead width of AISI 304SS [90]. A 7% increase in penetration depth was observed, while there was no change in bead width. The electron density of the plasma was found to be affected by the magnetic field. Lim, Y. C. et al. studied the effect of circular magnetic field (arc stirring) on grain structure refinement of GTAW weld beads made on Inconel [91]. They concluded that, grain detachment is the primary mechanism for grain refinement. And grain detachment can be achived using external magnetic

field to the weld pool. Guan, Zi Qi. et al. sudied the effect of magnetic field frequency on arc plasma and observed the compression in arc [92]. At frequency higher than 60 Hz, the arc shape is compressed, arc temp gradient and undercooling degree increases resulting in finer grains and improved mechanical properties than conventional welding.

From the above discussion, it is evident that during welding, arc energy density, heat transfer and fluid flow in the weld pool can impact factors such as weld pool geometry, temperature gradient, local cooling rates, and solidification structure, all of which can alter the microstructure and properties of the weldment. Table 2.1 provides the detailed auxillary welding methods and their mechnaisms in improving the arc energy densities including their applications.

Table 2.1 Auxillary energy assisted GTAW processes and their mechanism

Sl.No	Welding method	Mechanisms for improving the energy density of the arc	Applications
1	K-TIG	Constriction of arc	Welding of moderately thick plates at higher speeds
2	U-TIG	Increase in kinetic energy of the particle, thermal; compression	Welding at lower temperatures, welding of inorganic non-metallic materials
3	T-TIG	Coupled arc	Welding of thin plates at higher weld speeds, narrow gap welding
4	A-TIG	Arc constriction, energy transfer and thermal compression of arc	Welding of high strength steels, alloys and non-ferrous metals
5	H-TIG	Compression of the arc magnetically, increase in particle density	High quality welds
6	M-TIG	Constriction of arc using magnetic field	Welding of thick plates with narrower weld beads and higher depth of penetrations

2.5 Magnetic field assisted arc welding process

From the above discussion, it is evident that, all the auxillary energy assisted processes requires an external power supplies of higher voltages/frequencies, activated fluxes to enhance the energy density and to constrict the arc. But in case of magnetic field assisted welding process, magnetic field itself is enough to constrict the arc and to increase the energy density within the

arc. The advantages of magnetic field assisted welding are its low cost setup, constricted arc, arc stability and greater energy concentration.

Arc phenomena occur as an emerging result of interaction of various physical process and discharge regions. Also, Arc can be controlled using an external magnetic field which in turn produces better results. The combination of all above has been studied as a part of literature review.

According to fundamental physics, the welding arc, a flexible gaseous conductor, is sensitive to magnetic fields. The consequences of the welding arc's interaction with magnetic forces was initially observed by Seeker, P. E., and Guile, A. E [93]. Arc extinction in strong applied fields happens as a result of excessive direct ion disruption and symmetry in the plasma stream's velocity distribution [94]. In welding arcs, the ionisation is due to conduction in gas arcs which are generally caused by argon or helium. Schmidt, H. P., & Speckhofer, G. studied the influence of transverse magnetic field on the arc column and observed the column of arc is deflected by Lorentz forces. Two pairs of Helmholtz coils are used to generate the magnetic induction along the arc column [95]. Anders, A., & Yushkov, G. Y. investigated the effect of magnetic field on the kinetic energy of the ions in the plasma region of arc column. For a free expansion of arc in the absence of magnetic field, a decrease in the density is observed as a result of particle conservation. Both the ion and electron density decreases by many orders of magnitude as the plasma is expanding. Magnetic fields are frequently employed to enhance ion charge states, and it has been demonstrated that ions' kinetic energy may also be increased [96].

A conventional gas tungsten arc welding process undergoes substantial changes when an external longitudinal magnetic field is applied to it [97]. If a longitudinal (axisymmetric) magnetic field is applied parallel to the centreline of welding arc, results in annular flow of liquid metal in weld pool and produces a considerable changes in the fluid flow and heat transfer of the weld pool. It also influences the melting and solidification of the weld metal. This sort of magnetic field can control the crystallization process in the weld metal and also refines the grain size of the weldment. A number of grain refining techniques during solidification process has been introduced in 1980’s such as, electromagnetic stirring [98–100]. Impact of an axial magnetic field on the geometry and solidification structure of gas tungsten arc welds of bead on plate in austenitic stainless steel AISI 310 are studied by Ouden G Den, Vink WJP [101]. By the application of alternating magnetic field with a frequency of 5 Hz produced a symmetrical weld bead with a good appearance and a refined grain structure. By increasing the magnetic field frequency from 0 to 40 Hz, the cross-sectional area of the weld bead is increasing. Also, Penetration depth is decreasing in alternating magnetic field by

increasing the frequency of alternating magnetic field. Chen, Rong. et al. studied the benefits and effects of axial magnetic field on weld pool dynamics of dissimilar weld of steels and aluminum [102]. Axial magnetic field modified the appearance of weld bead and microstructure of weld by Lorentz force and thermoelectric magnetic force induced in the weld pool. Reduction in austenite grain size is observed. The suppression of diffusion of C and decrement of Gibbs energy of Fe, led to an increase in nucleation rate and decreasing of growth rate. Decrease in micro-hardness and increase in tensile strength is observed. Matsuda, F. et al. investigated the effect of electromagnetic stirring on refining of weld solidification structure on austenitic stainless steels [100]. Equiaxed dendrite zone is produced near the center of weld bead under the application of electromagnetic force. Fine grains were produced by increasing the magnetic frequency. García, M. A. et al. applied electromagnetic interaction of low intensity during welding of AISI 2205 duplex stainless steels using metal arc welding [103]. This process reduced the size of HAZ, limited the coarsening of ferrite grains (δ) and promoted regeneration of austenite (γ) in this zone. Due to electromagnetic interaction, electromagnetic stirring in the weld pool induced a grain refinement of the weld metal with a large formation of austenite during cooling. Mahajan, S. et al. studied the effect of mechanical arc oscillation on mild steel using GTAW [18]. Columnar grains were observed in traditional GTAW and fine equiaxed grains were observed in arc oscillated welds. And strength, ductility of the weld was increased due to reduction in grain size diameter. Weld metal hardness decreased due to increase in pro-eutectoid ferrite formation with absence of Widmanstatten ferrite in the weld metal and less coarsening of grains in HAZ due to increased cooling rate. Investigated the effect of magnetic field on hybrid laser-metal inert gas welding of SS 304 plate of 4 mm [104]. The joint strength was increased by 12% and tensile residual stresses were reduced. Also, grain refining and promotion of the phase transformation with the magnetic field were analyzed. Stirring effect caused by the interaction of internal induced magnetic field and external magnetic field led to refined grains and uniformity of element distribution. Nucleation rate was increased as well, which promoted the δ-γ transformation then resulted in a decreased volume of ferrite. An investigation was conducted on the impact of transverse mechanical arc oscillation during Tungsten Inert Gas (TIG) welding of Al-Mg-Si alloy. The study findings revealed that the grain structure in the weld metal was refined, resulting in enhanced mechanical properties [18]. Liu, Y.B. et al. studied the effect of axial magnetic field on copper-aluminum using arc welding and observed that, the joint strength is increased by 33% [105]. With additional electromagnetic force, the average heat input at joint interface is decreased and the growth of Al_2Cu layer was inhibited.

Also, the external magnetic field can be confined to a particular configuration using a set of permanent or electromagnets. This configuration helps in constricting the arc to a particular region as discussed below.

Liu, Zuming. et al. developed a cusp magnetic field device to generate magnetic field to improve the welding process and arc behaviour [83]. By constraining the arc from two opposite directions and elongating it in the other directions, the cross-sectional shape of the arc was transformed into an oval shape. As a result of this transformation, stable keyhole welding processes were successfully achieved. Baskoro, Ario Sunar. et al. developed various configurations of magnetic field around the GTAW electrode [106]. The power consumption was reduced by 11% in magnetic field assisted welding for parallel configuration of North-North-South-South with side deflection. Nomura, Kazufumi. et. al conducted bead on plate experiments for SS 304 plates [25], using cusp magnetic field assisted TIG welding. Analytically and experimentally, they observed the change of arc shape from circular to elliptical. This effect results in no humping on bead on plates during welding. Application of CMF to GTAW, the arc has been constrained and turned to oval shape which in turn increased the weld bead aspect ratio, improved weld appearance and weld speed [7, 13]. The CMF arrangement has a major impact on welding arc plasma properties and weld quality. The influence of an external AMF on 304SS weldments during laser-metal inert gas hybrid welding was investigated by Chen et al. [107]. Distribution of arc pressure on the workpiece is relatively more uniform under the influence of magnetic field [108]. The use of an appropriate magnetic field has enhanced grain refinement and tensile strength by 12% and reduced tensile residual stresses. When EMF is used during welding, it causes electromagnetic agitation to the molten metal, resulting in grain refining of the weld metal during solidification. In an austenitic 304SS, it also changes the kinetics of phase precipitation in HAZ [103]. Stirring effect produced by AMF resulted in decrement of thermal gradients and promoted the uniform skeletal ferrite and decreased the intensity of ferrite texture [17]. An increase in resistance to pitting corrosion was also observed [48]. Grain refinement and ferrite reduction were aided by an optimum magnetic field intensity, which boosted the impact toughness of the laser-MIG hybrid weld of SS 304 [16].

It is ideal for real-time application because, considering the contactless nature of the magnetic field and the exertion of electric current during welding is exceptionally tidy. Furthermore, the controlling arrangement for magnetic field and electric current has advanced rapidly in recent years. The use of external magnetic fields in welding has been shown to be a cost-effective and efficient way to improve the quality of welding process.

2.6 Summary

From literature survey it has been found that, weld aspect ratio and quality of the weld can be increased in GTAW process using external magnetic field. Several techniques were established to increase the penetration in work piece. Among all of them, arc constriction is the better solution to increase the penetration in work piece. Arc can be constricted using two processes namely, A-TIG welding process and application of external magnetic field either from electro-magnets or permanent magnet. Based on literature review, it is observed that magnetic field assisted welding is more suitable for high welding speed, deeper penetration, and high quality of welding.

By constricting the arc with the help of magnetic field would lead to a significant increase in current density of the arc thereby increasing the density of energy transferred to the base metal and the amount of electromagnetic pressure created by arc together produce deeper penetrations which can be utilized to weld thick materials.

Only a few literatures are available regarding the magnetic field assisted arc welding process. Among them, majority of the reported work are related to experimental in nature for GTAW where different configurations of the experimental setups are discussed. Also, very few experimental works have been carried out in constricting the arc. Also, work on the proposed area is not fully explored yet. The influence of process parameters on constricting the arc has to be studied to a full extent.

2.7 Gaps in literature

The aim of this literature review is to identify recent developments in the field of GTAW research. During the review process, several gaps were identified that could potentially enhance the GTAW process and benefit the user community. The following are the gaps that were observed during the review.

- Previous literature has not reported any findings on the development of an experimental setup for configuring magnetic fields around the GTAW electrode using permanent magnets.
- Most of the previous studies applied arc oscillations, transverse magnetic fields on the TIG welding of low carbon steels. Further investigation is required to study the effect of cusp magnetic field and evolution of its properties on the GTAW of low carbon steels.

- In the past literature, only bead on plate welding was conducted on SS 304 plates using cusp magnetic field. No further investigation was carried out on the properties of the weldment.

To the best of our knowledge, no study has been conducted to investigate the impact of cusp magnetic fields on the metallurgical and mechanical properties of TIG-welded low carbon steels

2.8 Research Objectives

The overall objective of the present work is quantitative understanding of the effect of cusp magnetic field on the mechanical and metallurgical properties of similar and dissimilar steel weldments. The detail objectives of the thesis are as follows:

- To develop a suitable custom-made permanent magnets setup for producing a cusp magnetic field during the GTAW process.
- To develop a 3D finite element model (FEM) to simulate the magnetic flux density distribution around the electrode.
- To study the effects of welding conditions on metallurgical properties of the fusion zone, heat affected zone, and base metal zone. Also, to investigate the relationship between the microstructures in the weld bead and variations in mechanical properties of the weldments.
- To investigate the effect of cusp magnetic field configuration on GTAW of low carbon steels under various process parameters settings.
- To study the effect of magnetic field on the morphology, phases present in the microstructure and mechanical properties of the weldment of SS 304 alloy.
- To determine the effect of cusp magnetic field on the corrosion behaviour of the weldment of SS 304.

Investigation and comparison of conventional and cusp magnetic field assisted GTAW of dissimilar materials i.e. low carbon steel and stainless steel, at different welding currents and welding speeds.

Chapter 3 Design and Development of CMF

3.1 Introduction

This chapter deals with the study on selection of permanent magnets used in the experimentation and their physical properties. Also, this chapter demonstrates the design and development of cusp magnetic field (CMF) using permanent magnets by 3D finite element modelling.

3.2 Selection of permanent magnets

The magnets which can generate a magnetic field without any application of external power source are called permanent magnets. Permanent magnets are of various types namely ceramic, AlNiCo, Samarium Cobalt (SmCo), Neodymium-iron-boron (NdFeB) and Injection molded. Of all the above SmCo and NdFeB are called rare earth magnets.

The most important parameters considered for selection of magnets are magnetic flux density, coercive force, BH max energy product and the operating temperature of magnets. Table. 3.1 represents the properties of various permanent magnets. Among them NdFeB-39H magnets are having the best properties but with less operating temperatures. In this study, the magnets are to be placed near the arc region and due to radiation effect we have observed a higher temperature on the magnet surface up to 150^0C in preliminary experiments. The operating temperature of magnet lies on the linear reversible demagnetization characteristic. If the operating conditions reach the maximum working temperature, it strongly influence the magnetic characteristic and may lead to magnetization loss in the magnet. Based on this criteria, SmCo, AlNiCo and ceramic magnets have been left for our selection. From the above three types, SmCo magnet has been finalized for our experiments due to its higher operating temperatures, maximum energy product and magnetic flux density including its coercive force.

Table 3.1 Different types of permanent magnets

Material	Grade	Br (Gauss)	Hc (KA/m)	BHmax (KJ/m^3)	Tmax (^{0}C)
NdFeB	39H	12,800	978	318	150
NdFeB	B10N	6,800	460	79.6	150
SmCo	**26**	**10,500**	**732**	**206**	**300**
AlNiCo	5	12,500	51	43.8	540
Ceramic	8	3,900	254	27.9	300
Flexible	1	1,600	109	4.8	100

SmCo magnets are having different types of grades depending upon the actual material property and the maximum energy product of the magnet material. Table 3.2 and 3.3 represents the list of various grades of the SmCo magnet.

Table 3.2 Different types of grades in SmCo (1:5)

Material	Grade	Br (Gauss)	Hc (KA/m)	BHmax (KJ/m^3)	Tmax (^0C)
Sm1Co5	SmCo16	8100-8500	620-660	110-127	250
	SmCo18	8500-9000	660-700	127-143	250
	SmCo20	9000-9400	676-725	150-167	250
	SmCo22	9200-9600	710-748	160-175	250
	SmCo24	9600-10000	730-770	175-190	300

Table 3.3 Different types of grades in Smco (2:17)

Material	Grade	Br (Gauss)	Hc (KA/m)	BHmax (KJ/m^3)	Tmax (^0C)
Sm2Co17	SmCo26	10200-10500	748-796	191-207	300
	SmCo28	10300-10800	756-812	207-220	300
	SmCo30	10800-11000	788-835	220-240	300
	SmCo26H	10200-10500	748-796	191-207	350
	SmCo28H	10300-10800	756-812	207-220	350
	SmCo30H	**10800-11000**	**788-835**	**220-240**	**350**

As per data given in Table 3.2 & 3.3, Sm2Co17 magnets with a grade of SmCo30H is considered for our experiments because of its maximum energy product and higher operating temperatures. The physical properties of the Sm2Co17 magnet are presented in Table 3.4.

Table 3.4 Physical properties of Sm2Co17 magnet

Grade	Density ($Kg/m^{3)}$	Magnetic flux density (Gauss)	Coercivity (KA/m)	BHmax (KJ/m^3)	Electrical resistivity (Ωm)	Operating temperature (^0C)	Curie temperature (^0C)
30H	8400	10800	788-835	220-240	0.8×10^{-6}	350	825

By using the magnets, CMF was generated and its principle was discussed in detail in section 3.3. The position of the magnets along the weld torch was shown in Fig. 3.1. Magnetic flux density was measured at the electrode tip using COMSOL® Multiphysics simulation software. Various measurements were taken on the electrode tip at certain heights (0, 1, 2.5, 3.5, 5 mm) from the base of the magnets.

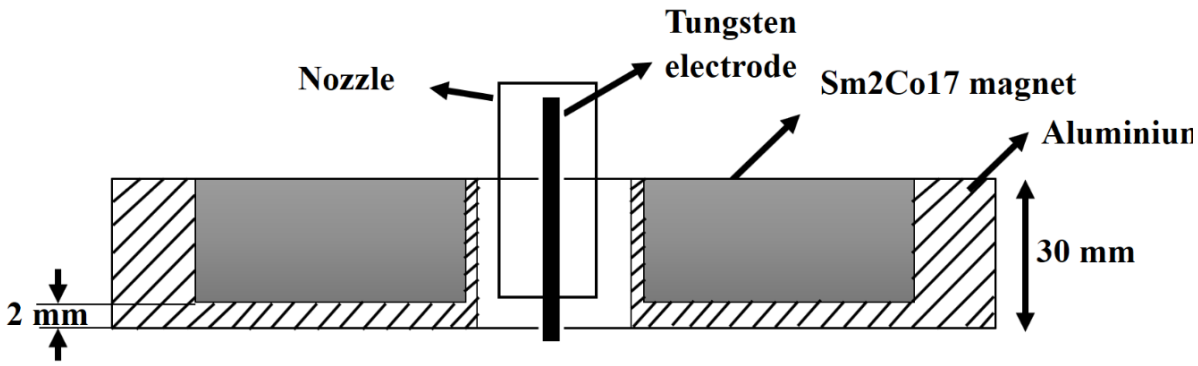

Fig. 3.1 Position of magnets along the weld torch

3.3 CMF principle

In the DC arc welding process, an electric discharge between the anode and cathode creates the arc jet, which comprises of electrons and ions serving as charge carriers, as illustrated in Fig. 1.2 in chapter 1. As per Ampere's law, a self-induced magnetic field is produced along the arc-jet in a counterclockwise direction. An electromagnetic pinch force is generated evenly towards the center of the cylindrical arc, according to Fleming's left-hand rule [25] as shown in Fig. 3.2a. As a result, the flow of arc-jet is regulated by a combination of the electric field, magnetic field, and pinch effect. From the center of axis to the arc border, the magnetic field intensity decreases, resulting in the development of a bell-shaped arc. Due to this, a significant thermal energy loss can be observed through convection, radiation and advection. The application of additional magnetic field around the arc axis will combine with the self-induced magnetic field of arc, resulting in a change in arc energy density.

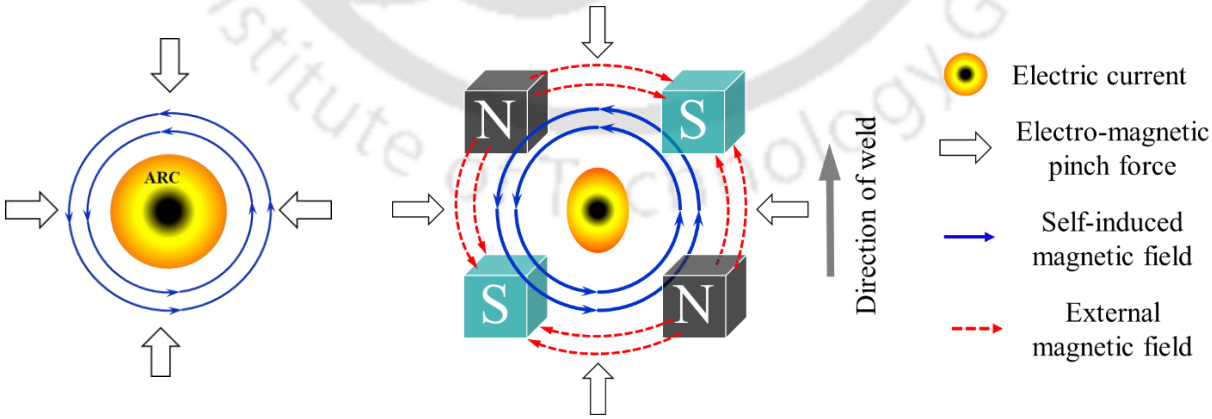

(a) (b)

Fig. 3.2 Arc shape: (a) without CMF, and (b) with CMF

The additional magnetic field is generated using four permanent magnets, which were arranged at an angle of 90° (N→S→N→S) to each other as shown in Fig. 3.2b. Due to the above arrangement, two inner poles of the magnet form a clockwise magnetic path and the other two poles form anti-clockwise magnetic path as shown in Fig. 3.2b. While combining the CMF with the arc magnetic field, the strength of the magnetic field is increased in anti-clockwise magnetic path. This is due to the direction of both the self-induced and additional magnetic field are in the same direction, resulting in constraining the arc in left and right sections. Meanwhile, the clockwise magnetic path and self-induced magnetic field are in opposite direction resulting in weakening of magnetic forces in top and bottom positions of the arc axis. This leads to the formation of an arc from circular to elliptical cross-section [7, 13]. This also leads to the compression of arc, which in turn increases the amount of energy holding per unit volume in the arc space. This compression effect decreases heat energy loss owing to radiation by restricting the dispersion of the arc. Additionally, it increases the quantity of energy transmitted to the anode area.

3.4 Model for cusp-type magnetic field

In the current study, external magnets are used to concentrate the electric arc formation at the required weld interface, so a magnetostatic simulation is needed to see the magnetic flux density distribution on the tip of the electrode. COMSOL® Multiphysics is used to simulate the magnetic flux density distribution produced by permanent magnets surrounding the electrode. In this FE analysis, a 3D geometric model consisting of four magnets and a circular electrode is made in the COMSOL software directly using its geometry tool. The magnetic field is applied in an X-Y plane perpendicular to the electrode axis. For measuring magnetic flux density at certain heights below the base of magnets surface, the electrode end point was moved from base of the magnets i.e., 0 mm to 5 mm towards the weld plate. The vector potential equation of Gauss law derives the magnetic field formed by a magnet and is given by

$$\vec{B} = \nabla \times \vec{A} \tag{1}$$

where A and B represent the magnetic vector potential (Tm or Wb/m) and magnetic flux density (T), respectively. A magnetically insulated boundary is created, indicating the zero field along the boundary,

$$n \cdot B = 0 \tag{2}$$

The Maxwell's equation used for the magnetic field of an permanent magnet is given by

$$\nabla . B = 0 \tag{3}$$

The magnetic field strength can be calculated using Eq. (4).

$$B = \mu_0 (H + M) \tag{4}$$

Where, M is magnetization (A-m2/Kg), H is magnetic field strength (A/m) and μ_0 is the permeability of free space (Wb/A.m).

Without the presence of a magnetic field,

$$\nabla \times H = 0 \tag{5}$$

V_m, a scalar magnetic potential can be defined from the following relation,

$$H = -\nabla \mathrm{V}_m \tag{6}$$

Inserting Eq. (4) and (6) in Eq. (3), the final relation is obtained as

$$-\nabla . (\mu_0 \nabla V_m - \mu_0 M_0) = 0 \tag{7}$$

During the magnetostatic simulation in the COMSOL software, a magnetic field with no current module is chosen to see the magnetic flux density distributions along the electrode tip. Maxwell's equation with no current is considered for the remnant flux density on the magnet poles.

3.5 Influence of CMF on electrode tip

The permanent magnets are positioned along the welding electrode, resulting in a horizontal magnetization direction. The magnetic flux ($\nabla . B = 0$) forms a complete loop around the magnets. The loop distribution is determined by the surface's orientation and the position of the magnet (North-South-North-South around the GTAW torch). The magnetic flux density distribution created by the magnets around the GTAW electrode tip at a height of 3.5 mm below the base of magnets was shown in Fig. 3.3. The legends in Fig. 3.3a, represents the magnetic field strength along the magnets and other represents the field strength within the area.

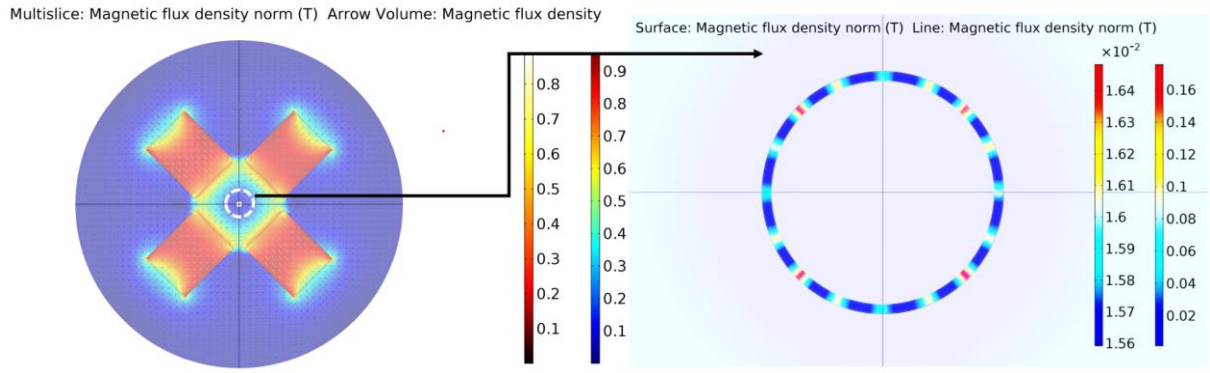

(a) (b)

Fig. 3.3 3D simulation of magnetic field distribution: (a) CMF in XY plane at 3.5 mm from base of magnets, and (b) Along its electrode tip

The magnetic field intensity on the tip of the electrode located at distance of 3.5 mm from the base of the center of magnets is depicted in Fig. 3.3b. At the tip of the electrode, minimum fields and maximum were observed at an interval of angle. These minimum and maximum field loop across the electrode tip is leading to expand the arc profile in top and bottom directions and constraining the arc in left and right directions as discussed in the previous section. Furthermore, the magnetic field strength is measured experimentally with a Gauss-meter at the tip of an electrode and observed the similar results as compared to numerical simulation with an acceptable error of 5-10%. The measured flux density values are presented in Table 3.5. The change in cross-section of the arc by an externally applied magnetic field during welding is due to electromagnetic forces in the plane normal to field lines.

Table 3.5 Magnetic flux density (in Gauss) at various points on electrode tip at certain heights below the base of magnets

Sl.	0 mm		1 mm		2.5 mm		3.5 mm		5 mm	
No	Exp	Num	Exp	Num	Exp	Num	Exp	Num	Exp	Num
1	512 ± 2	501	412 ± 2	398	319 ± 2	324	160 ± 2	158	144 ± 2	148
2	492 ± 2	475	394 ± 2	382	305 ± 2	318	168 ± 2	164	152 ± 2	162
3	510 ± 2	498	412 ± 2	396	319 ± 2	331	157 ± 2	157	145 ± 2	154
4	493 ± 2	462	394 ± 2	390	305 ± 2	324	159 ± 2	163	152 ± 2	171
5	512 ± 2	501	412 ± 2	398	319 ± 2	324	160 ± 2	158	144 ± 2	148
6	492 ± 2	475	394 ± 2	382	305 ± 2	318	170 ± 2	164	152 ± 2	162
7	510 ± 2	498	412 ± 2	396	319 ± 2	331	152 ± 2	157	145 ± 2	154
8	493 ± 2	462	394 ± 2	390	305 ± 2	324	154 ± 2	163	152 ± 2	171

3.6 Summary

This chapter provided the thorough procedure of magnets selection and development of CMF using the magnets and its principle. A 3D finite element analysis was carried out to calculate the magnetic flux density on the electrode. Flux density was measured at various heights of the electrode to know the effect of magnetic field on that position.

Chapter 4 Experimental Procedure

4.1 Introduction

This chapter broadly deals with the material selection, experimental setup, fixture used to generate the magnetic field and welding procedures during the experimentation. In the present study, welding current and weld speed are selected as process parameters. Every experiment is conducted with and without the influence of external magnetic field. After the completion of experiment, test samples are prepared from the weld plates for the analysis of macrostructure, microstructure and mechanical properties of the weldment. This chapter also outlines the different techniques used for testing and analyzing of the weld specimens.

4.2 Material preparation

To perform autogenous GTAW procedures, workpieces are prepared for optimum flatness and alignment prior to welding in order. For improved surface alignment, the mating edges are milled. After milling, the minor burrs left on the edges of the specimen are eliminated by fine filing followed by emery paper polishing to achieve a nearly zero gap in between the adjacent plates for the GTAW process. Also the welding surfaces are polished with emery sheets and then chemically cleaned with acetone to remove the grime, grease and oxide layer.

4.3 Material

The materials used in the experiment are low carbon steel (AISI 1008) and AISI 304 stainless steel (SS 304) plates. The workpiece dimension for similar welding of low carbon steel (LCS) and SS 304 is 120 mm × 65 mm × t mm^3, where t = 2.8 mm for low carbon steel and t = 3.1 mm for SS 304. The work piece dimension for dissimilar welding of LCS and SS 304 is 120 mm × 65 mm × 3 mm^3. All samples are welded in butt joint configuration

The chemical composition (wt.%) of the as-received base metal of low carbon steel (LCS) and SS 304 are measured using energy-dispersive X-ray (EDX) spectroscopy and are presented in Table. 4.1 and Table 4.2, respectively.

Table 4.1 Chemical composition of LCS (wt.%)

Element	Mn	Si	P	S	C	Fe
wt.%	0.3	0.2	0.1	0.1	0.1	99.3

Table 4.2 Chemical composition of SS 304 (wt.%)

Element	C	Cr	Ni	Mo	Mn	Si	P	S	Fe
wt.%	0.06	19.3	7.6	0.4	1.2	0.5	0.2	0.1	balance

In addition, mechanical properties of the examined LCS and SS 304 are shown in Table. 4.3 and Table. 4.4, respectively.

Table 4.3 Mechanical properties of LCS base metal

Mechanical property	Elongation (%)	Ultimate tensile strength (MPa)	Yield strength (MPa)	Hardness (HV)
Value	51.5 ± 6	385 ± 8	260 ± 7	118

Table 4.4 Mechanical properties of SS 304 base metal

Mechanical property	Elongation (%)	Ultimate tensile strength (MPa)	Yield strength (MPa)	Hardness (HV)
Value	28 ± 1	726 ± 2	267 ± 14	187 ± 4

In order to generate CMF during welding, four custom made samarium cobalt permanent magnets with dimensions of 25 mm × 20 mm × 15 mm were used. Table 4.5 lists the physical properties of the permanent magnets.

Table 4.5 Physical properties of Sm2Co17 magnet

Grade	**Density (Kg/m^{3})**	**Magnetic flux density (Gauss)**	**Coercivity (KA/m)**	**BHmax (KJ/m^{3})**	**Electrical resistivity (Ωm)**	**Operating temperature (^{0}C)**	**Curie temperature (^{0}C)**
30H	8400	10800	788-835	220-240	0.8×10^{-6}	350	825

4.4 Permanent magnet fixture

To generate the magnetic field along the GTAW arc, the magnets have to be placed at a proportionate height and at a distance from the electrode as discussed in the previous chapter. In this regard, the fixture is designed to hold the four permanent magnets in a circumferential manner and at a desired distance from the center of electrode. The magnets can be arranged inside the fixture such that the maximum magnetic field is available to converge the arc during welding. Magnet fixture with all magnets placed at their respective locations is shown in Fig. 4.1a. An aluminum block of 150X140X18 mm^3 has been used to develop the fixture. The fixture is machined using a CNC-milling machine as shown in Fig. 4.1b, by using G-code.

Aluminum is selected on the basis of its easy machinability and high thermal conductivity. Due to its higher thermal conductivity, the rate of heat transfer will be high which leads to a better cooling process throughout the fixture. During welding, some amount of heat will be transferred through the fixture base. As the magnets are having less curie temperatures, exposing them to higher temperatures during welding may cause loss in the magnetization of the magnets. To overcome this, the inner surface of the fixture is coated with a thermal barrier coating composed of Yttria-stabilised-Zirconia, which is ideal for remaining stable at higher temperatures.

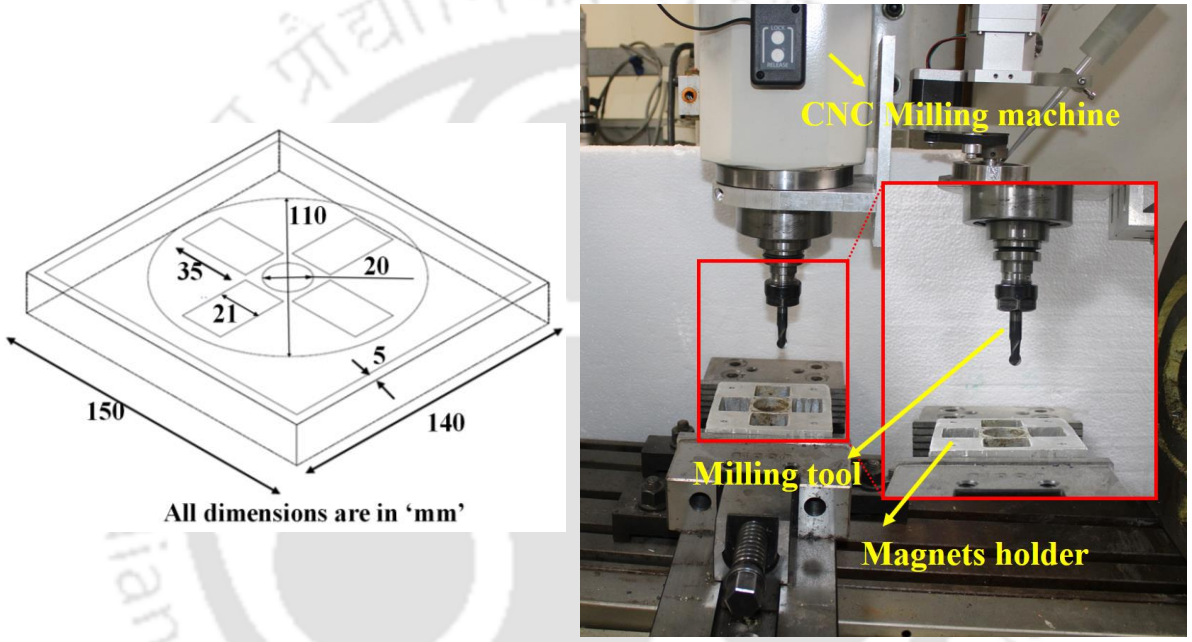

(a) (b)

Fig. 4.1 (a) Magnets arrangement in an aluminum fixture and (b) CNC milling machine

4.5 Experimental setup

The experimental setup used in this study majorly consists of two parts: (1) GTAW welding system, and (2) magnetic fixture along the GTAW torch. In autogenous GTAW process, the weld quality majorly depends upon the type of power source, cooling unit, welding speed; welding torch and its position with respect to the weld line, and precise motion control of the welding torch. In this experimentation, a MIGATRONIC PI PLASMA 350 welding machine is used to conduct welds for all the samples as shown in Fig. 4.2a. The DC power source is a constant current source with 5A-500A power supply. A tungsten electrode having 2% Thorium with a diameter of 2.4 mm is used. For shielding of plasma arc, argon gas of 99.95% purity is used in experimentation and the flow rate of argon gas is maintained at 12 L/min for all the

experiments. For conventional GTAW process, a fixture was developed as shown in Fig. 4.2b. The arc gap can be adjusted using the knob placed at the top of the fixture. The specimens were placed on the motorized pug machine and were clamped tightly in order to avoid the distortion of weld. As shown in Fig. 4.2c, a new fixture was developed to accommodate both the permanent magnet setup and the welding torch to generate the external magnetic field. As illustrated in Fig. 4.2 (d, e), permanent magnets were arranged in a circumferential manner to achieve a permissible amount of magnetic field to converge the GTAW arc during welding. The magnetic field strength is measured experimentally using a Gauss-meter at the tip of electrode which is located at a 3.5 mm away from base of magnets. Both simulated and experimental results are closely matched as shown in Table 4.6.

Table 4.6 Comparison of magnetic flux density at the electrode tip before welding

Magnetic flux density (in Gauss) at various points on electrode tip		
Sl. No	Experimental (avg.)	Numerical
1	160 ± 2	158
2	168 ± 2	164
3	157 ± 2	157
4	159 ± 2	163
5	160 ± 2	158
6	170 ± 2	164
7	152 ± 2	157
8	154 ± 2	163

During welding, the deflection of arc by the externally applied magnetic field is due to electromagnetic forces in the plane normal to field lines. Temperature have been measured using K-type thermocouples, which were located at a distance of 6.5 mm away from the joint centre line.

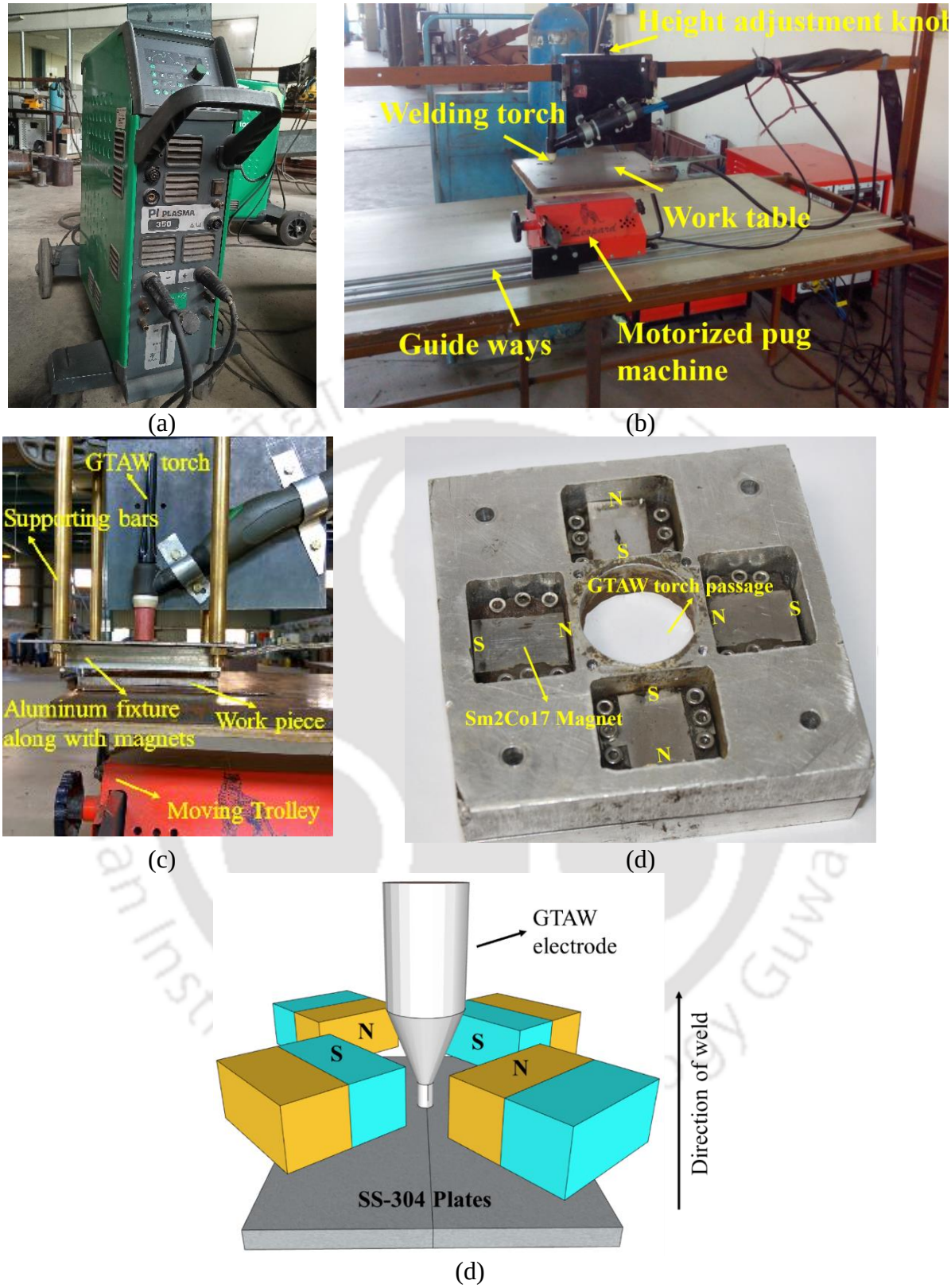

Fig. 4.2 (a) GTAW machine, (b) Work table, (c) Experimental setup, (d) Magnet fixture and (d) schematic diagram of magnets along the GTAW electrode

4.6 Measurement methodology

In order to ensure the quality of the welded samples, several measurement techniques are considered and are discussed in detail in the following subsections.

4.6.1 Macro and microstructural analysis

In GTAW process, interaction of arc plasma with material leads to formation of weld pool. The molten metal in the weld pool experiences recirculation and flow of liquid metal which in turn effects the thermal cycles and the formation of weld pool geometry. During this process, three regions in the weldment were formed namely, fusion zone (FZ), heat affected zone (HAZ) and unaffected base metal. In HAZ, ensuing heat transfer causes microstructural changes and fluid flow, kinetics and magnitude of various solid-state transitions causes microstructural changes in fusion zone. Evolution of grain structure in the weldment has a major effect on the mechanical properties. The grain structure is majorly influenced by the process parameters such as welding current, voltage and speed which in turn controls the heat input during welding. Hence, welded samples were then processed for metallographic characterization in accordance with ASTM: E3 and BSEN: 1321 standards.

The characterization of microstructure and macrostructure was done on metallographic specimens, which were cut from the welded specimens using wire-EDM, as illustrated in Fig. 4.3. The cross-sectional specimens were polished with silicon carbide abrasive papers up to 2000 grit size, followed by Alumina (0.2 µm) polishing and etching. For low carbon steel, 4% HNO_3 nital reagent is used and samples were etched in the solution for 20 seconds. And, 304 SS polished samples were etched using an etchant consisting of 15 mL HCL acid, 5 mL HNO3 and 10 mL Glycerol for 200 seconds.

The weld bead geometry, such as depth of penetration (h), bead width (w), microstructure, HAZ width and grain size at various locations are characterized using optical microscope (OM). The specifications of OM are presented in Table 4.7. The morphologies of the welded joints were examined using FESEM and the specifications of the machine are listed in Table 4.7. To establish the mode of failure in tensile specimens, the fracture morphology of the joint was examined using a Zeiss Sigma-FESEM. EDX analysis was used to categorize different phases and elemental quantities in the weld joint. It was performed along the fusion zone and HAZ, respectively. Also, to determine and quantify the phases in the weld, XRD is a distinctive method to analyse the crystallinity of a compound. Hence, XRD analysis was performed using

CuK_{α} irradiation at a scan rate of 10° per minute between $30° \leq 2\theta \leq 100°$ on fusion zone and HAZ. Intensity of the peak indicates the type of phase present in the weldment and its composition. Atomic distribution of atoms in the lattice determines the level of intensity. Phase identification of a specimen is determined by comparing experimental results to standard reference patterns.

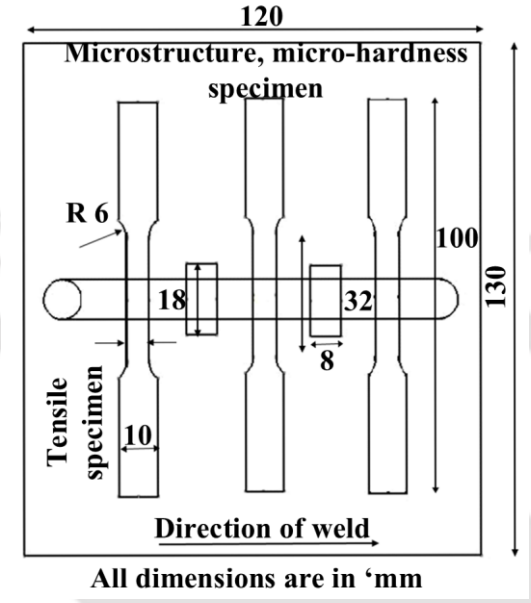

Fig. 4.3 Scheme for tensile and metallurgical samples extraction

4.6.2 Vickers micro-hardness test

The purpose of every weld is to produce a structure that is up to the challenges of its intended use. To know the performance of the weld, the best way is to assess the weld mechanical properties. Vickers micro-hardness test is one of the prominent test to evaluate the characteristics of the weldment. A material's hardness value is not a distinctive characteristic, but, if two materials have different hardness values indicating that both the materials are not alike. Testing the hardness of a component is a reliable approach to determine the performance and survival of the weldment in their specific working environment and its applications. Welded samples hardness values are affected by the presence of several phases and the subsequent development of their microstructure during welding. In HAZ, the hardness values indicate the weld susceptibility to crack.

In the current work, Vickers micro-hardness (Make: Buehler and Model: Micromet-2101) machine with a square base pyramid shaped diamond is used for testing the hardness of the weld. Before conducting hardness test, the specimen was polished and etched as discussed in previous sub-section. Hardness was measured at a depth of 1 mm from the top surface along

the unaffected base metal, HAZ followed by fusion zone, HAZ and unaffected base metal. A minimum spacing between two indentations was maintained based on ASTM standards. At room temperature, hardness test was conducted with an indentation dwell time of 15 second with a constant load of 500 gf.

4.6.3 Tensile test

As discussed in previous sub-section, evaluating the mechanical properties of a weldment determines the performance of the weld structure. Tensile test, is also one of the most significant test to evaluate the ultimate tensile strength (UTS), yield strength (YS) and elongation of the weld joint as compared to base metal.

To evaluate the mechanical properties of the joint, transverse tensile specimens were prepared accordingly to ASTM-E8 standards, as shown in Fig. 4.3. INSTRON universal testing machine was used to conduct the tensile tests at 1 mm/min strain rate. An extensometer with a gauge length of 25 mm was used to measure elongation during the tensile test. A portion of the gauge length is polished using silicon carbide abrasive paper up to a grit size of 600. Three samples were tested for each heat input condition, and the average tensile properties were presented. Three mechanical properties such as Ys, UTS and percentage elongation were determined from each test condition.

4.6.4 Grain size measurement

The grain size is measured in HAZ for all the welds using line intercept method. An optical microscope is used for micrographic image.

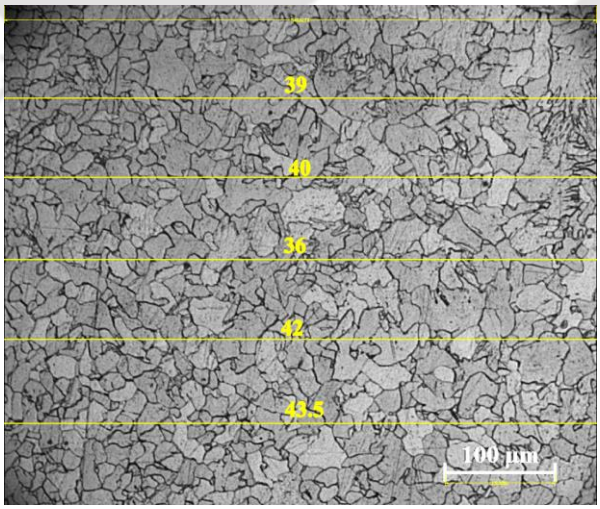

Fig. 4.4 Grain size measurement using line intercept method

A random of five horizontal test lines are drawn along the micrographic image. On the test line, intersection of the grain boundaries with test line or the number of grains intercepted with the test line are counted which is later used for grain size measurement as per ASTM E 112-13 standard. For representation purpose, one analysed sample was shown in Fig. 4.4.

4.6.5 Corrosion test

For corrosion test, the test specimens were cut from the welded plate along the weld line majorly consisting of fusion zone and HAZ. A 13 mm^2 circular specimens were prepared and grounded on both top and bottom of weld bead using emery papers up to a grit size of 2000 to achieve mirror finish as shown in Fig. 4.5a. A standard three electrode system and a potentiostat were used for polarization test as shown in Fig. 4.5b. In this test, the working electrode was the surface of the circular specimen, the reference electrode was silver/silver chloride (Ag/AgCl) and counter electrode was a Platinum wire. While conducting experiments, to avoid the external perturbations the Faraday shield was used to preserve the corrosion cell. Once the open circuit potential (OCP) attains the stable value, polarization test was conducted. In polarization test, the potential is applied from -500mV to +500 mV at a scan rate of 1 mV s^{-1} to attain the anodic branch. Naturally aerated electrolyte solutions were used for all the experiments.

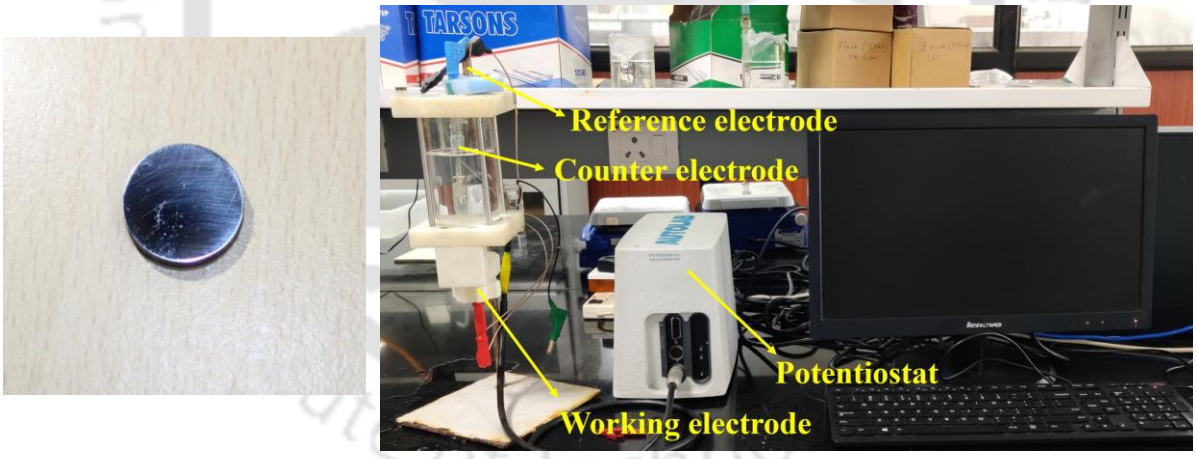

(a) (b)

Fig. 4.5 (a) Corrosion test specimen, and (b) Potentiostat experimental setup

Machines or equipment used in this research work are listed in Table 4.7 along with their make and model including specifications.

Table 4.7 Specifications of equipment's/machines used for welding and testing

Equipment/Machine	Make & Model	Specifications
GTAW	MIGATRONIC,	• Current range: 5-500A (GTAW)

	PI Plasma 350	• Duty cycle 60 %: 500A/30V
Dynamic Universal Testing Machine (UTM)	Instron, UK 8801J4051	• Mode of control: elongation rate, load hold, load rate, strain rate • Hydraulic pump capacity: 25 L/min • Method of testing: Position and load control • Capacity: ± 100 kN, • Actuator displacement: 0 to ± 75 mm
Optical Microscope (OM)	Carl Zeiss Axiotech, 100HD, 3D	• Magnification: 500X – 5 kX • Camera: In built Axiovision software with Axio-cam • Measuring system: 3 axis table movement • Binocular phototube (20°/23)
Hardness tester	Buehler, Micromet-2101	• Indentation force:1, 10, 50, 100, 300, 500, 2000 g force • Dwell time: 5 to 60 seconds
FESEM	Zeiss, Sigma	• Magnification range: 300X to 1000 kX • Specimen chamber: 270mm height, 330 mm inner dia • Movement: 125 mm in XY plane, 50 mm in Z plane • Chamber detectors: Inlense, SE-2, NEBSD
XRD	PANalytical, X-pert	• Minimum step size: 0.0001° • Direct optical positioning with 3 kW generator • diffracted beam and pre-fix incident
EDX	Zeiss, Gemini 300	• Magnification: 10X to 200 kX • Chamber detectors: Inlense, SE-2, NEBSD • Accelerating voltage: 0.02 kV to 30 kV
Wire-EDM	ECO-32	• Maximum process range: 320 mm×400 mm • Maximum cut thickness: 400 mm
Potentiostat	Metrohm Autolab, PGSTAT 204	• Potential range: -10V to 10V • Compliance voltage range: ±20 V

Chapter 5 Experimental Investigation of Cusp Magnetic Field Assisted GTAW of Low Carbon Steel

5.1 Introduction

In this work, magnetic field-assisted autogenous gas tungsten arc welding (GTAW) of 2.8 mm thick low carbon steel has been studied. The external magnetic field was generated by custom made rectangular shaped samarium cobalt permanent magnets which were arranged in a manner to generate a cusp-type magnetic field (CMF). The impact of CMF on the weld bead geometry, morphology and microstructural evaluation of the weld joints were examined prudently using optical microscope, Field-emission scanning electron microscope and X-Ray Diffraction technique and compared with the conventional GTAW process. Mechanical properties such as ultimate tensile strength and hardness values were characterized and analysed. Fractured surface morphology of the tensile specimen was analysed using FESEM. The experimental results exhibited that the CMF assisted GTAW produce joints with better mechanical and metallurgical properties compared to conventional GTAW.

5.2 Experimentation

The process parameters used in this study along with weld bead width (w) and depth of penetration (h) for all the experiments are shown in Table 5.1. All experiments were conducted with and without the influence of CMF for same process parameters settings and the samples were prepared for characterization as per the steps discussed in chapter 4.

5.3 Results and discussion

5.3.1 Effect of CMF on weld bead

The top surface appearance of the weld bead for both, with and without external magnetic field at various welding conditions are shown in Fig. 5.1. All the samples are silvery and bright in appearance indicating a good weld bead. The quality and dimensions of the weld bead are related to the process parameters as shown in Table 5.1. Figure 5.1 (a, c and e) and (b, d and f) shows the weld bead formed without and with the application of CMF to the arc, respectively. From Table 5.1, in both the cases, while increasing the welding current, the bead width is increased.

Table 5.1 Process parameters and geometry of weld bead

Test case	Current (A)	Welding speed (mm/s)	Heat input (kJ-mm^{-1})	CMF	w (mm)	% decrease in w	h (mm)	% increase in h
Exp-1	160	3	0.43	No	8.38	3.52	2.26	6.50
				Yes	8.07		2.41	
Exp-2	165	3	0.45	No	9.27	2.74	2.78	0
				Yes	9.21		2.78	
Exp-3	160	3.5	0.37	No	7.95	6.15	2.20	18.98
				Yes	7.46		2.62	
Exp-4	165	3.5	0.39	No	8.14	5.93	2.72	1.78
				Yes	7.66		2.77	
Exp-5	160	4	0.32	No	7.49	1.26	2.16	29.13
				Yes	7.39		2.79	
Exp-6	165	4	0.34	No	7.88	4.86	2.28	21.94
				Yes	7.50		2.78	

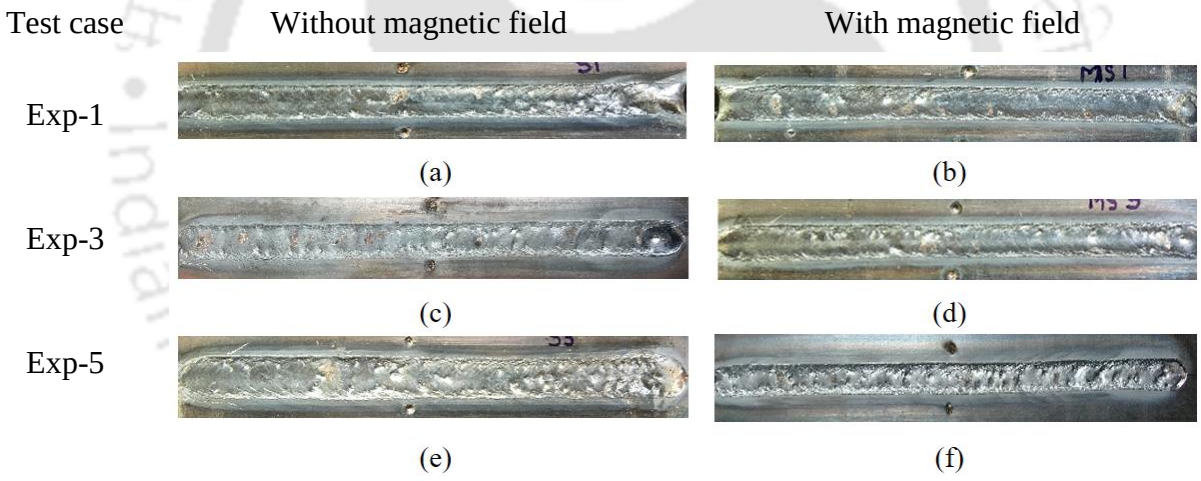

Fig. 5.1 Weld bead appearance at heat input of (a-b) 0.43 kJ-mm^{-1}, (c-d) 0.37 kJ-mm^{-1}, (e-f) 0.32 kJ-mm^{-1}

Higher values of arc current lead to more heat input per unit length at a fixed welding speed. Hence, larger volumes of base metal are being melted resulting in increase of bead width. During the application of cusp-type magnetic field, there is a significant amount of decrement in the bead width and an increment in the depth of penetration, as shown in Fig. 5.2. A maximum of 6.15 % reduction in weld bead width and 29.13% incerment in depth of penetration were observed in Exp-3 and Exp-5, as shown in Table 5.1.

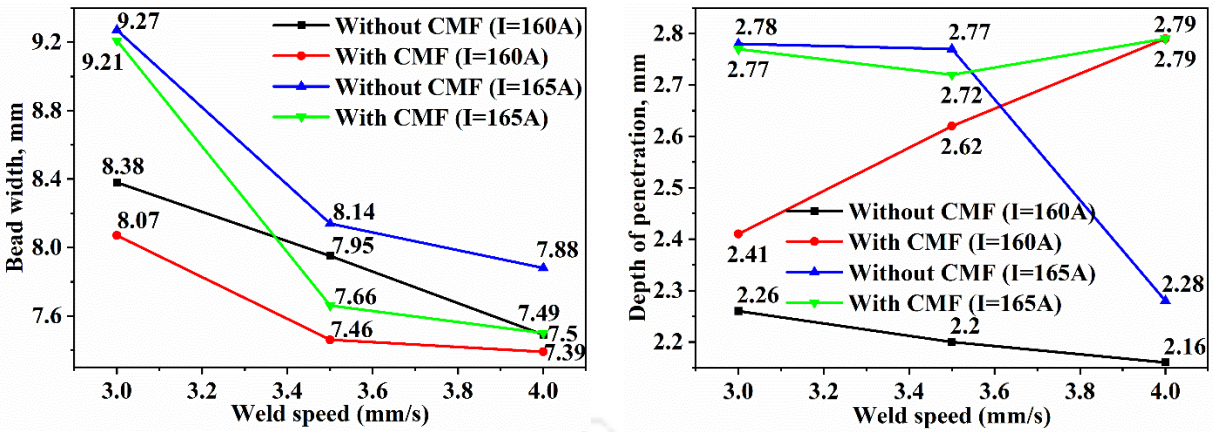

(a) (b)

Fig. 5.2 Effect of cusp magnetic field on bead width and depth of penetration: (a) Welding speed Vs bead width and (b) Welding speed Vs depth of penetration

.

While applying the cusp type magnetic field, the arc is stretched towards the welding direction in an ellipical cross section leading to smaller heating area along the normal to welding direction resulting in a narrower weld bead. Moreover, due to compression of arc, the arc force and energy density within the arc increases which further increases the plasma density leading to higher depth of penetrations [109,110].

5.3.2 Thermal histories and microstructure

Figure 5.3, shows the temperature profiles of the welds which were measured at a distance of 7.5 mm away from the centre line. The measured transient temperature distribution is compared for both with and without the application of CMF. The variation of the temperatures were majorly dependent on the amount of heat input. As the heat input increases, the transverse temperatures were increased in both the cases as shown in Fig. 5.3. Increasing the heat input from 0.32 kJ-mm^{-1} to 0.43 kJ-mm^{-1} resulted in increase of peak temperatures from 493.4°C to 705.8°C in case of without CMF, and 290.6°C to 431.2°C in case of CMF influenced welds. The application of cusp type magnetic field during welding produces two simultaneous effects. Firstly, anti-gravity gradient is produced by the arc within the cathode and anode thereby reversing the arc flow leading to a low temperature zone formation at center of arc on anode [29]. Secondly, it produces an electromagnetic stirring effect in the weld pool thereby increasing the convection within the weld pool resulting in higher thermal conductivity of molten metal. Due to higher convection rates, heat transfer in weld pool is increased resulting in decrement of peak temperatures as shown in Fig. 5.3. Also, due to arc contraction, the weld bead formed is narrower compared to weld bead formed without CMF. The reduced

temperatures help nuclei in weld pool survive and results in formation of equiaxed grains in weld fusion zone [5].

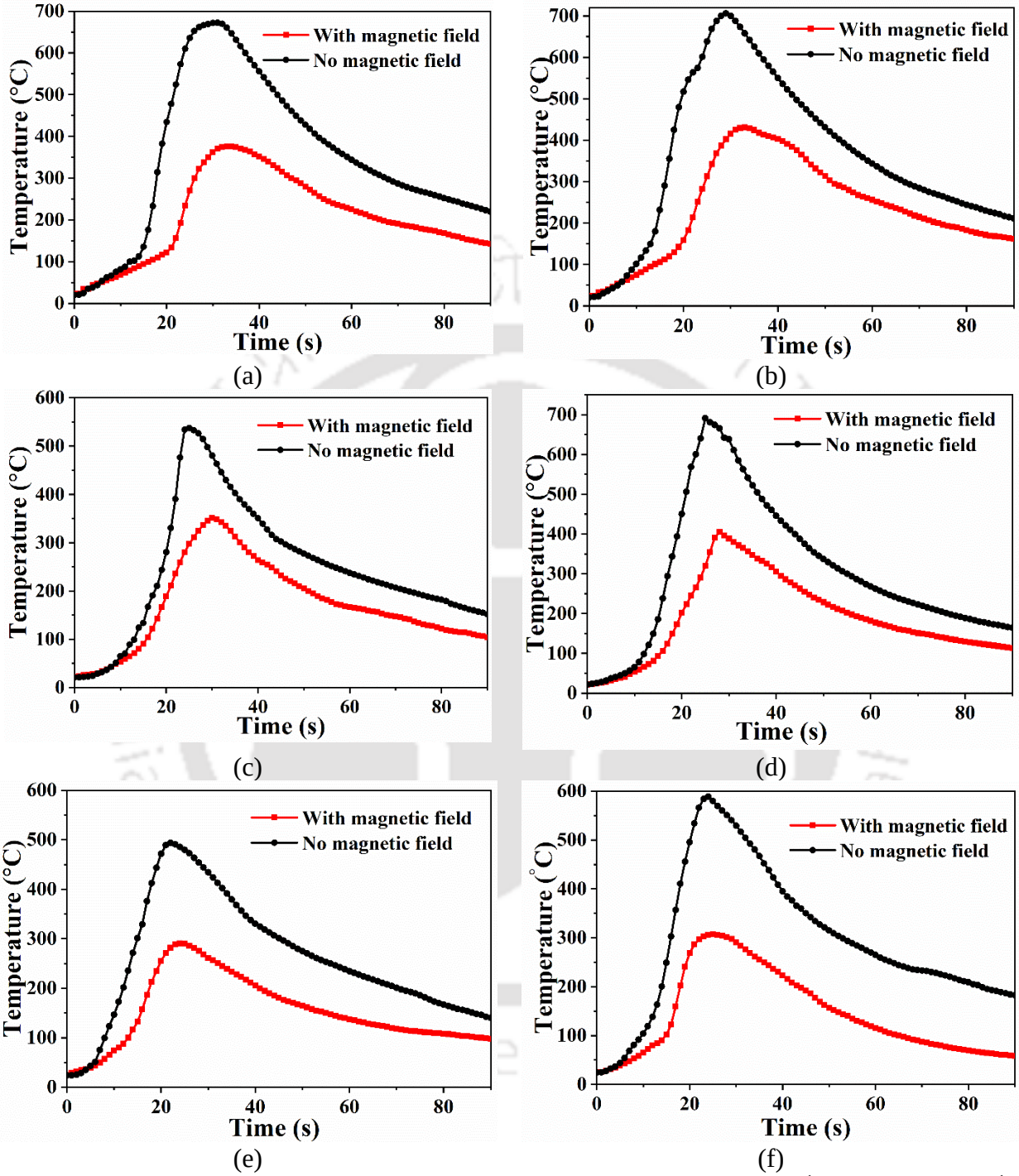

Fig. 5.3 Comparison of temperatures at various heat inputs (a) 0.43 kJ-mm^{-1}, (b) 0.45 kJ-mm^{-1}, (c) 0.37 kJ-mm^{-1}, (d) 0.39 kJ-mm^{-1}, (e) 0.32 kJ-mm^{-1}, (f) 0.34 kJ-mm^{-1}

The macroscopic view of welded cross-section, including the fusion zone, heat affected zone (HAZ) of both conventional and CMF assisted GTAW are shown in Fig. 5.4 (a, b). Figure 5.4c, represents the microstructure of base metal primarily consists of ferrite and pearlite (

$\alpha - Fe + Fe_3C$). Figure 5.4d, represents the fusion zone followed by heat affected zone, shown in Figure 5.4 (e, f), in conventional GTAW and CMF assisted GTAW, respectively. Enlarged view of grain structure in HAZ for the Fig. 5.4 (e, f) are represented in Fig. 5.4 (g, h) majorly consisting of ferrite (α). The major phases observed in fusion zone of both cases were ferrite, acicular ferrite (AF) and Widmanstatten ferrite (WF). By the application of external magnetic field, homogeneity in microstructure was observed in the fusion zone by forming equiaxed grains and also large quantities of AF and WF were observed compared to conventional GTAW. The grain size distribution in HAZ of the welds for both with and without magnetic field are shown in Table 5.2. The average grain size of the base metal is 12.46 µm. An average of 12% reduction in grain size is observed in CMF assisted GTAW. By the application of CMF, the arc is compressed as discussed earlier. As the compression of arc is high, larger the thermal gradients and higher the under cooling degree of weld during crystallization, resulting in refinement of grains [111] as shown in Table 5.2. Large volumes of WF are associated with refined microstructures resulting in higher toughness [111,112]. Due to this microstructure, the strength of the weld has been increased as shown in Table 5.3. From Fig. 5.5, it is clear that by increasing the welding speed the heat input is reduced resulting in the reduction of grain size in both the cases. At higher heat inputs, cooling rates are slower resulting in accelerating the nucleation and recrystallization which in turn causes the grains in HAZ to become coarser [5].

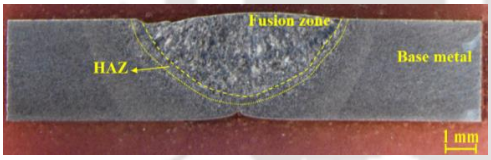

(a)

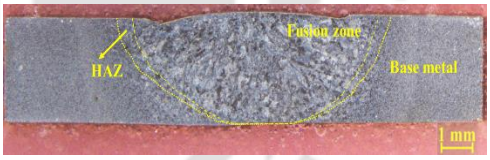

(b)

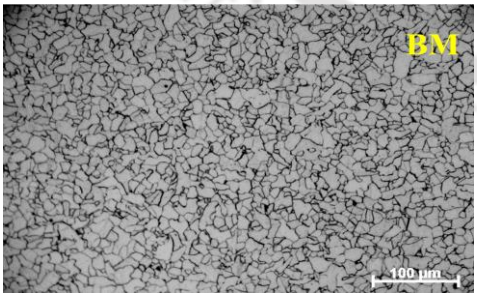

(c)

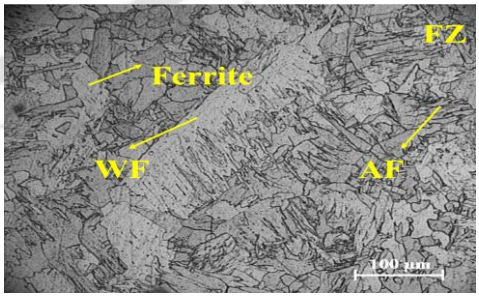

(d)

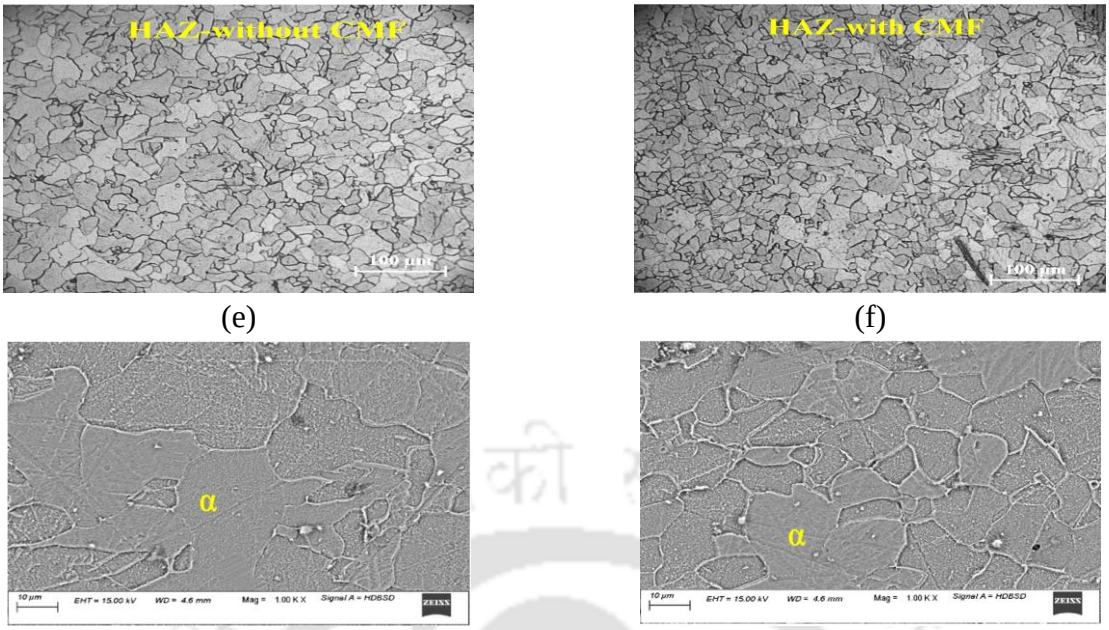

Fig. 5.4 Optical images of macroscopic and microstructure of weldments: (a) macroscopic view of weldment, (b) macroscopic view of CMF assisted weld sample, (c) Microstructure of base metal, (d) Microstructure of fusion zone, (e) HAZ -Without CMF, (f) HAZ - with CMF and FESEM images: (g) HAZ -Without CMF, (h) HAZ - with CMF

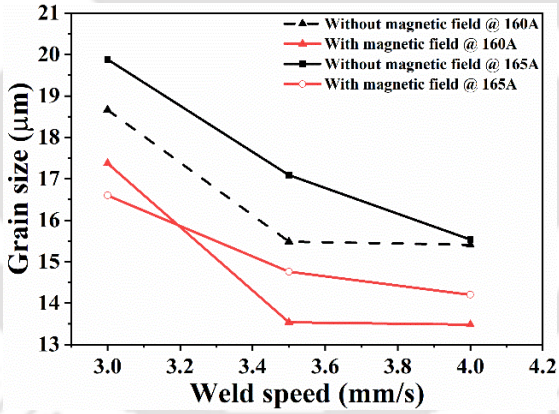

Fig. 5.5 Comparison of weld speed Vs grain size in HAZ

5.3.3 XRD analysis

XRD analysis of with and without magnetic field-assisted welded samples were conducted to analyze the phases present in the weld, as shown in Fig. 5.6. From XRD peaks, phases were identified in both the samples at different welding parameters settings. As per PDF-006-0696 cards, the peaks at 44.59 degrees refers to (110) miller indices, and correspondingly 64.80 refers to (200), 82.22 refers to (211), 99.06 refers to (220) and 116.25 refers to (310) miller

indices, representing body center cubic (BCC) microstructure. The phases present in the BCC microstructure indicates α-ferrite phases and Fe_3C phases [13].

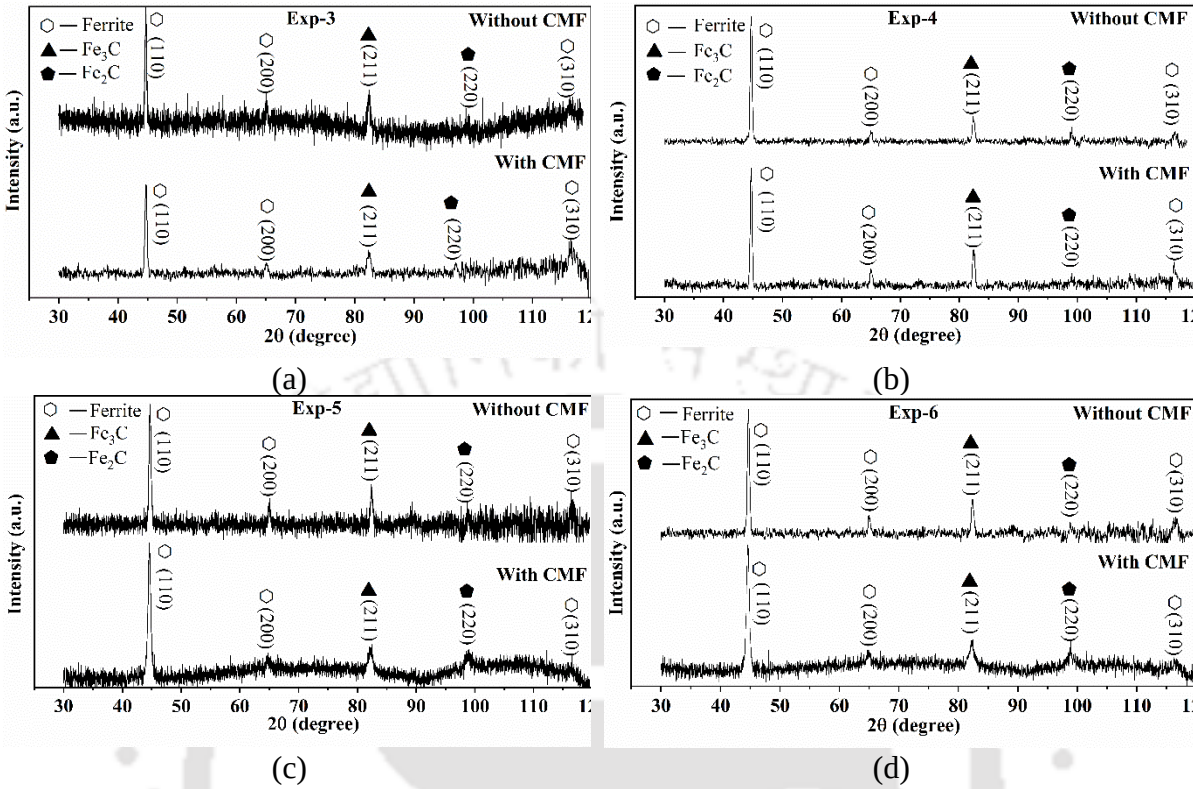

Fig. 5.6 Comparison of diffractograms between two processes at various heat input: (a) 0.37 kJ-mm^{-1}, (b) 0.39 kJ-mm^{-1}, (c) 0.32 kJ-mm^{-1} and (d) 0.34 kJ-mm^{-1}

In case of magnetically influenced welded samples, for all welding speeds, the peaks represent the broader full widths at half-maximum (FWHM) values. The comparison between both samples in terms of FWHM is shown in Table 5.2. Poorer crystallinity can be signified in terms of increased values of FWHM. Also, grain refinement is more and higher dislocation densities can be found at higher values of FWHM [113]. However, no significant change in the phase formation for both the weldments is observed. But the measured relative intensity of Fe_3C and Fe_2C are higher in case of conventional GTAW representing the higher volume fraction of Fe_3C and Fe_2C. In presence of external magnetic field, the diffusion of carbon in ferrite is inhibited [114]. It states that, under the influence of cusp type magnetic field in GTAW, significant changes in grain growth can be observed but not the phase composition. While reducing the heat input from 0.43 kJ-mm^{-1} to 0.32 kJ-mm^{-1}, the FWHM value is increased. As a result, it leads to an increase in the mechanical properties of the weld metal.

Table 5.2 Grain size distribution and FWHM values in both cases

Test case	Current (A)	Weld speed (mm/s)	CMF	Grain size (μm)		Full width at half-maximum (FWHM)
				HAZ 1	% Decrease	
Exp-1	160	3	No	18.66	6.90	0.487
			Yes	17.37		0.597
Exp-2	165	3	No	19.87	16.5	0.415
			Yes	16.59		0.485
Exp-3	160	3.5	No	15.48	12.6	0.657
			Yes	13.53		0.801
Exp-4	165	3.5	No	17.08	13.6	0.392
			Yes	14.75		0.466
Exp-5	160	4	No	15.40	12.5	0.696
			Yes	13.48		0.963
Exp-6	165	4	No	15.53	8.6	0.633
			Yes	14.22		0.847

5.3.4 Hardness

Figure 5.7 (a-f) shows the micro-hardness profile of welds for both with and without magnetic field at a gap of 1 mm transverse to the welding direction from the center of weld to base metal in both the directions. Based on the microstructural changes in the weld, the fusion zone, HAZ, and base metal were identified, as shown in the hardness graph. The hardness in the fusion zone is higher compared to the HAZ. The existence of partly un-melted grains at the fusion boundary region results in higher hardness. This is due to the current precipitating process of weld metal during solidification partially adopts them as nuclei. The coarse-grained microstructure can be observed in HAZ adjacent to the fusion area is due to the relatively slow cooling rate. Whereas the region adjacent to base metal is subjected to higher cooling rates due to steeper thermal gradients and has a fine-grained microstructure.

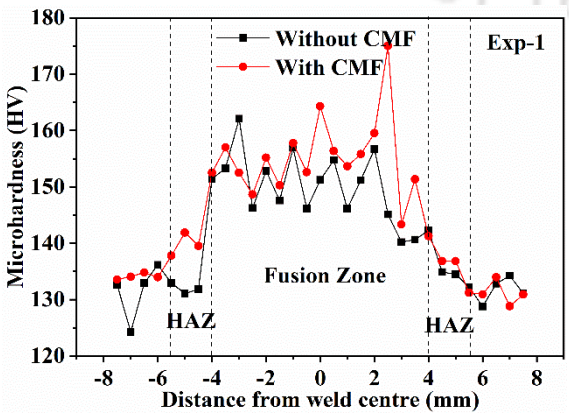

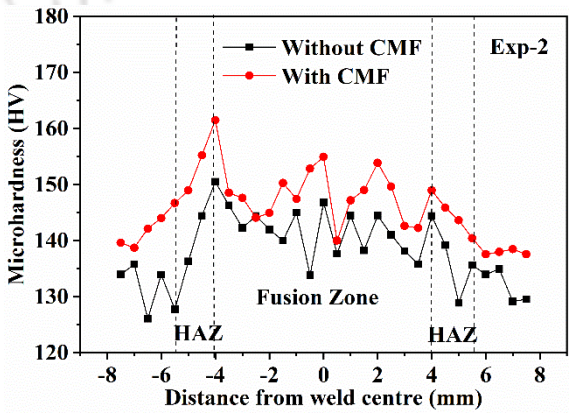

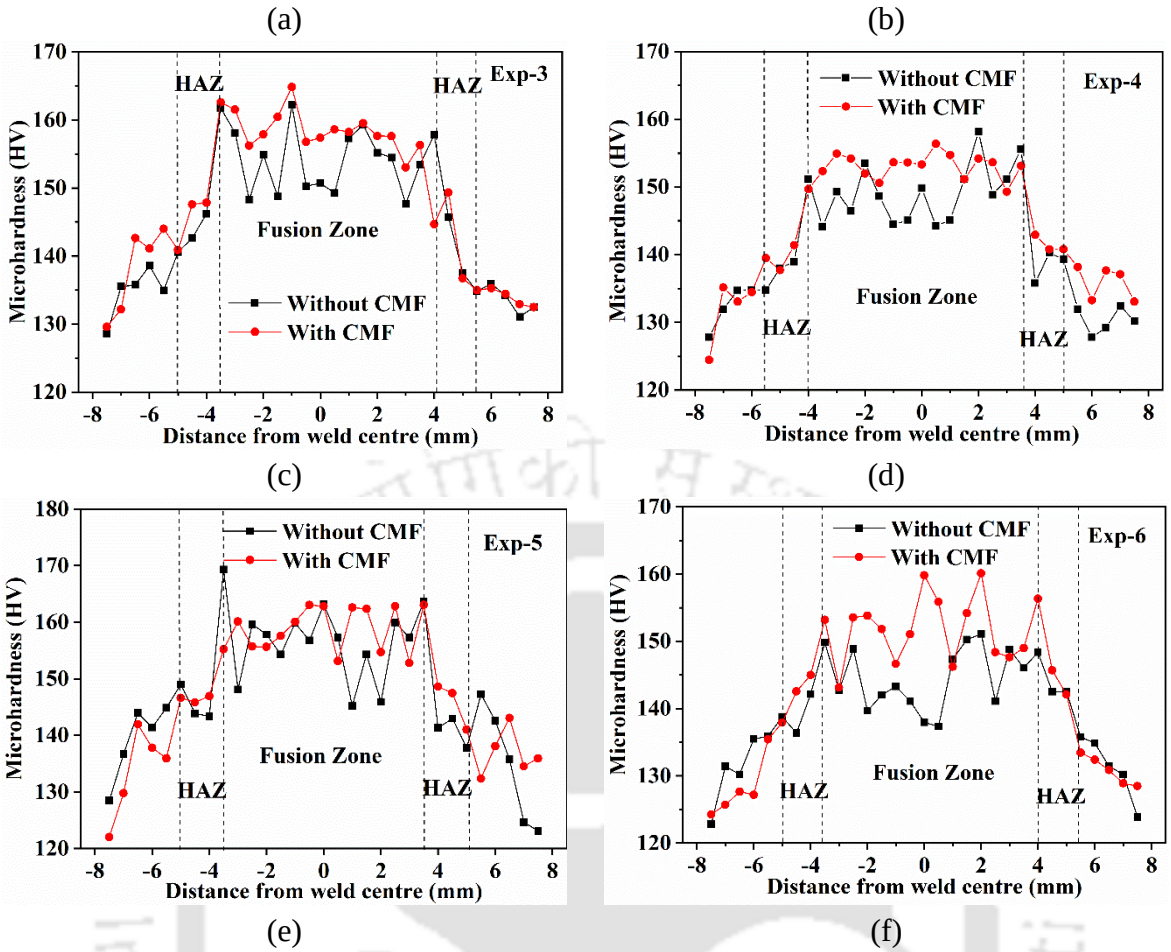

Fig. 5.7 Comparison of hardness between two processes: (a) 0.43 kJ-mm^{-1}, (b) 0.45 kJ-mm^{-1}, (c) 0.37 kJ-mm^{-1}, (d) 0.39 kJ-mm^{-1}, (e) 0.32 kJ-mm^{-1}, (f) 0.34 kJ-mm^{-1}

Figure 5.7, shows the average hardness of welds made with the magnetic field is higher than the welds without the magnetic field, Guan et al [92] also observed similar results. The magnetically enhanced arc was modified and turned into an oval shape, which in turn reduced the heat-induced area. As the arc is converged and elongated in the welding direction, the arc itself acts as a pre-heat source and the trailing edge acts as a post-heat source. Preheating the base metal result in higher hardness. And post-heating of weld pool result in uniform hardness in the fusion zone as compared to conventional GTAW. Also, due to grain refining, there is an increase in grain boundaries that leads to restriction of dislocation moment, thereby increasing the mechanical properties of the weld [115].

5.3.5 Tensile Test

An uni-axial tensile test provides conclusive strength parameters such as ultimate tensile strength (UTS), yield strength and % elongation. Tensile properties for each heat input condition were obtained and presented in Table 5.3. The presence of yield point phenomena

was observed in the base material. However, this phenomenon was absent in both conventional and CMF assisted welded samples.

Table 5.3 Tensile test results of welded joints for all experiments

Test case	Current (A)	Weld speed (mm/s)	Heat input (kJ-mm^{-1})	CMF	Yield strength (MPa)	UTS (MPa)	% Increase in UTS	% Elongation
Exp-1	160	3	0.43	No	276 ± 0	372 ± 6	2	27
				Yes	306 ± 1	380 ± 4		30
Exp-2	165	3	0.45	No	287 ± 8	367 ± 4	8	27
				Yes	306 ± 1	394 ± 2		27
Exp-3	160	3.5	0.37	No	284 ± 2	377 ± 1	1	24
				Yes	290 ± 8	383 ± 2		27
Exp-4	165	3.5	0.39	No	287 ± 9	387 ± 2	1	26
				Yes	298 ± 1	389 ± 6		29
Exp-5	160	4	0.32	No	272 ± 8	383 ± 4	0	29
				Yes	291 ± 10	383 ± 4		27
Exp-6	165	4	0.34	No	274 ± 4	378 ± 6	3	27
				Yes	295 ± 1	389 ± 6		39

The tensile properties of CMF assisted welds are higher than the conventional welded specimens. By varying both current and welding speed, the heat input is increased from 0.32 kJ-mm^{-1} to 0.45 kJ-mm^{-1}, the ultimate tensile strength and yield strength in magnetically influenced welded samples yield better results than non-magnetically influenced samples as shown in Fig. 5.8 (a, b). The ultimate tensile strength was increased by 3% and 8%, respectively, for an increase in heat input from 0.34 kJ-mm^{-1} to 0.45 kJ-mm^{-1} under CMF assistance. The fracture location of all the tensile specimens was at the boundary of HAZ and base metal, indicating that welding metal possesses greater strengths than the base metal. As the CMF assisted welds are high energy density welding processes, the amount of heat extracted from the heat source is also less. From the Fig. 5.3, it can be observed that the soaking periods are longer at peak temperatures than conventional GTAW process. It helps in refinement of grains which itself acts as a strengthening mechanism to improve the mechanical properties of the CMF assisted welds.

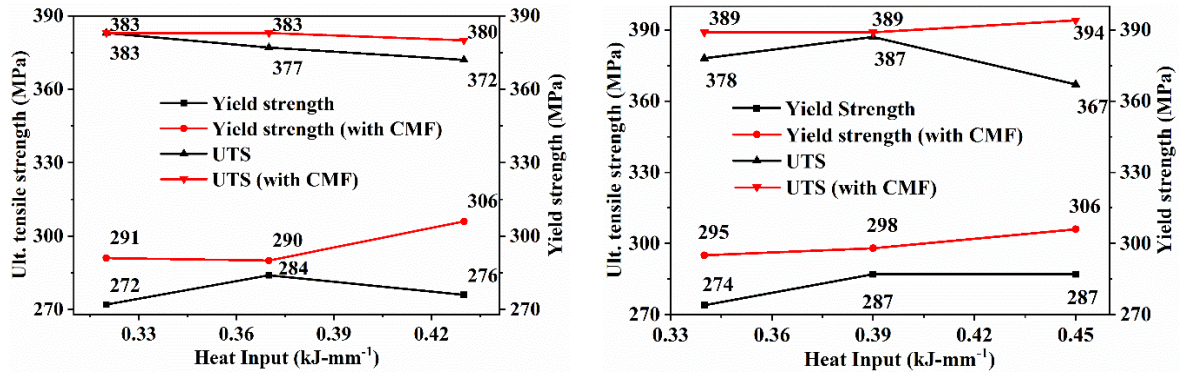

(a) (b)

Fig. 5.8 Tensile properties at various currents: (a) Heat input Vs UTS @ 160A and (b) Heat input Vs UTS @ 165A

Base metal elongation is 51%. The elongation in base metal is higher than the weld metal. However, CMF assisted welded samples exhibit 45% higher elongation than the weld without a magnetic field for experiment no.6 as shown in Table 5.3. Also, by comparing all the experiments, the elongation is increased by an average of 10%. It indicates that CMF assisted welds exhibit higher absorbed energies along with higher ductility and strength of the joints [13]. Furthermore, a weld's tensile strength is directly related to the presence of equiaxed grains in the microstructure. And the above phenomena resulted to the reduced sensitivity of finer grains to solidification cracking. The density of the grains can be increased by reducing the grain size. Higher the density of grains, the distribution of stress on the grains will be better leading to increase in the overall stress level of a weld.

5.3.6 Fractography

Failure analysis of fractured tensile samples was determined by using FESEM images. The FESEM fractography of base metal shows ductile mode of failure together with local intergranular cleavage type fracture. Figure 5.9a, shows the distribution of different sizes of dimples in the base metal indicating a ductile mode of failure. Figure 5.9 (b, c), represent the fracture morphology of both conventional and CMF assisted GTAW welded samples. In both the cases, micro-void coalescence along with finer dimples are observed. On calculating the number of voids per mm^2, there was a significant increase in the void number density of sample welded under the magnetic field when compared to the void number density of sample welded without a magnetic field.

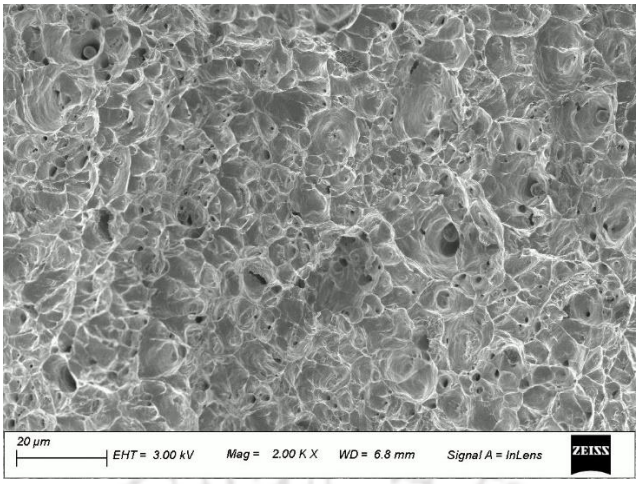

(a)

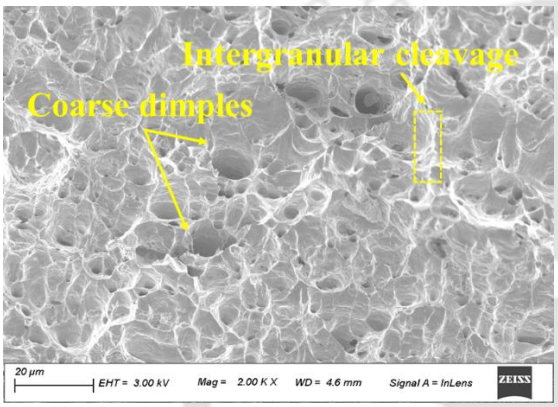

(b)

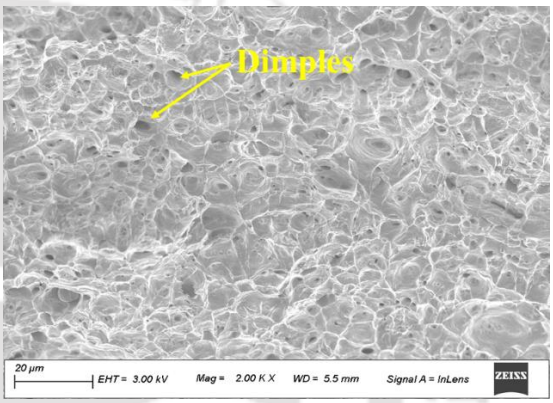

(c)

Fig. 5.9 Fracture surface morphology: (a) base metal, (b) sample welded without magnetic field and (c) CMF influenced weld sample

An increase in the void number density results in the improvement of strength of the joint [92]. Samples welded under the influence of CMF consist of deeper dimples than the samples welded without CMF. Size of the dimples reflect the amount of energy absorbed per unit area. Grain boundary volumes improved with decreased grain size. A higher density of small and shallow dimples was observed resulting in an increase of tensile strength and ductility. An increase in the heat input results in the formation of coarser and elongated dimples in both the cases.

5.4 Summary

With the application of CMF using premanent magnets to a GTAW process results in the change of arc shape and energy density within the arc. The study analyzed the impact of process parameters on the morphology and weld geometry, and noted an enhancement in the aspect ratio of the weld bead. It was found that increasing the heat input resulted in greater bead widths and depth of penetration, irrespective of the case considered. And, there is no considerable

phase changes in the weld, although the volume fractions of Fe3C and Fe2C are reduced in the CMF-assisted welds. Under CMF-assisted GTAW, two different heat inputs led to a 3% and 8% increase in UTS. Additionally, magnetically influenced weld samples exhibited a decrease in dimple size and an increase in dimple density, which resulted in improved mechanical properties. In summary, the application of a magnetic field in welding leads to a significant enhancement in both the metallurgical and mechanical properties of the weldment.

Chapter 6 Experimental Investigation of Cusp Magnetic Field Assisted GTAW of SS 304

6.1 Introduction

For a weldment, weld bead parameters like bead width, depth of penetration, thickness of HAZ, fusion zone geometry, and microstructures developed during welding all contribute to the overall quality of the welding and its performance under service conditions. In this study, experiments were carried out on AISI 304 SS metal using cusp-magnetic field (CMF) assisted gas-tungsten arc welding (GTAW) to improve the weld properties. The CMF was generated using four custom made samarium cobalt (Sm2Co17) permanent magnets. Influence of CMF on the weld morphology, metallurgical and corrosion properties were evaluated using various techniques. Experiments were conducted to measure the weld bead width, depth of penetration and mechanical properties such as micro-hardness and ultimate tensile strength (UTS). Also studied the elemental distribution of δ-Fe and γ-Fe using Schaeffler diagram. Microstructural analysis was performed using optical microscope (OM), energy-dispersive X-ray (EDX), Field-emission scanning electron microscope (FESEM), and X-ray diffraction (XRD) techniques. Experimental findings showed improvement in mechanical, metallurgical and corrosion properties compared to conventional GTAW.

6.2 Experimentation

For welding of 304 SS plates of 3.1 mm thickness, welding speed and current were taken as major process parameters along with cusp magnetic field. 12 experiments were conducted by varying the process parameters without using external magnetic field. And with the influence of CMF, 12 more experiments were carried out with the same process parameters which were used for conventional GTAW. Welded samples prepared for characterization and analysis were developed using the same process as discussed in chapter 4. The process parameters used in this study is presented in Table 6.1.

6.3 Results and discussion

6.3.1 Effect of CMF on weld bead macrostructure

The measured bead width (w), and depth of penetration (h) of the welds for different welding conditions are shown in Table 6.1. Figures 6.1 (a, b), (c, d) and (e, f) show the optical macrostructures of the specimens welded without and with the application of CMF for experiment nos. 1, 5 and 9, respectively. The samples welded with the application of CMF were having smaller bead widths and higher depth of penetrations as shown in Table 6.1. An average of 13% reduction in bead width and an increase of 37% in depth of penetration were observed. While applying cusp magnetic field, the arc was stretched towards the direction of welding in an elliptical cross section leading to smaller heating area. This leads to increase in density of heat to a minimal area resulting in a narrower weld beads and higher depth of penetration. The maximum depth of penetration and minimum bead width were observed at a higher current of 170A and weld speed of 4 mm/s (heat input of 0.38 kJ-mm^{-1}) in magnetic field assisted weld. In conventional GTAW, at higher welding speeds, the depth of penetration was upto half of the plate thickness. But for the same amount of heat input in CMF assisted GTAW, the depth of penetration was almost equal to plate thickness and achieving minimum bead widths as shown in Fig. 6.1.

Table 6.1 Process parameters and geometry of fusion area

Test case	Current (A)	Weld speed (mm/s)	Heat input (kJ-mm^{-1})	No CMF		With CMF		% decrease in w	% increase in h
				w (mm)	h (mm)	w (mm)	h (mm)		
Exp-1	140	3	0.42	8.63	3.10	7.65	3.10	11.4	0
Exp-2	150	3	0.45	9.09	3.10	7.44	3.10	14.9	0
Exp-3	160	3	0.48	9.32	3.10	7.89	3.10	15.3	0
Exp-4	170	3	0.51	9.45	3.10	8.38	3.10	11.3	0
Exp-5	140	3.5	0.36	7.85	1.90	7.25	2.47	7.6	30.0
Exp-6	150	3.5	0.39	8.15	1.85	7.72	3.10	5.3	67.6
Exp-7	160	3.5	0.41	9.22	1.90	8.75	3.10	5.1	63.2
Exp-8	170	3.5	0.44	9.44	3.10	7.95	3.10	15.8	0
Exp-9	140	4	0.32	7.83	1.85	6.54	2.89	16.5	56.2
Exp-10	150	4	0.34	8.08	1.46	7.27	2.93	10.0	100.7
Exp-11	160	4	0.36	9.09	1.54	7.80	3.10	14.2	101.3
Exp-12	170	4	0.38	9.65	2.54	6.94	3.10	28.1	22.0

The mechanism of enhanced depth of penetration is primarily evident in the compression of the arc by the CMF, thereby, concentrating the maximum amount of arc energy in the molten pool. The additional CMF causes the ampere force to concentrate at the middle of weld bead and pulls the hotter liquid of molten metal from the front, protruding the solid-liquid surface in depth direction [116].

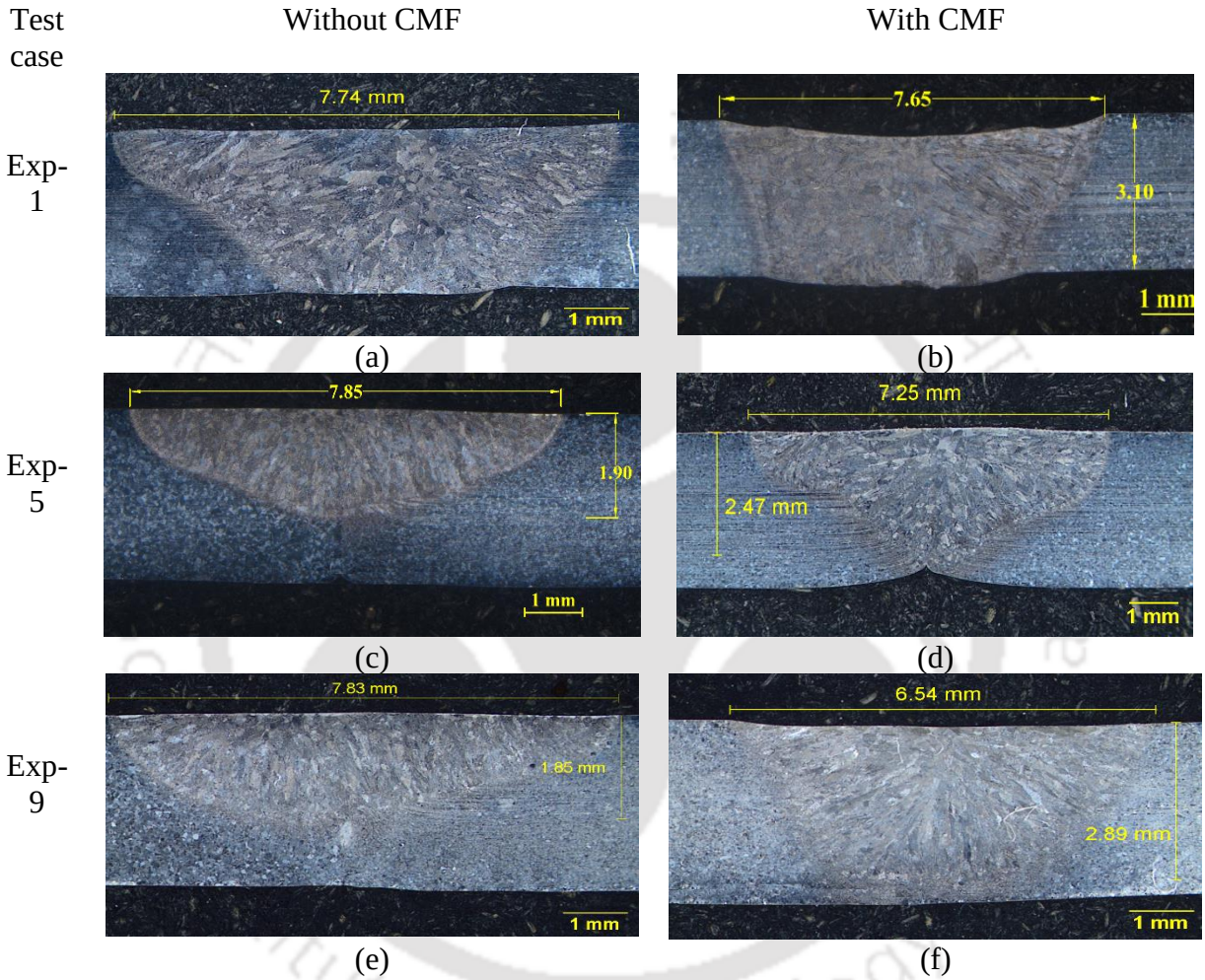

Fig. 6.1 Comparison of transverse weld profiles at different welding speeds: (a-b) 3 mm/s, (c-d) 3.5 mm/s, and (e-f) 4 mm /s at 140A

The geometry of the fusion zone is strongly influenced by the welding speed and current. The width of the weld bead was increased with the increasing welding current, as shown in Fig. 6.2, for both with and without CMF. Higher values of arc current lead to more heat input per unit length at a fixed welding speed. Hence, larger volumes of base metal are being melted resulting in increase of bead width. At slower welding speeds, bead width and depth of penetration were increased due to substantial enhancement of weld line energy. By increasing the welding speed,

bead width and depth of penetration were reduced in both the cases. This was due to reduce of heat input per unit length.

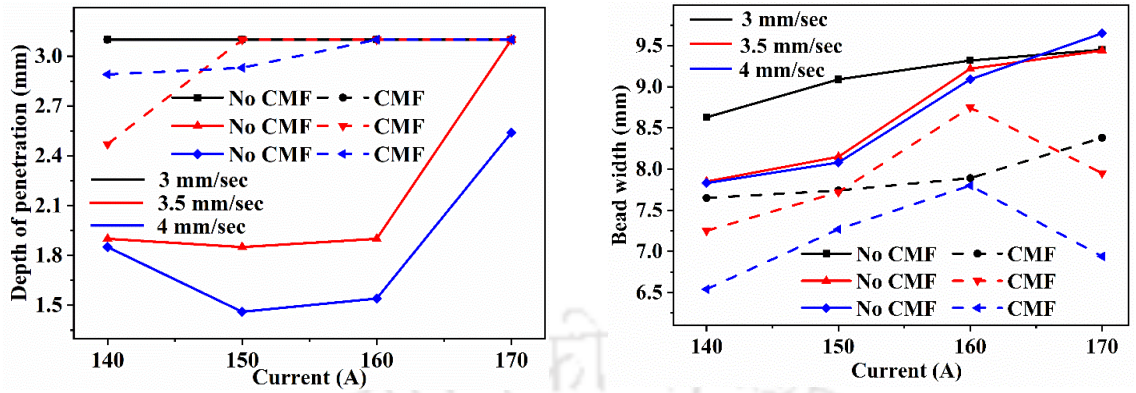

Fig. 6.2 Effect of welding current on (a) depth of penetration, and (b) bead width

6.3.2 Thermal analysis

Figure 6.3 (a-f), illustrates the comparison of temperature profiles of the welds at a distance of 6.5 mm from the weld center line for a welding speed of 3, 3.5 and 4 mm/s at a current of 140 A and 170 A. As the heat input increases by varying the welding speed and current, resulted in the increment of temperature for both the cases. Meanwhile, the peak temperature decreased with the application of CMF for the same amount of heat input as shown in Fig. 6.3. The maximum temperature was obtained in Exp-4 followed by Exp-8 and Exp-12. In all these cases, the highest current of 170 A was used at a welding speed of 3, 3.5 and 4 mm/s. The minimum peak temperature was obtained at lowest heat input of 0.32 kJ-mm^{-1}.

In absence of external magnetic fields, the welding arc charge particles have a particular spiral radius along the symmetry of its own axis due to the interactions from the temperature field and self-inductance magnetic field. By application of magnetic field, an additional Lorentz force is formed on the charge particles causing them to rebalance and attain a state of re-equilibrium [29]. The Lorentz force causes changes in particle movement, resulting in variations in current density and temperature field in CMF assisted GTAW. The arc energy density within the arc space is increased due to the constriction of arc by additionally induced Lorentz force. Also, the CMF induces a stirring effect in the weld pool resulting in enhancement of the convection rates. The peak temperatures in CMF assisted welds were reduced due to increment in heat transfer rate caused by convection [107]. A narrower weld bead was formed due to constriction of arc and the heat flux was also distributed over a narrow region as compared to conventional GTAW. This was also a reason to attain lower peak temperatures at the measuring point. Due to higher arc energy densities, the thermal energies

attained in CMF assisted weld pool is higher and the cooling rate is little slower resulting in favorable conditions for precipitation of austenite.

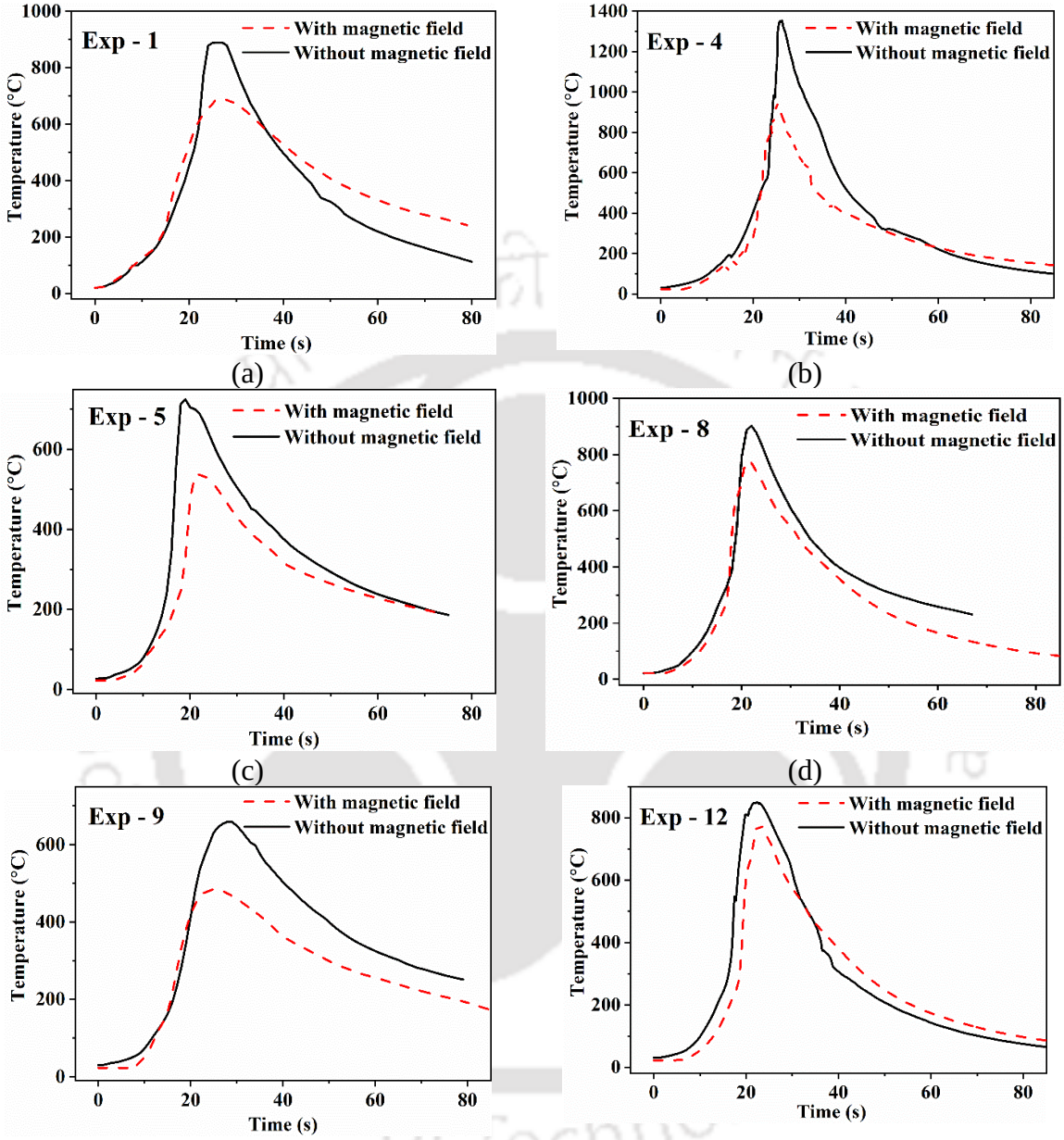

Fig. 6.3 Welds thermal cycles of (a) Exp-1, (b) Exp-4, (c) Exp-5, (d) Exp-8, (e) Exp-9, and (f) Exp-12

6.3.3 EDX analysis of welds

Figure 6.4, represents the SEM images of the weld beads consisting of ferrite and austenite phases. The type of microstructure developed depends on the weld pool solidification behavior. The weld metal solidification structure in ASS is dendritic with enormous quantities of elemental segregation. The primary elements, namely chromium (Cr), molybdenum (Mo), and

nickel (Ni), as well as their equivalent ratio (Cr_{eq}/Ni_{eq}), influence the types of phases that form in the weld metal during solidification. The Cr and Ni equivalents are calculated using Schaeffler diagram and can be expressed as:

$$Cr_{eq} = W_{Cr} + W_{Mo} + 1.5W_{Si} + 0.5W_{Nb} \quad (8)$$

$$Ni_{eq} = W_{Ni} + 0.5W_{Mn} + 30W_{C} \quad (9)$$

The ferrite quantity in the weld can be estimated using Schaeffler diagram [12]. The chemical composition (in wt.%) of welded samples were measured using EDX spectroscopy and are shown in Fig. 6.4 (c, d). Figure 6.5 (a, b), represents the quantity of ferrite in the fusion zone and HAZ for both conventional and CMF assisted welds. The average Cr_{eq}/Ni_{eq} ratio in the fusion zone and HAZ for all the experiments were above 1.5 as shown in Fig. 6.5 (c, d), representing a fully austenitic solidification mode.

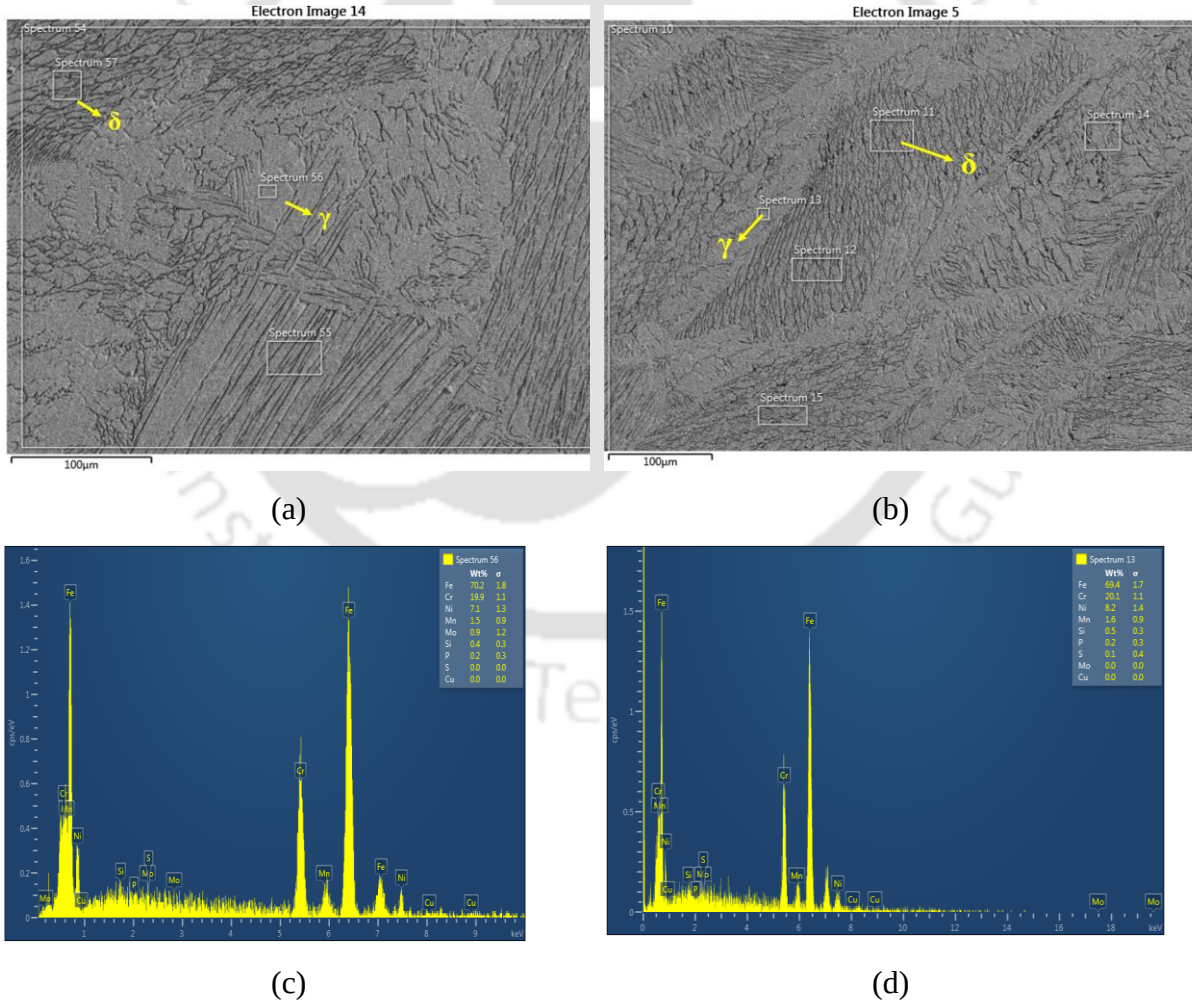

Fig. 6.4 Fusion zone microstructure of Exp-1 (a) without CMF, (b) with CMF. EDX results for austenite phase: (c) without CMF, and (d) With CMF

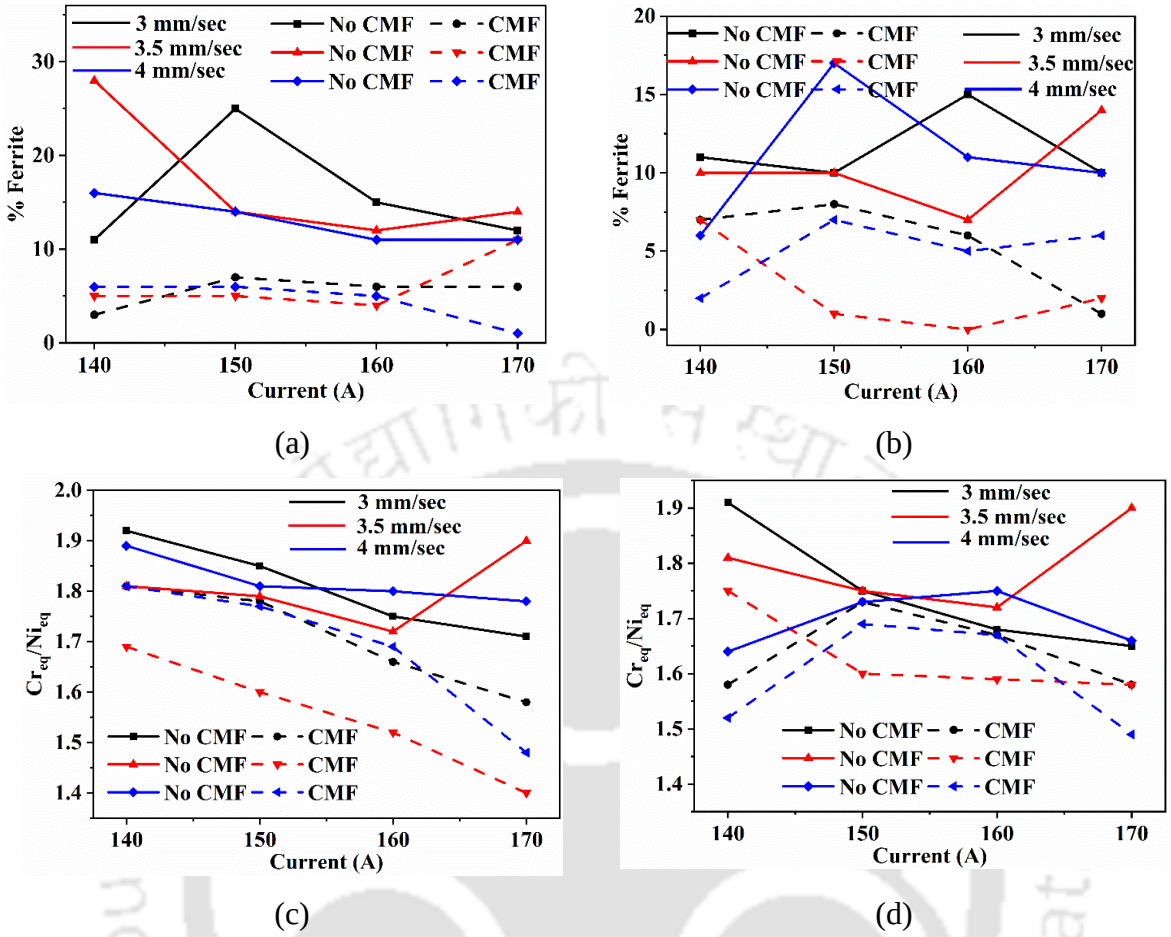

Fig. 6.5 Effect of welding current on ferrite quantity (a) in fusion zone, (b) HAZ, and (c) Cr_{eq}/Ni_{eq} ratio in fusion zone, and (d) Cr_{eq}/Ni_{eq} ratio in HAZ

The average ferrite quantity in the fusion zone of conventional and CMF assisted welds were 15.5 %, 5.5 % and in HAZ, the average quantity were 11 %, 4.3%, respectively. The ferrite quantity in CMF assisted welds in the fusion zone and HAZ were reduced by 65 % and 61 %, respectively, as compared to conventional GTAW. By increasing the current for a given speed, the heat input increases resulting in decrease of Cr_{eq}/Ni_{eq} ratio and ferrite quantity in both the welding cases. In case of CMF assisted welds, stirring effect induced by the magnetic fields introduces many aspects: diversifies the thermal gradient direction resulting in the formation of weak intensity δ-skeletal ferrite, promoting columnar to equiaxed transition, re-melting of the dendrite arms and limiting its growth. Also, the stirring effect induced in the weld leads to the detachment of grains and escalates the number of sites for nucleation of γ-austenite [107]. The results showed that, while applying CMF, the Cr_{eq}/Ni_{eq} ratio and ferrite quantity were decreased as a result of increased in nickel equivalent which leads to increase in austenite phases. The nickel acts as a promoter for the formation of austenite phase and chromium for

formation of ferrite phase. Furthermore, the transition from delta ferrite to austenite occurs by diffusion in a solid state [117]. In magnetically influenced welds, the cooling rate is slightly slower than conventional welds resulting in precipitation of austenite and growth within the ferrite grain boundaries attributed to enhance the austenite phase in the welds. As the austenite is a phase of paramagnetic and the domains are oriented randomly; thus, the magnetic fields interaction induces vibration of the atoms [118]. This interaction on vibration of atoms also promotes the transformation of the ferrite to homogenized austenite matrix. Homogeneity of elemental distribution was also observed in CMF assisted welds and was confirmed by the micro hardness profiles.

6.3.4 Microstructural analysis

In fusion welding of steels using GTAW, interaction of arc plasma with material leads to formation of weld pool. The molten metal in the weld pool experiences recirculation and flow of liquid metal which in turn effects the thermal cycles and the formation of weld pool geometry. And, non-uniform temperature gradient in the weld pool and its surroundings leads to formation of three zones in the weldment. They are namely, fusion zone, HAZ and unaffected base material. By the application of heat source to the base material, HAZ size is mostly influenced by the amount of heat applied to the surface of the workpiece. Figure. 6.6, represents the HAZ thickness for both conventional and CMF assisted welds. The HAZ is narrower in CMF welds for same amount of heat input. The average size of the HAZ in conventional and CMF assisted welds were 60 µm and 30 µm, respectively as shown in Fig. 6.6c. In both the welding cases, with increase in heat input the thickness of HAZ was increased. This clearly depicts the effect of welding current and speed on the HAZ thickness.

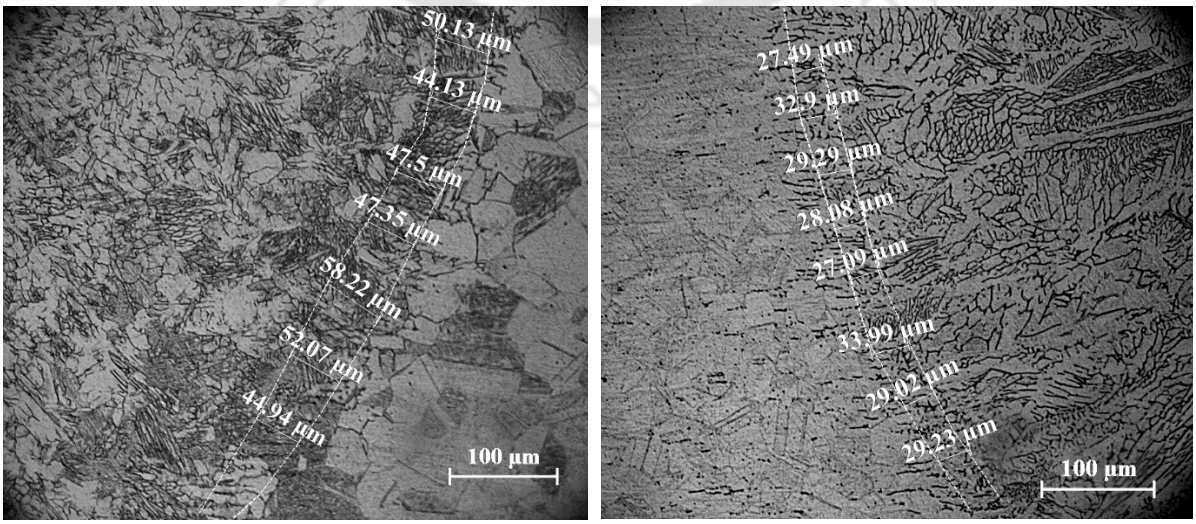

(a) (b)

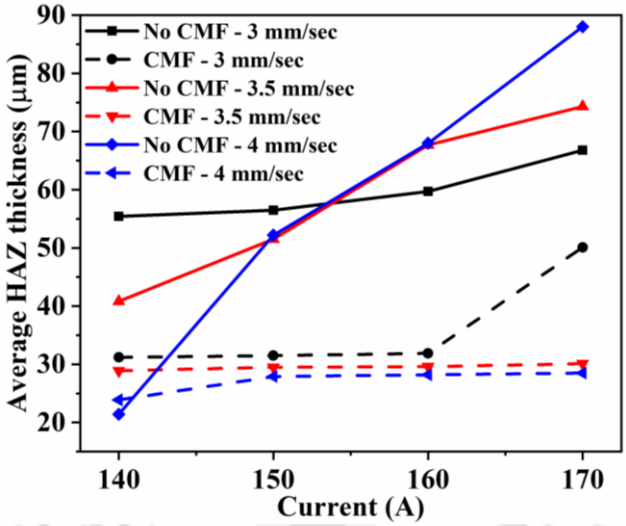

(c) HAZ thickness

Fig. 6.6 Width of HAZ for Exp-11: (a) Without CMF, (b) With CMF; and (c) HAZ thickness for all experiments

As shown in Fig. 6.7, in conventional arc welding, the heat diffusion takes place in the opposite direction of thermal gradient along the same plane and is perpendicular to solid-liquid interface. This results in increase of growth direction perpendicular to the fusion line. As the heat is diffusing along the fusion line, due to curvature of the weld zone the heat will accumulate at a closet point A (Fig 6.7a). Under these conditions, the longest period of high temperature will encourage the base metal to form wider heat affected zones [119]. With the application of CMF, the diffusion of heat is parallel through the fusion line without accumulating at point B (Fig 6.7b). Due to this condition, the base metal experiences very less time at higher temperatures resulting in a narrower heat affected zones.

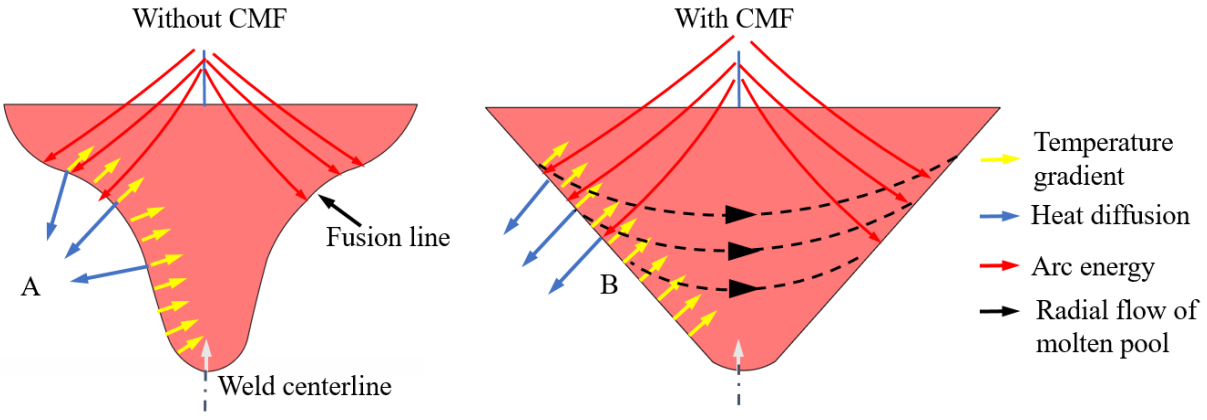

Fig. 6.7 Schematic illustration of temperature distribution in (a) weld bead without CMF, and (b) Weld bead with CMF

As discussed earlier, evolution of microstructure dependents on ampere force in CMF assisted welds. The additional ampere force leads to deflect the δ-dendrites from the vertically growing direction. The dendrites close to solid-liquid boundary develop at faster rates than lower ones and forms an asymmetrical structure. The additional magnetic field induces the radial flow, pushes the hot liquid to mushy zone, re-melt and disrupt the dendrite, as shown in Fig. 6.8. The fracture and necking of δ-dendrites, escalates the number of crystal nuclei of δ-dendrites and block the evolution of austenite. This primary dendrite leads to the formation of refined subsequent γ-grains. The external magnetic field acts as a driving forces for nucleation and recrystallization. The average grain size of base metal was 33 µm. The grain size of CMF influenced welds was 22 µm and conventional welds was 32 µm as illustrated in Fig. 6.9 (a-c).

Skeletal morphology and lathy morphology δ-ferrite were formed in CMF assisted and conventional GTAW joints, respectively, as depicted in Fig.6.9 (d and e). Due to moderate cooling rate, skeletal morphology was formed as a result of limited diffusion. During the diffusion process, the ferrite was enhanced adequately in ferrite stimulating elements, such as Cr, Mo and deprived in elements that are promoting austenite, such as nickel [120]. And lathy ferrite was formed in higher cooling rates due to restricted diffusion during the solidification.

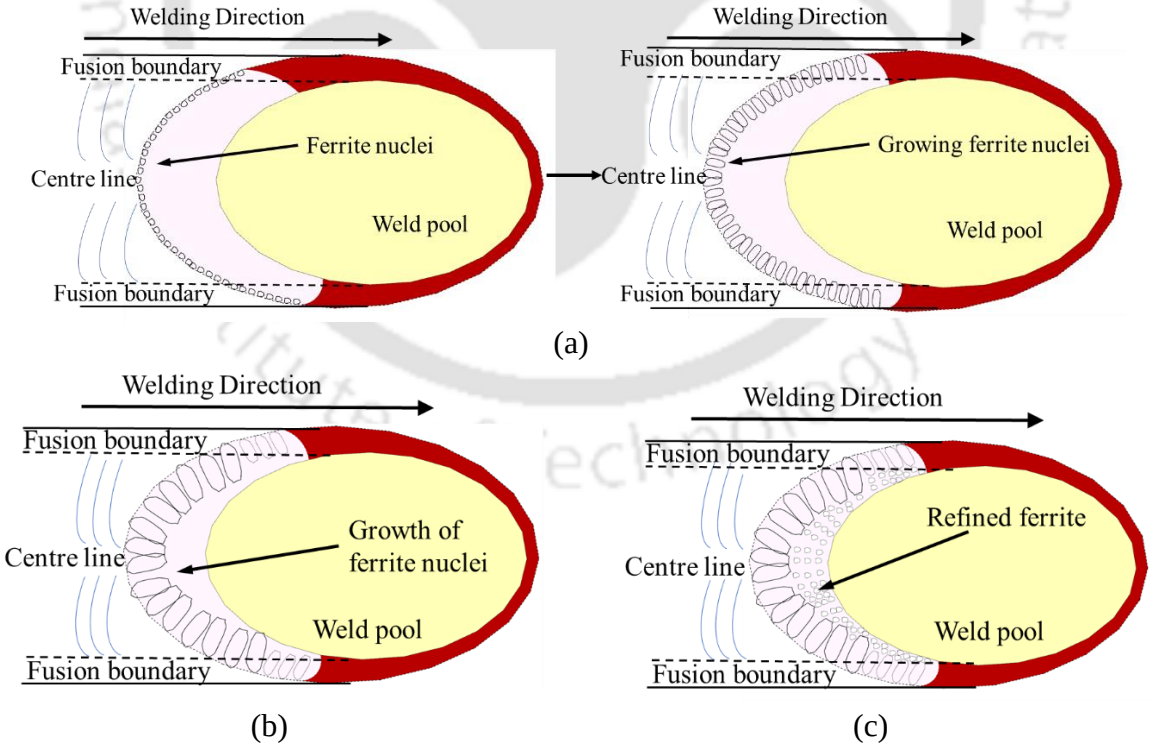

Fig. 6.8 Ferrite grain refinement mechanism (a) Ferrite nuclei growth, (b) Growth of ferrite nuclei in conventional GTAW, and (c) Refinement of ferrite grain in CMF assisted weld

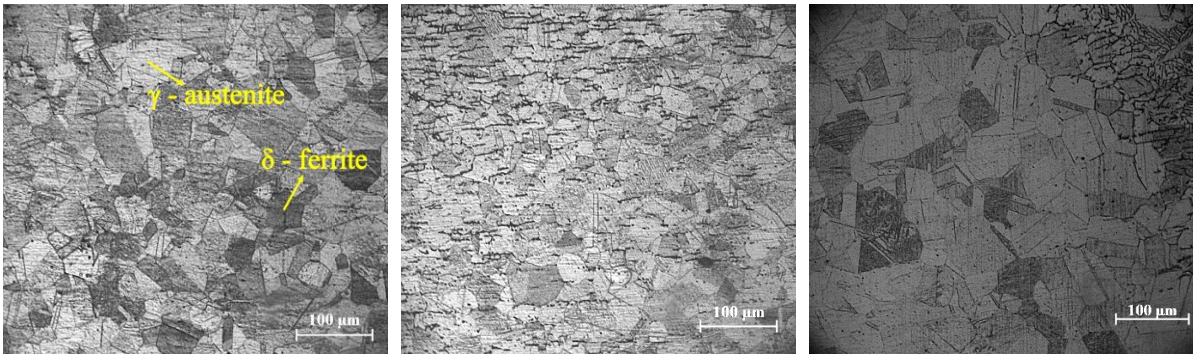

(a) (b) (c)

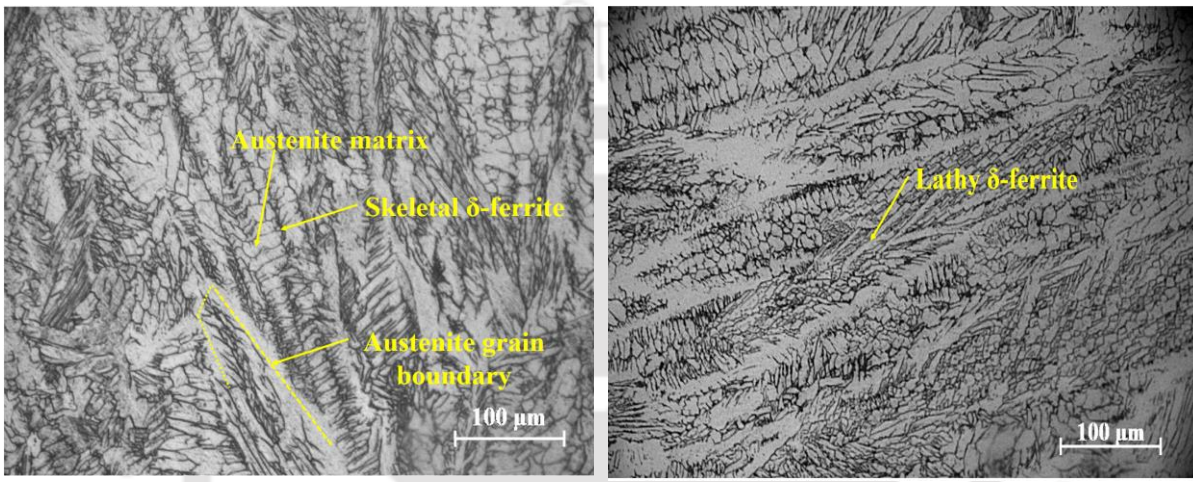

(d) (e)

Fig. 6.9 Grain size (a) base metal, (b) CMF assisted weld, (c) conventional GTAW, and fusion zone microstructure of (d) CMF assisted weld, and (e) Conventional GTAW

6.3.5 XRD analysis

XRD was carried out to identify and analyze the phases present in both the conventional and CMF assisted welds. Figure 6.10, depicts the XRD patterns of base metal and welded samples of Exp-3, Exp-7 and Exp-11. XRD patterns representing two major phases present in the weld metal: austenite (γ) and ferrite (δ) for all welding heat input conditions. The peaks in the base metal at 44.48° refers to (111) miller indices, and correspondingly 45.42° refers to (110), 51.66° refers to (200), 75.46° refers to (220), 82.88° refers to (310), 91.36° refers to (311) and 96.68° refers to (222) comprising of major quantities of austenite and minor quantities of ferrite. No precipitated chromium carbides were formed in the weldment in both the cases.

In the weld zone, carbide formation was absent in both the cases. From analysis it was observed that, in CMF assisted welds, the peaks represent higher values of broader full widths at half-maximum (FWHM). This leads to higher dislocation densities in the weld. The grain size and dislocation densities are inversely proportional to each other [121], representing the reduction

of grain size in magnetically influenced welds. Furthermore, a small quantity of δ-ferrite was present in both the cases, it is advantageous in reducing the hot cracks during weld solidification.

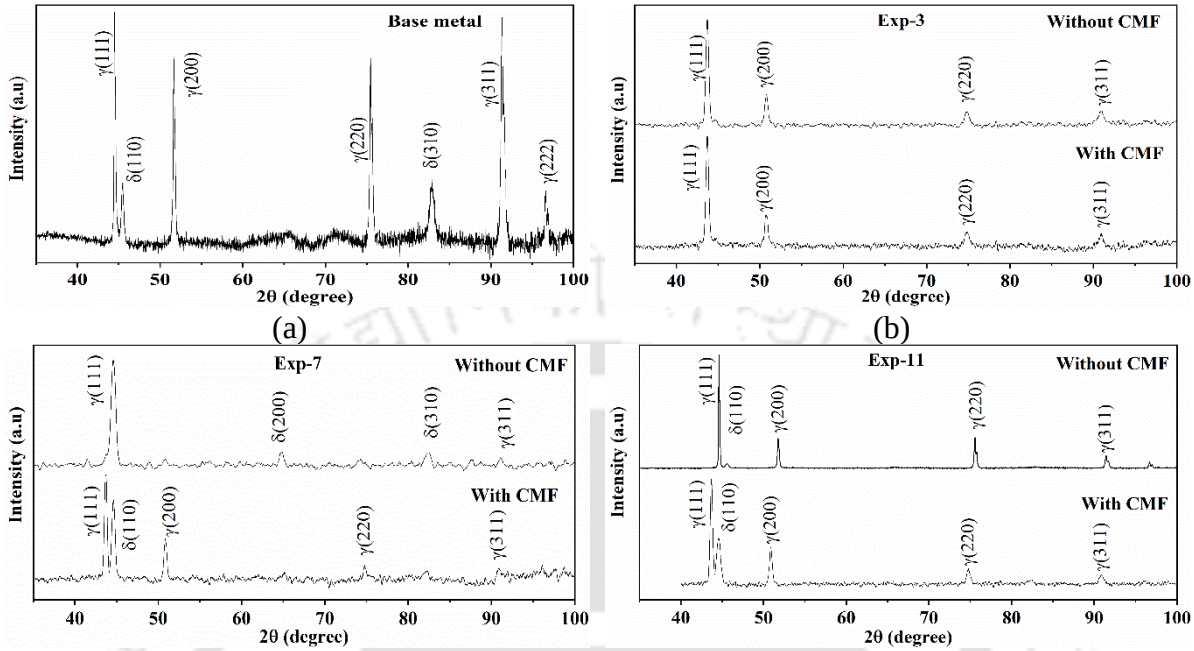

Fig. 6.10 XRD phase analysis (a) base metal, (b) Exp-3, (c) Exp-7 and (d) Exp-11

6.3.6 Hardness

After welding of base material, microstructure and phases may changes in the weldment causing to a change in hardness value of the material. The hardness values vary from unaffected base material to HAZ and fusion zone. Figure 6.11, represents the micro hardness profiles of all the experiments for both without and with the application of CMF. Hardness indentation was done at a depth of 1 mm transverse to the weld cross section. The fusion zone, HAZ, and base metal regions were determined based on microstructural changes in the weld, as illustrated in the hardness graph. The hardness of base metal was 179 HV, and the hardness of all the welds were almost greater than the base metal. Hardness was high in HAZ followed by fusion zone and unaffected base metal. Because, the coarse-grained microstructure can be observed in HAZ adjacent to the fusion area was due to the relatively slow cooling rate. Whereas the region adjacent to base metal is subjected to higher cooling rates due to steeper thermal gradients and has a fine-grained microstructure.

There was no major difference in the fusion zone hardness for both the cases. Meanwhile, on an average the hardness in conventional GTAW was slightly higher than magnetic field assisted welds. The amount of ferrite quantity in the fusion zone was slightly higher in case of without

magnetic field assisted welds resulted in increased hardness. But in CMF assisted welds, due to refinement of grains in HAZ, the hardness is slightly higher in HAZ as compared to conventional GTAW as per Hall-Petch formulae. A homogeneous distribution of hardness was observed in CMF welds due to stirring action and homogenized elemental distribution in the molten pool as discussed earlier.

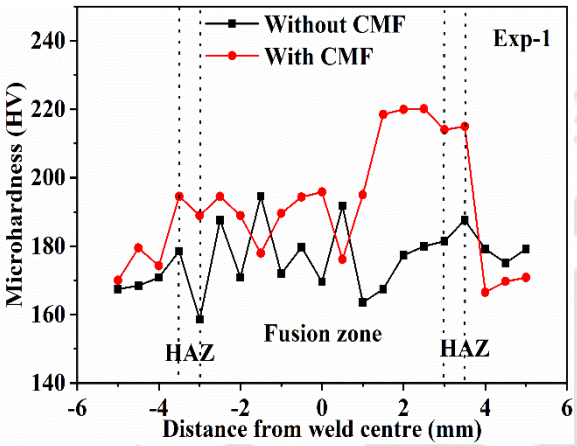

(a)

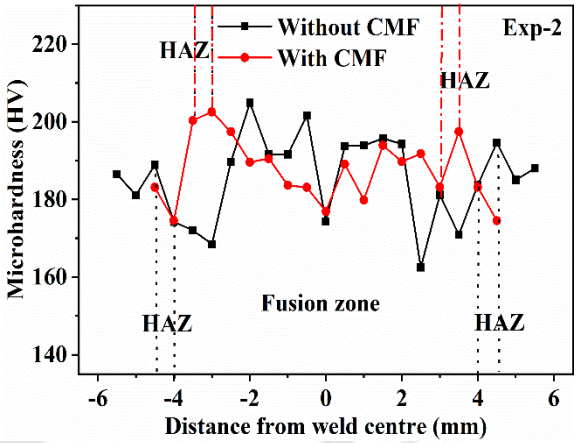

(b)

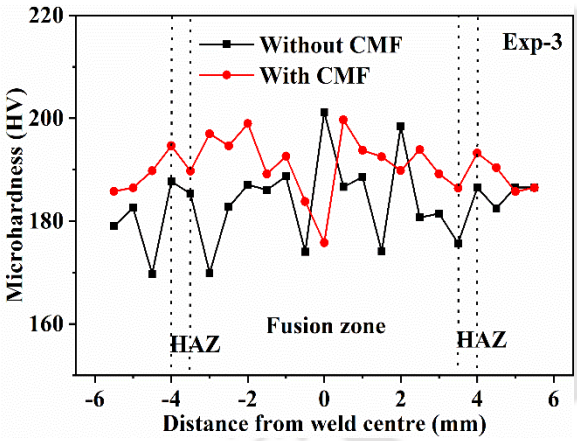

(c)

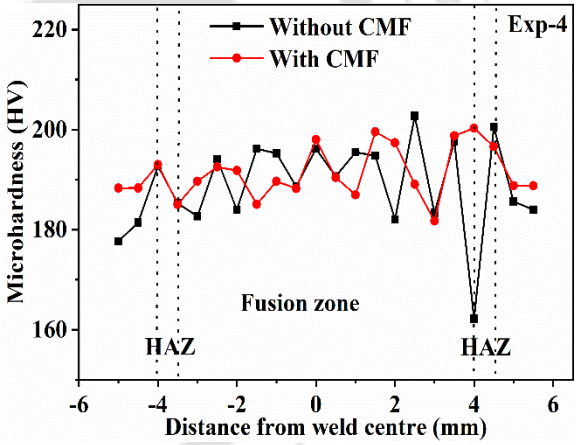

(d)

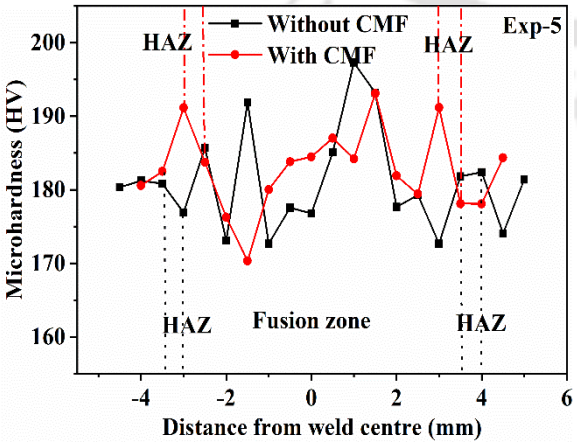

(e)

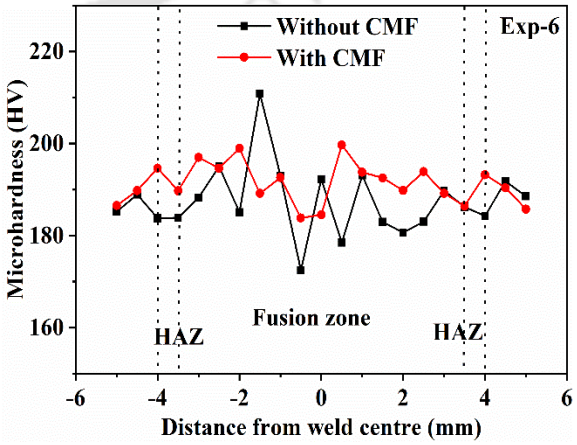

(f)

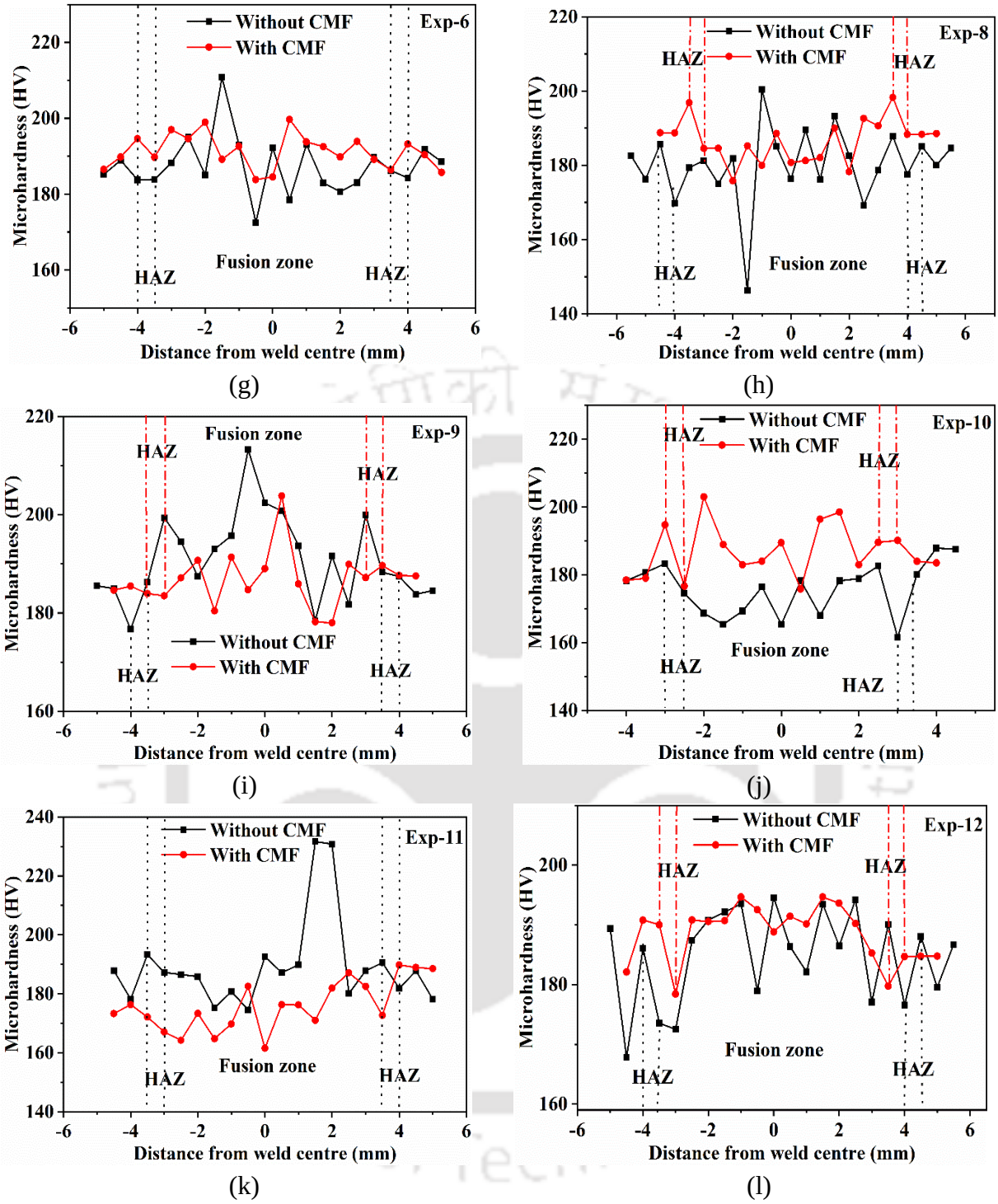

Fig. 6.11 Comparison of hardness between two welding cases of (a) Exp-1, (b) Exp-2, (c) Exp-3, (d) Exp-4, (e) Exp-5, (f) Exp-6, (g) Exp-7, (h) Exp-8, (i) Exp-9, (j) Exp-10, (k) Exp-11, and (l) Exp-12

6.3.7 Tensile properties

An uni-axial tensile test provides conclusive strength parameters namely % elongation, and ultimate tensile strength (UTS). The base metal UTS and elongation were 728 MPa and 28 %,

respectively, as illustrated in Fig 6.12a. Table 6.2, shows the tensile properties of all the experimental conditions.

Table 6.2 Tensile properties of weld joints for all experiments

Test case	Heat input (kJ-mm^{-1})	CMF	UTS (MPa)	% Increase in UTS	% Elongation
Exp-1	0.42	No	306 ± 4	128	2
		Yes	697 ± 13		21
Exp-2	0.45	No	670 ± 20	9	19
		Yes	726 ± 6		23
Exp-3	0.48	No	633 ± 30	9	16
		Yes	691 ± 10		19
Exp-4	0.51	No	705 ± 3	3	20
		Yes	725 ± 15		20
Exp-5	0.36	No	371 ± 30	22	1
		Yes	452 ± 10		6
Exp-6	0.39	No	648 ± 10	12	3
		Yes	725 ± 5		24
Exp-7	0.41	No	461 ± 20	57	3
		Yes	722 ± 2		21
Exp-8	0.44	No	660 ± 2	10	4
		Yes	722 ± 15		22
Exp-9	0.32	No	327 ± 20	114	8
		Yes	699 ± 7		20
Exp-10	0.34	No	323 ± 8	125	8
		Yes	725 ± 15		23
Exp-11	0.36	No	316 ± 10	130	8
		Yes	723 ± 13		23
Exp-12	0.38	No	379 ± 70	90	11
		Yes	716 ± 4		21

In CMF assisted welds, the average tensile strength was improved by 59 % and elongation by 50 % as compared to conventional GTAW. Due to the fact that CMF aided welding is high energy density welding process, the HAZ is very small and it is the reason for higher UTS in CMF assisted welds [20]. The fracture location for all the magnetically influenced welds were at the base metal, and the UTS was almost equal to the base metal UTS. The CMF assisted welds helps in increasing the refinement of grains which itself acts as a strengthening mechanism to improve the mechanical properties as shown in Fig. 6.12b. In both the cases, the UTS is increasing with increase in weld current. But in case of without CMF, the weld joints were partially penetrated at lower heat inputs (i.e., at high welding speed) resulting in decrease of tensile strength as depicted in Fig. 6.12c. All the test specimens from experiment 5 to 12

were failed at weld joint due to lack of penetration. But in case of CMF assisted welds, the arc was narrower and more amount of energy was concentrated at a minimal area leading to achieve deeper penetrations for the same amount of heat input. The UTS was increased with increase in heat input for both the cases as shown in Fig. 6.12(c and d). The elongation of base metal was higher than the weld metal. The elongation depends on the amount of energy absorb during the tensile test. The CMF assisted welded samples exhibited much higher elongation than the welds without a magnetic field.

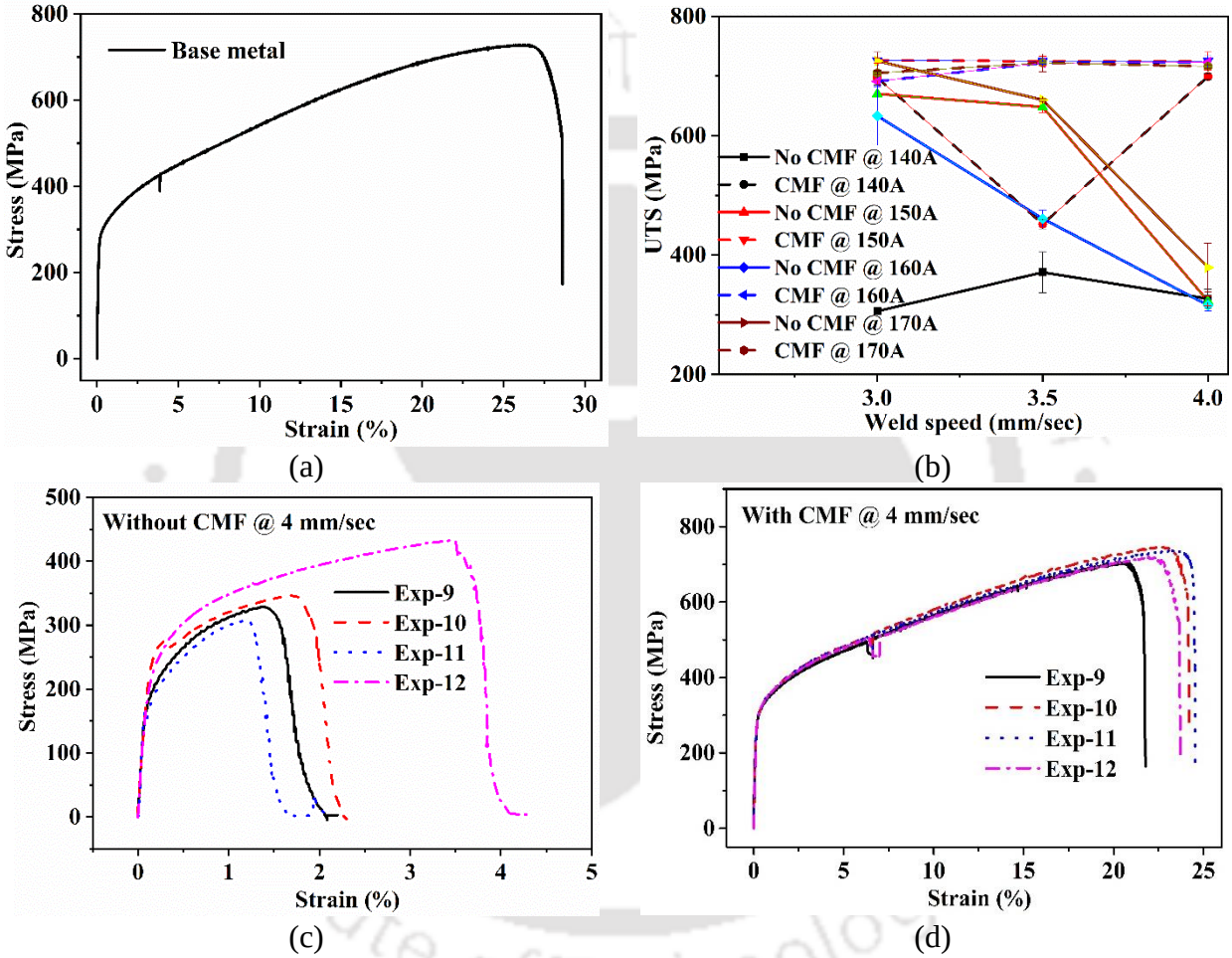

Fig. 6.12 (a) Tensile stress-strain graph of base metal, (b) weld speed vs UTS, and UTS at 4 mm/sec by varying current: (c) without CMF, and (d) with CMF

6.3.8 Fractography

The fracture morphology of the joints welded without and with the influence of magnetic field for Exp-10 are shown in Fig. 6.13. The tensile test of soft materials typically results in ductile fracture, which occurs in various stages. Initially, a cavity is nucleated and grows either in stably or unstably nature. Finally, the cavities interconnect, leading to the final fracture and the formation of a dimple at the fracture surface [122,123]. Both the welded samples exhibited

uniform dimples and their distribution indicates ductile mode of failure. Without the application of CMF, coarser dimples along with intergranular cleavage fracture were observed at lower welding speeds, as shown in Fig. 6.13a. In contrast, coalescence of finer and deeper dimples were observed in welds assisted by CMF as depicted in Fig. 6.13b. In conventional GTAW procedures, when welding speeds were increased to 4 mm/sec, partial depth of penetrations were achieved resulting in formation of shallow dimples, indicating that a minimum amount of energy was absorbed during failure, as depicted in Fig. 6.13c [124]. Finer and micro void dimples were formed in case of magnetic field assisted welds, resulting in maximum amount of energy absorbed during failure due to full depth of penetrations as shown in Fig. 6.13d. The major factors influencing the tensile strength are, the number of grains and their size in the microstructure. Nucleation and recrystallization are driven by the cusp magnetic field resulting in finer grains in the microstructure. The major factors influencing the tensile strength are, the number of grains and their size in the microstructure. Also, the amount of energy absorbed per unit area depends on the size of the dimple [125]. On calculating the number of dimples per mm^2, there was a significant increase in the density of dimples in CMF assisted welds. With increase in density of dimples, the grain boundary volumes increase with reduced grain size.

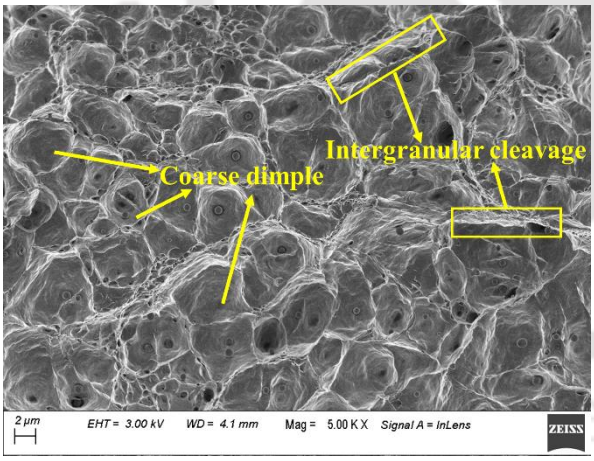

(a)

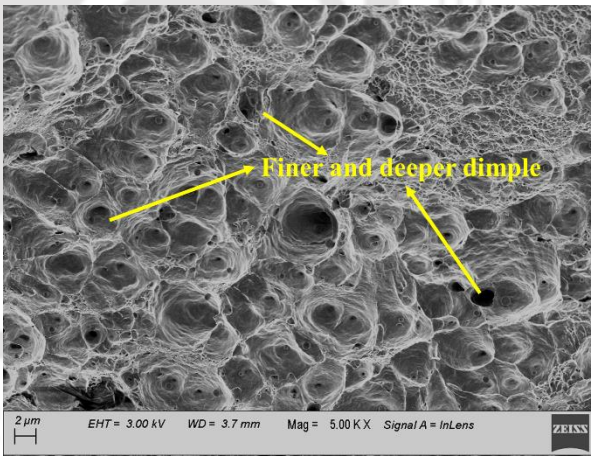

(b)

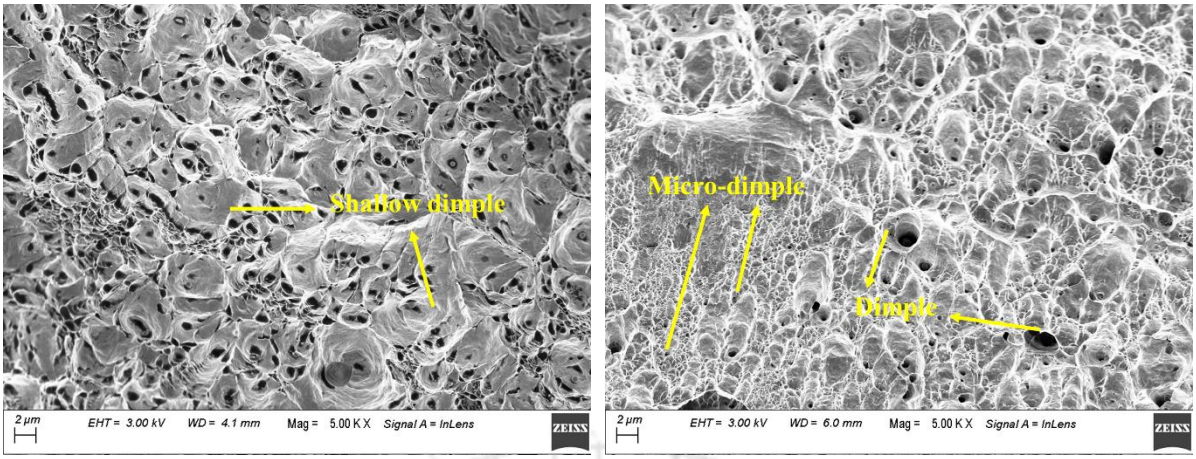

(c) (d)

Fig. 6.13 Fracture surface morphology of Exp-2: (a) Without CMF, and (b) With CMF; and Exp-10: (c) Without CMF, and (d) With CMF

6.3.9 Corrosion analysis

Experiments were performed in a potentiostat to analyze the corrosion resistance in 304 SS weldments using Tafel polarization curves. The potential was applied from -500mV to +500 mV at a scan rate of 1 mV s^{-1} to attain the anodic branch. The experimental curve was used to analyze the corrosion characteristics such as, corrosion current density (I_{corr}) and corrosion potential (E_{corr}). I_{corr} was derived from extrapolating the cathodic and anodic curves. The corrosion tests were performed for the best results achieved from the process parameters. Table 6.3, represents the corrosion potential and current density for the welding heat input of 0.45, 0.39 and 0.34 kJ-mm^{-1} for both with and without magnetic field. It can be clearly seen that the corrosion potential was higher and moving towards the positive side as shown in Fig. 6.14 (a-c), in CMF influenced welds. Also, the lower current density values were achieved as compared to conventional GTAW. From Faraday's law for corrosion rate, a better corrosion resistance can be attained at a lower corrosion current densities [126]. Hence, from Fig. 6.14(d), it can be concluded that higher corrosion resistance was achieved in CMF influenced welds. Corrosion resistance was majorly influenced by the alloying elements present in the fusion zone and HAZ. As the chromium (Cr) element was the major influencing one for corrosion resistance. But, for the experiments 2, 6 and 10, from the EDX analysis, the Cr quantity was significantly increased in magnetic field assisted welds as shown in Fig. 6.15. In fusion welding of 304 SS, the ferrite phase consists of Cr as the major constituting element in a heterogeneous distribution. By the application of CMF, distribution of alloying elements becomes uniform including Cr contents as compared to conventional welds [17]. Also, the austenite is a phase of paramagnetic and

their domains are oriented randomly. With the application of CMF to GTAW, an electromagnetic interaction takes place between the self-induced magnetic field and external magnetic field and this interaction induces vibration of the atoms [118]. This interaction on vibration of atoms also promotes the transformation of the ferrite to homogenized austenite matrix. Due to the homogenization of Cr element, the formation of Cr-depleted sites and precipitates of the Cr-rich carbides were reduced leading to improved passive film homogeneity over the surface of the weldment. This results in better corrosion resistance with lower corrosion current densities in CMF assisted welds. Also, by conducting EDX analysis, as shown in Fig. 6.16, the higher percentage of ferrite quantity were observed in conventional welds. Ferrite quantity was noticeably lesser in quantities and was distributed homogenously along the weld in CMF assisted welds was also a reason for better corrosion resistance in CMF assisted welds [117]. As depicted in Fig. 6.9 (d and e), maximum skeletal morphology and minimum lathy morphology δ-ferrite were formed in CMF assisted welds leading to better homogeneity in microstructure. This type of microstructure helped in improving corrosion resistance and a similar trend was also observed by Rong Chen et al. [17].

Table 6.3 Electrochemical properties of welded samples

Test case	Heat input ($kJ\text{-}mm^{-1}$)	Without CMF		With CMF	
		E_{corr}	I_{corr}	E_{corr}	I_{corr}
Exp-2	0.45	-0.143	-5.05	-0.101	-5.318
Exp-6	0.39	-0.114	-5.297	-0.09	-5.618
Exp-10	0.34	-0.193	-6.368	-0.109	-6.404

In both the cases, by increasing the heat input, corrosion current density was decreased (Fig. 6.14d) which indicates a better corrosion resistance, the similar trend was also observed by Lu, et al., [127]. At higher heat inputs, higher temperatures was achieved and sufficient amount of time allowed to transformation of ferrite to austenite. In addition to that, in case of CMF, the diffusion of heat was parallel through the fusion line without accumulating at boundary walls leading to narrower HAZ. The external magnetic field acted as a driving forces for nucleation and recrystallization, leading to finer grains in the microstructure. The narrower HAZ and finer grains also promoted the corrosion resistance [128].

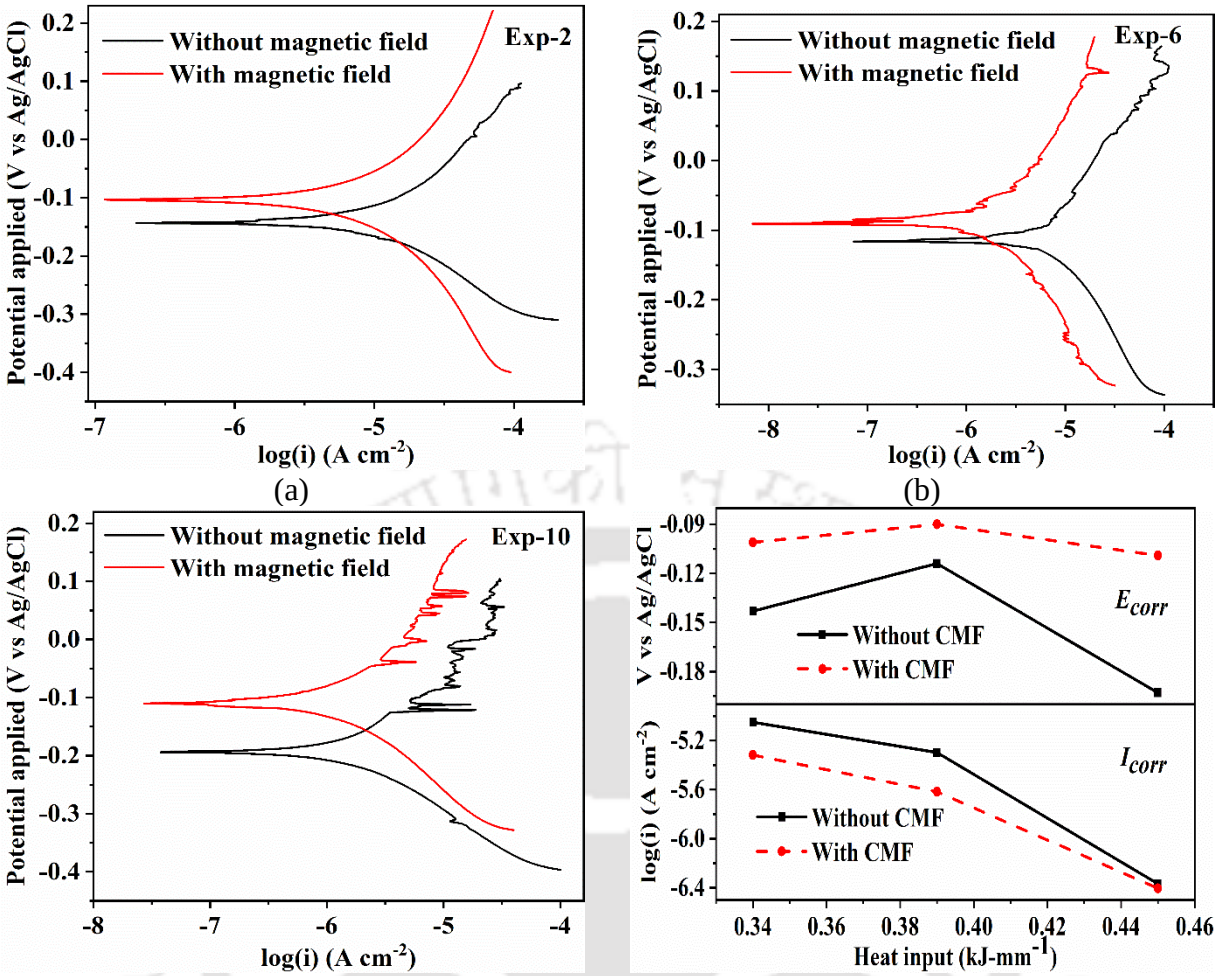

Fig. 6.14 Comparison of Tafel polarization curves: (a) Exp-2, (b) Exp-6, (c) Exp-10; and (d) effect of heat input on corrosion resistance

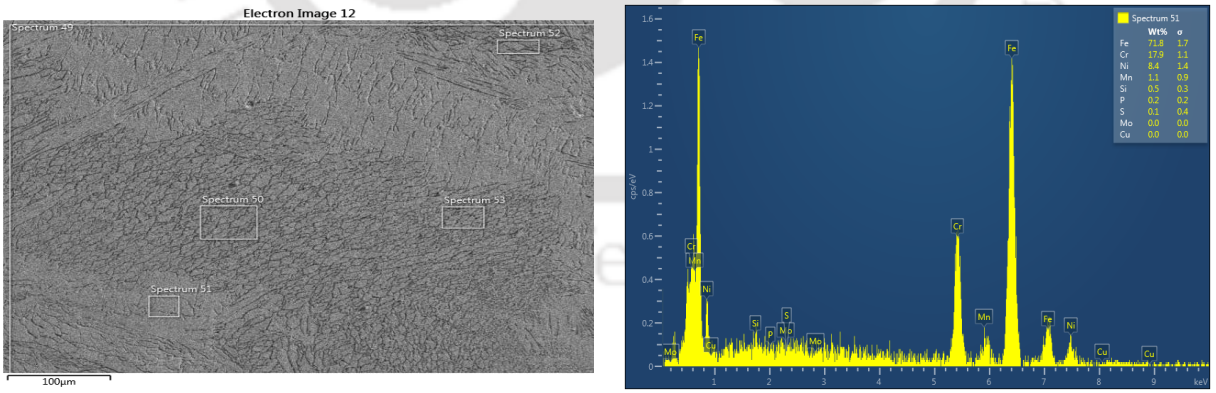

(a) (b)

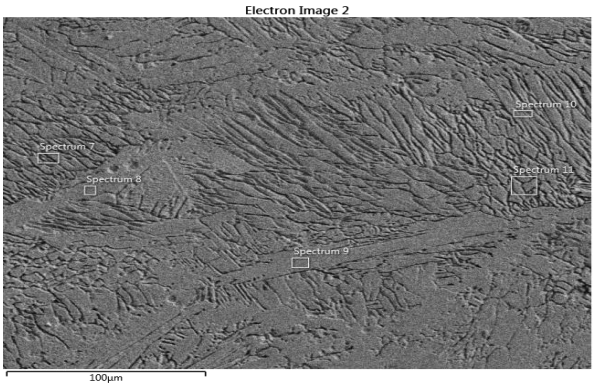

(c)

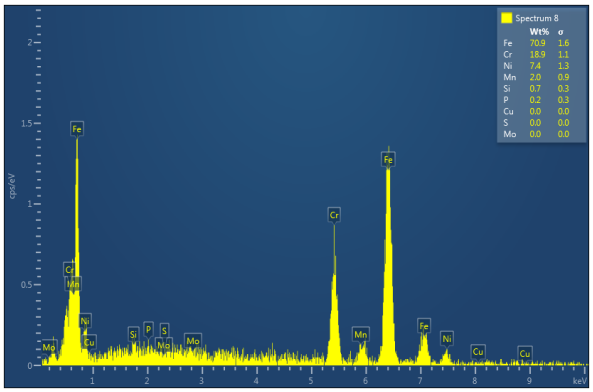

(d)

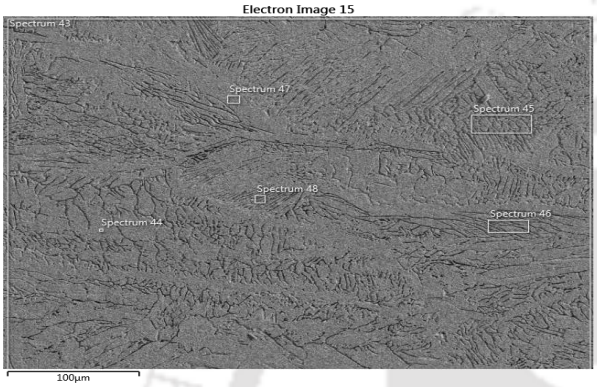

(e)

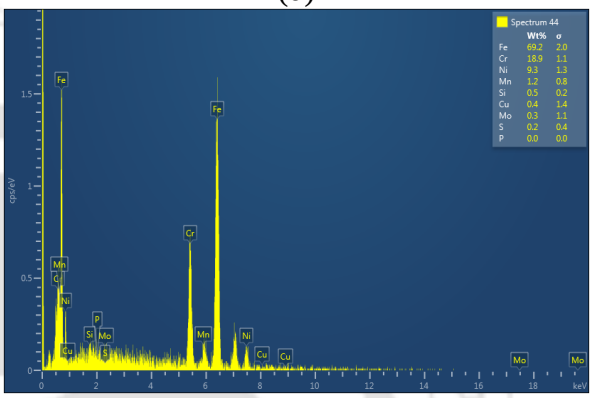

(f)

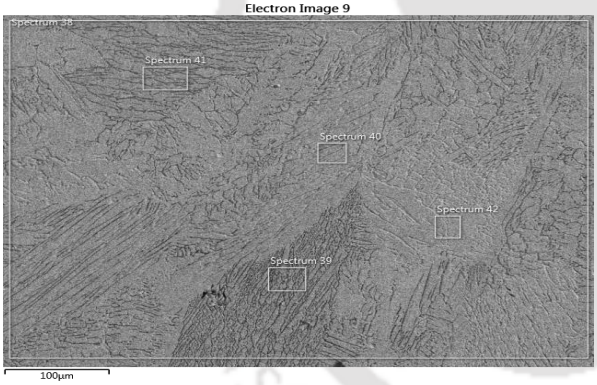

(g)

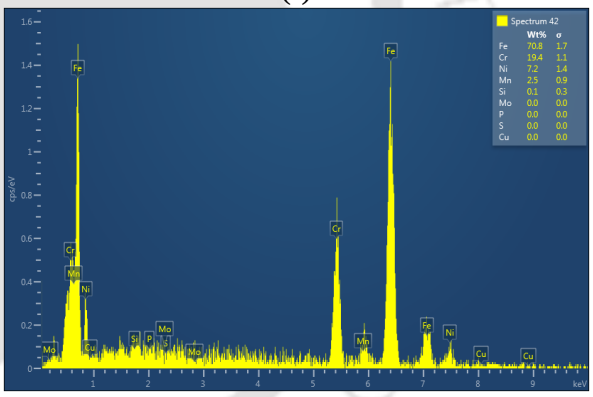

(h)

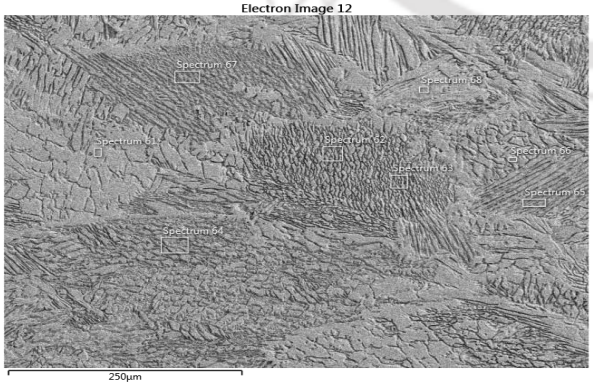

(i)

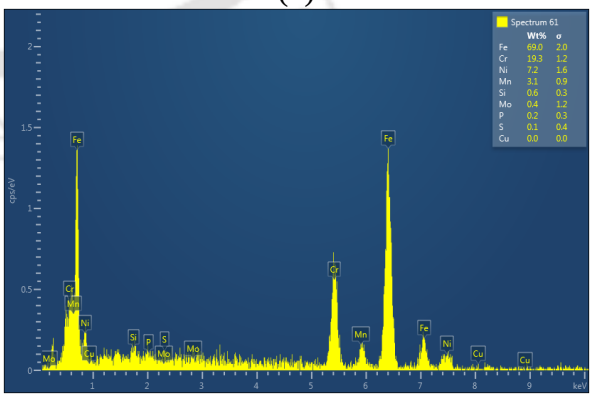

(j)

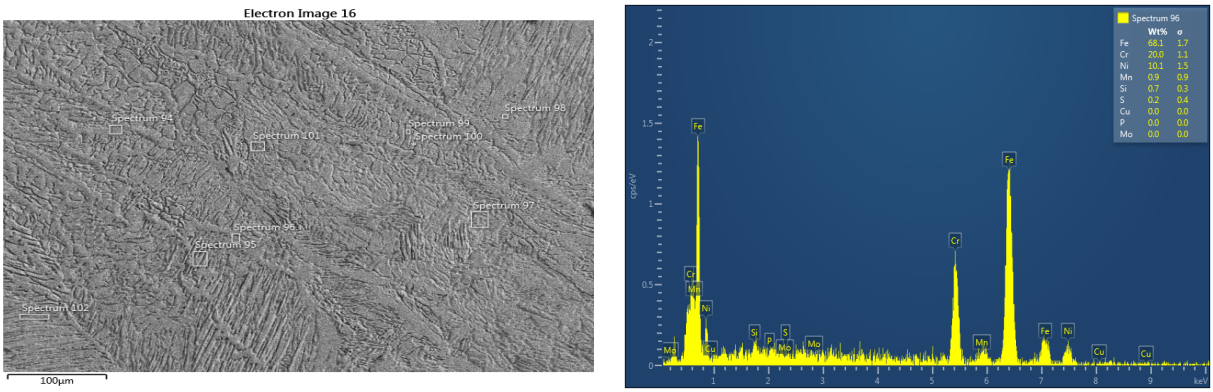

(k) (l)

Fig. 6.15 EDX analysis of corresion tested samples: without CMF - (a-b) Exp-2, (e-f) Exp-6, (i-j) Exp-10 and with CMF – (c-d) Exp-2, (g-h) Exp- 6, and (k-l) Exp-10

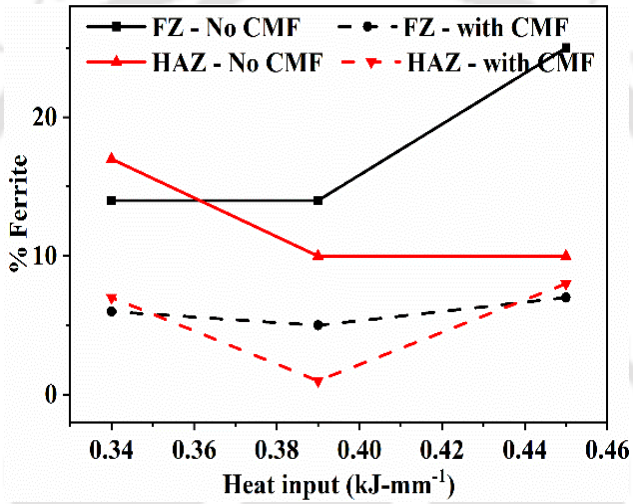

Fig. 6.16 Effect of heat input on ferrite percentage

6.4 Summary

With the application of CMF during GTAW, arc was constricted and the energy density within the arc was also increased. Effect of process parameters on the morphology and weld geometry were also studied and observed an improvement in the aspect ratio of the weld bead. Higher bead widths and depth of penetrations were observed at higher heat inputs in both the cases. The external magnetic field induced a stirring effect in the molten weld pool that leads to formation of higher quantities of δ-skeletal ferrite in the weldment. Average hardness in the fusion zone was marginally higher than the conventional GTAW welds due to the existence of higher quantity of δ-ferrite. Higher hardness in HAZ was observed in CMF assisted welds due to the presence of finer grains. UTS was increased by 59 % and more amount of energy was absorbed by the CMF assisted welds. Also, better corrosion rate was achieved due to homogenous distribution of alloying elements and minimal quantities of ferrite in the weldment. In summary,

the effect of magnetic field results in good improvement in metallurgical and mechanical properties of the weldment.

Chapter 7 Experimental Investigation of CMF Assisted GTAW of Dissimilar Steels of LCS and SS 304

7.1 Introduction

This study deals with the dissimilar gas tungsten arc welding of low carbon steels (LCS) and SS 304. In general, dissimilar metal welding of SS 304 to LCS has a wide application in industries such as boilers, pressure vessels and heat exchangers in power industry [56,58]. The major difficulty in traditional welding of dissimilar steels is caused by discrepancies in alloying elements composition, which result in solidification and segregation defects. In order to reduce the imbalances in alloying composition a magnetic field was introduced during GTAW of dissimilar steels. Microstructure and mechanical properties of dissimilar weld joints subjected to a magnetic field have not been reported in the past literature. After conducting experiments, weld joints were characterized by micro-hardness, ultimate tensile strength and EDX analysis. Experimental findings showed a better weld aspect ratio and homogenous distribution of alloying elements by the application of magnetic field to the weld.

7.2 Experimentation

For welding of dissimilar steels of LCS and 304 SS plates of 3 mm thickness, welding speed and current were taken as major process parameters along with cusp magnetic field. The base material chemical composition and joint preparation along with characterization process were discussed in chapter 4. By varying the process parameters, 12 experiments were conducted without using the external magnetic field. At the same process parameters setting, 12 more experiments were conducted using cusp magnetic field. The process parameters used in this study is presented in Table 7.1.

7.3 Results and discussion

7.3.1 Effect of CMF on weld macrostructure

Table 7.1, represents the various process parameters setting used for the welding of dissimilar steels and also the measured bead width (w), and depth of penetration (h). Figures 7.1 (a, b), (c, d) and (e, f) show the optical macrostructures of the specimens welded without and with the application of CMF for experiments 2, 6 and 10, respectively.

Table 7.1 Process parameters and geometry of fusion area

Test case	Current (A)	Weld speed (mm/s)	Heat input (kJ-mm^{-1})	No CMF		With CMF		% decrease in w	% increase in h
				w (mm)	h (mm)	w (mm)	h (mm)		
Exp-1	140	3	0.42	8.56	3.10	8.24	3.10	3.7	0
Exp-2	150	3	0.45	8.99	3.10	8.36	3.10	7.0	0
Exp-3	160	3	0.48	8.85	3.10	8.84	3.10	0.1	0
Exp-4	170	3	0.51	9.27	3.10	8.63	3.10	6.9	0
Exp-5	140	3.5	0.36	8.54	3.10	7.54	3.10	11.7	0
Exp-6	150	3.5	0.39	8.86	3.10	7.87	3.10	12.1	0
Exp-7	160	3.5	0.41	8.96	3.10	8.12	3.10	9.4	0
Exp-8	170	3.5	0.44	9.00	3.10	8.20	3.10	8.9	0
Exp-9	140	4	0.32	7.96	2.75	7.34	3.10	7.8	9.1
Exp-10	150	4	0.34	7.86	1.39	7.41	3.10	5.7	115
Exp-11	160	4	0.36	7.98	3.10	7.81	3.10	2.1	0
Exp-12	170	4	0.38	8.40	3.10	8.12	3.10	3.3	0

Higher bead widths were found in the specimens welded without the application of external magnetic field. An average of 7 % decrement in weld bead width was observed in CMF assisted welds. There was no significant difference in the depth of penetration for both the cases, except at lower heat inputs. In exp-9 and Exp-10, a partial penetration was observed due to lower heat inputs of 0.32 and 0.34 kJ-mm^{-1}. For the same amount of heat input, full penetrations were achieved in the welds with the application of CMF due to the increase in energy density of the arc.

For the same amount of heat input in similar SS 304 weldments (from exp-5 to exp-12), a partial depth of penetrations were observed as presented in chapter 6. However, in dissimilar welding higher depth of penetrations were achieved. This may be due to the difference in thermal conductivity of the LCS and SS 304, the SS 304 melted in less time and the molten pool temperature of SS 304 helped in melting the LCS side, leading to full penetrations.

Test case	Without CMF	With CMF
Exp-2	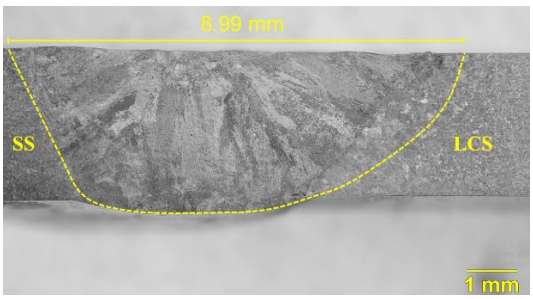	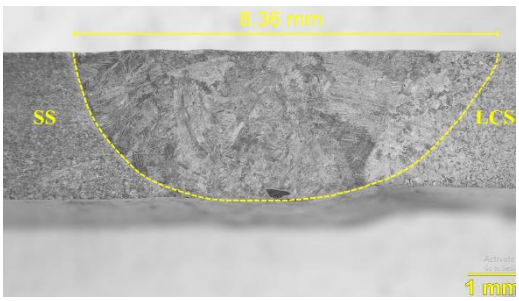

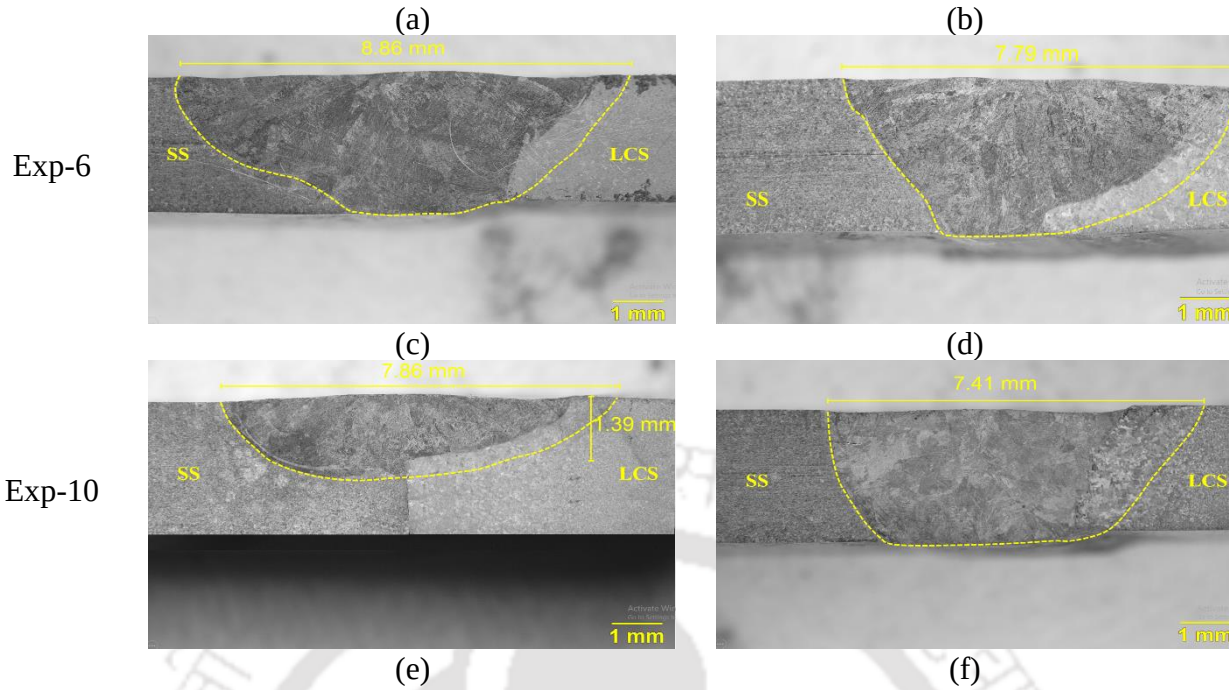

Fig. 7.1 Comparison of transverse weld profiles at different weld speeds: (a-b) 3 mm/s, (c-d) 3.5 mm/s, and (e-f) 4 mm /s at 150 A

The minimum weld bead width was observed at higher welding speed and lower current (*i.e*, at low heat input) as shown in Fig. 7.2. In both the cases, increasing the welding current leads to more heat input per unit length. This resulted in melting of larger volumes of base metals thereby wider bead widths were formed as shown in Fig. 7.1. Also, with reducing the welding speed, bead width was increased due to enhancement of weld line energy per unit length. As discussed in the previous chapters, with the application of CMF, the arc was compressed along the transverse direction and stretched towards the welding direction, leading to concentration of arc energy on the minimal transverse area. This led to form narrower weld beads in CMF assisted welds as compared to conventional welds.

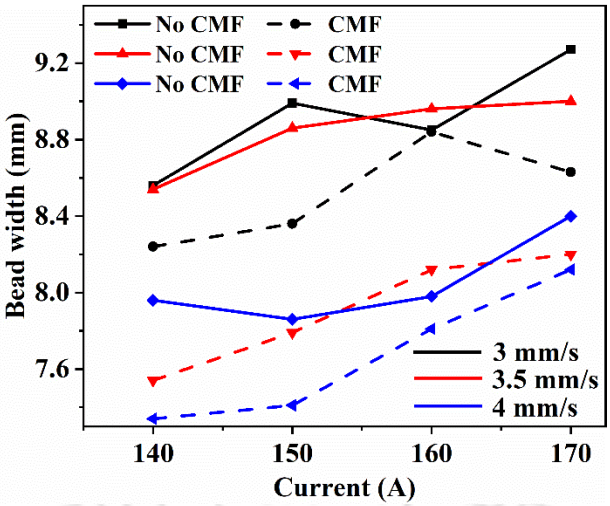

Fig. 7.2 Effect of welding current on weld bead width

7.3.2 Thermal analysis

To measure the temperature, K-type thermocouples were placed on both the plates at a distance of 6.5 mm from the centerline of the weld. Figure 7.3, represents the temperature profiles of the LCS and SS 304 plates welded under both with and without the influence of CMF. With increasing heat input in both the cases, the transverse peak temperatures were increased. By increasing the heat input from 0.34 kJ-mm^{-1} to 0.45 kJ-mm^{-1}, the peak temperatures were raised from 618 °C to 888 °C on LCS side and 493 °C to 672 °C on SS304 side, in conventional GTAW welds. In case of CMF assisted welds, the temperatures were raised from 620 °C to 847 °C on LCS side and 493 °C to 770 °C on SS 304 side. Also, the peak temperatures were high on LCS as compared to SS 304 side. This is due to the higher densities, specific heat capacity, melting point and lower thermal conductivity of the SS 304 material that leads to low heat distributions during the welding process as compared to low carbon steel. The lower heat conductivity of SS 304 resulted in faster heating and melting of the metal before the melt pool formation of the LCS [54]. This can contribute to the formation of initial melt pool in the dissimilar weld. The cooling rate was faster in LCS side due to higher thermal conductivity of the material. In the molten pool, the fluid flow is generally influenced by magnitudes of velocity, surface tension and buoyancy forces. An efficient heat transfer in the melt pool from the weld center to its periphery was due to its negative surface tension coefficient. And the velocity rates in the melt pool determines the temperature gradients. From Fig. 7.3, we can observe the higher thermal gradients in the LCS due to its higher thermal conductivities leading to negative surface tension in the molten pool.

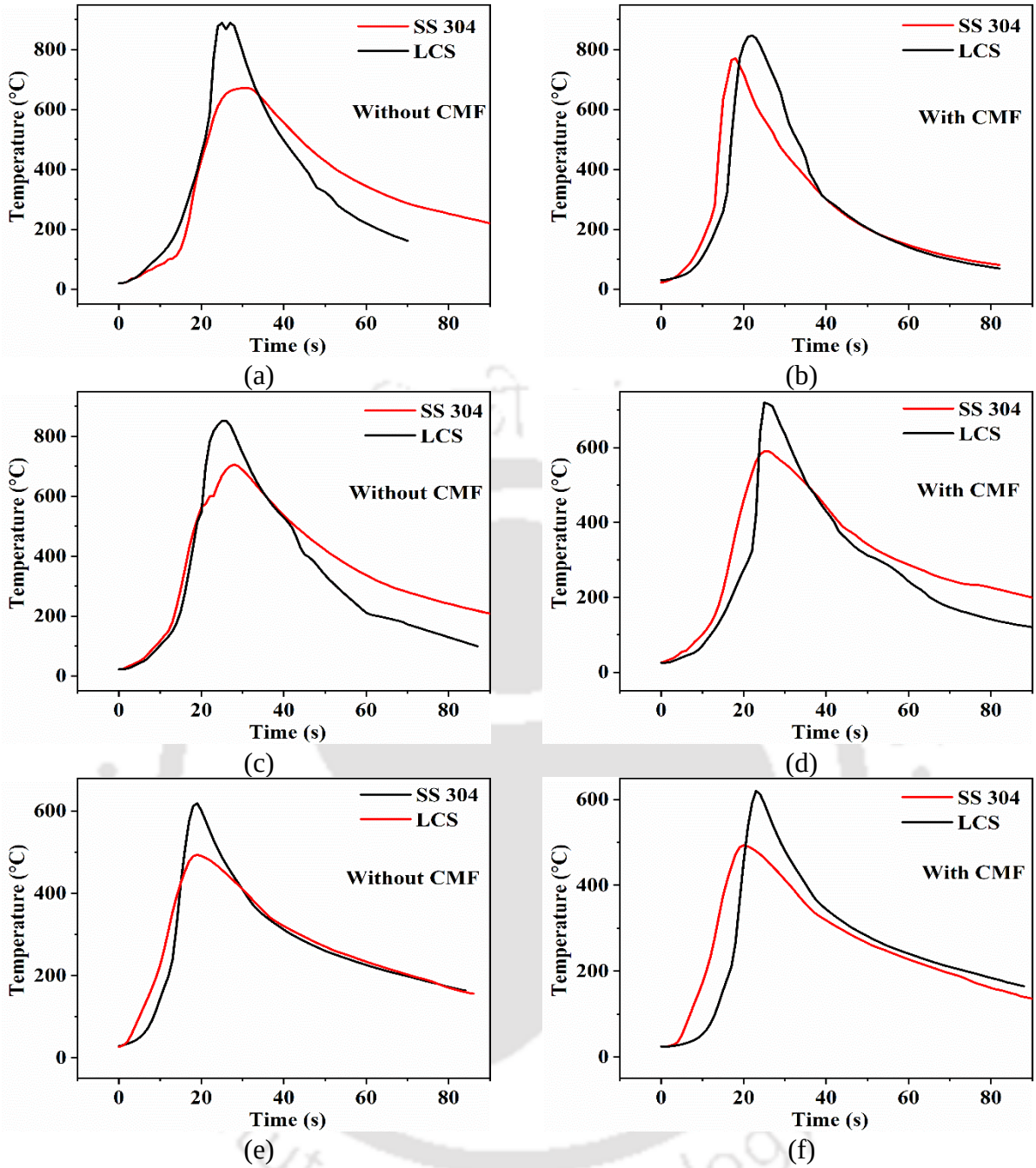

Fig. 7.3 Comparison of weld thermal cycles on LCS and SS 304 plates without and with the effect of CMF: (a-b) Exp-2, (c-d) Exp-6, and (d-e) Exp-10

In the absence of CMF, due to the interactions from the temperature field and self-inductance magnetic field, the charge particles of the welding arc have a specific spiral radius along the symmetry of its own axis. With the application of cusp type magnetic field during welding produces many effects. Firstly, an additional Lorentz force is created along the welding arc charged particles causing them to rebalance and attain a state of re-equilibrium. This results in the constriction of arc leading to higher arc energy densities within the arc space. Secondly, anti-gravity gradient is produced by the arc within the cathode and anode thereby reversing the

arc flow leading to a low temperature zone formation at center of arc on anode [29]. And mainly, it produces an electromagnetic stirring effect in weld pool thereby increasing the convection within the weld pool resulting in higher thermal conductivity of molten metal. Due to higher convection rates, heat transfer in weld pool is increased resulting in decrement of peak temperatures as shown in Fig. 7.3 [111,129].

7.3.3 Microstructure and EDX analysis

The mechanical and service performance of the dissimilar welded joint strongly depends on the weld zone microstructure. Figure 7.4 (a, b) represent the microstructure of base metals of LSC and SS 304. Figure 7.4 (c, d) depicts the HAZ microstructure of SS 304 of conventional GTAW and CMF assisted GTAW and Fig. 7.4 (e, f) represents the HAZ grain structure of the LCS in both the cases. In conventional GTAW, nucleation effect was observed in the HAZ of LSC side in which the grains become finer as moving away from the fusion zone towards mild steel base metal. These grains were recrystallized near by the fusion zone and nucleated away from these recrystallized grains. The grains on the LCS side of the HAZ became finer as one moves from the fusion zone to the base metal indicating a nucleation effect. Also, with an increase in welding speed, the grain size was reduced in both the cases in LCS side as shown in Fig. 7.5. Width of the HAZ in SS 304 was considerably less as compared to LCS HAZ. Figure 7.4 (e, f), represents the HAZ thickness for both conventional and CMF assisted welds. The HAZ was narrower and finer grains were observed in CMF welds for same amount of heat input. By the application of CMF, these zones were further reduced in the weldments leading to better mechanical properties. The major phases observed in fusion zone of both the cases were ferrite, acicular ferrite (AF) and Widmanstatten ferrite (WF).

With the application of external magnetic field, homogeneity in microstructure was observed in the fusion zone by forming equiaxed grains and large quantities of AF and WF were observed compared to conventional GTAW as shown in Fig. 7.6. At higher heat inputs, wider WF structure was attained in the fusion zone, leading to higher hardness. The formation of microstructure and behavior of molten metal in the weld pool including the formation of skeletal and lathy morphology were discussed in the previous chapter.

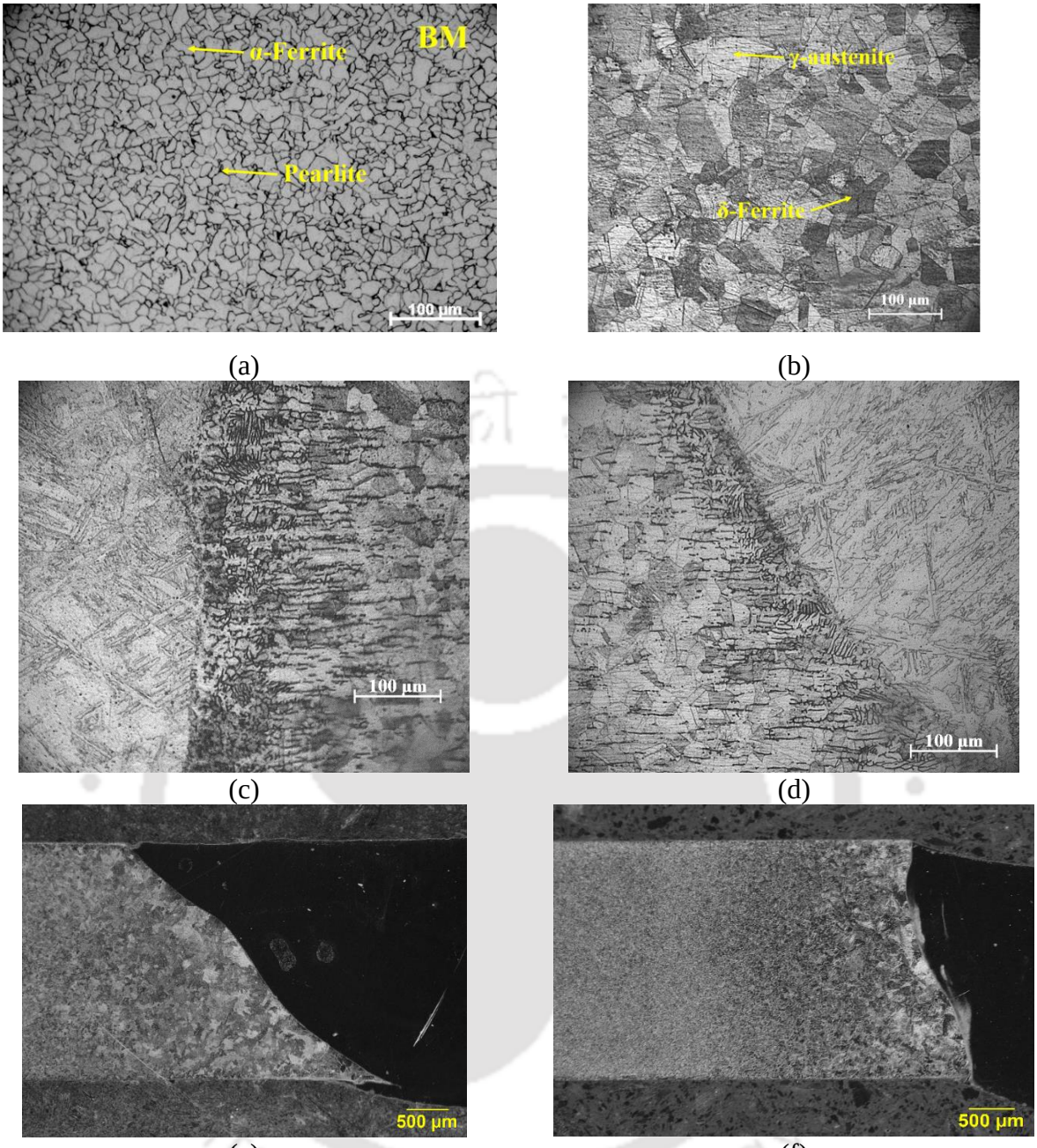

Fig. 7.4 Base material microstructure: (a) LCS, (b) SS 304; HAZ microstructure without CMF: (c) SS 304, and with CMF: (d) SS 304; HAZ microstructure of LCS: (e) without CMF, and (f) with CMF

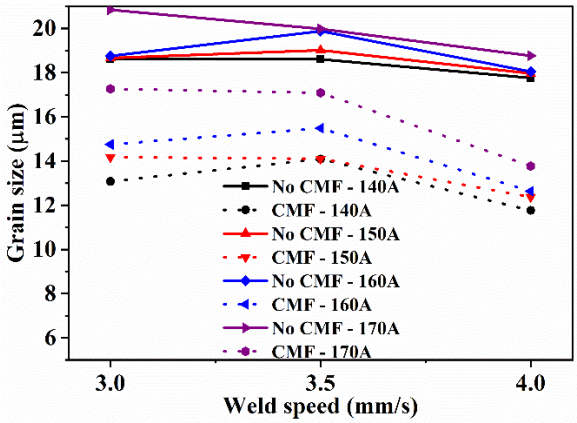

Fig. 7.5 Effect of weld speed on grain size

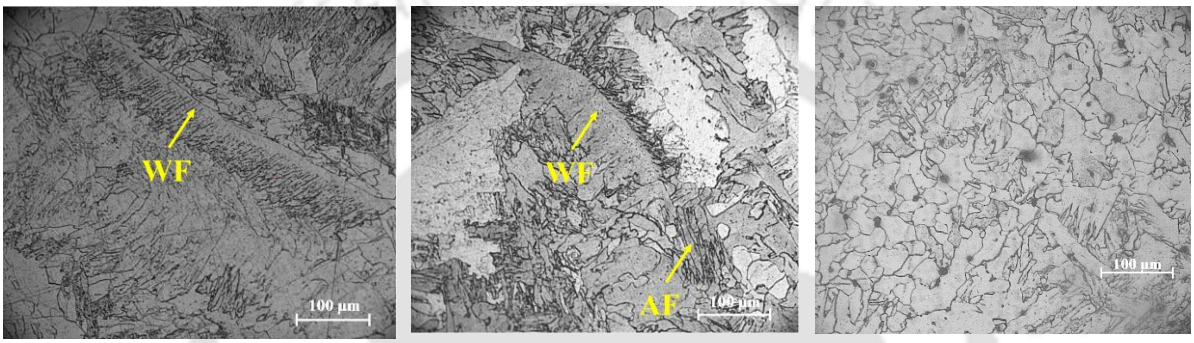

(a) (b) (c)

Fig. 7.6 Fusion zone microstructure on LCS: (a) without CMF, (b) with CMF, and (c) equiaxed grain structure in the HAZ side of LCS

Figure 7.7 represents the EDX analysis of the experiments 2, 6 and 10 on the LCS side of the weld zone. The alloying elements like Cr and Ni, which are constituent elements of the parent SS 304 plate, were not found in the LCS side of the fusion zone in conventional GTAW. With the application of CMF, stirring action in the molten pool caused the uniform distribution of alloying elements including Cr contents as compared to conventional welds [17]. By decreasing heat input, in both the cases, the narrower weld bead was formed. Due to narrowed weld beads, the convection rates and molten pool flow velocities were high resulting in transferring the alloying elements across the weld pool. As shown in Fig. 7.7, the increment of Cr, Ni elements and decrement of ferrite quantity on the LCS side were observed in both the cases. The presence of alloying elements and reduction of ferrite quantities were high in CMF assisted welds as compared to conventional welds. With the application of CMF, an electromagnetic interaction took place between the self-induced magnetic field and external magnetic field and this interaction induced vibration of the atoms as discussed in previous chapter. The elements concentration profiles at the interface specify that, stainless steel diffused slightly in the softer mild steel alloy but negligible mild steel diffused in the harder stainless steel. The diffusion of

such elements (Cr and Ni) indicates the dissimilar weld of the materials are chemically and mechanically bonded to collectively contribute to the weld integrity.

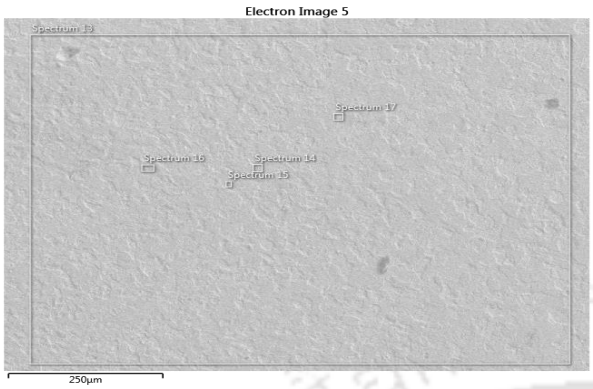

(a)

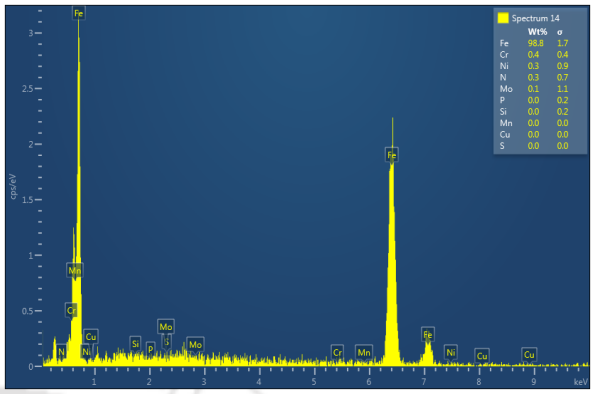

(b)

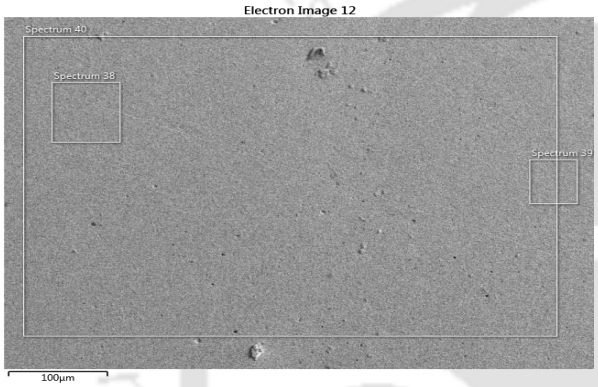

(c)

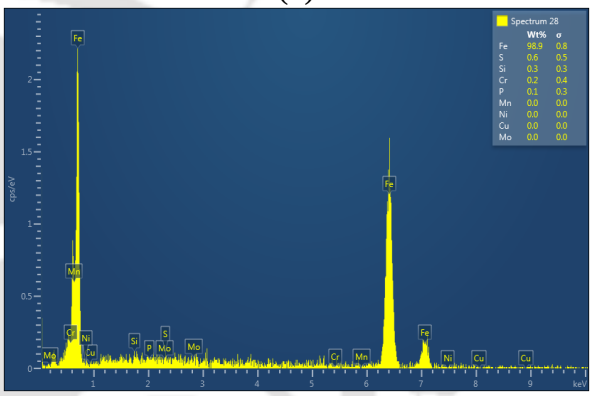

(d)

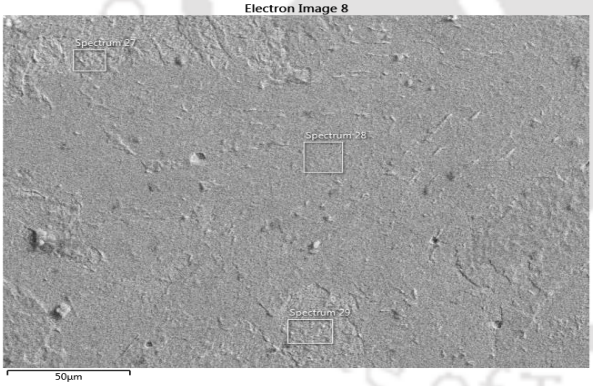

(e)

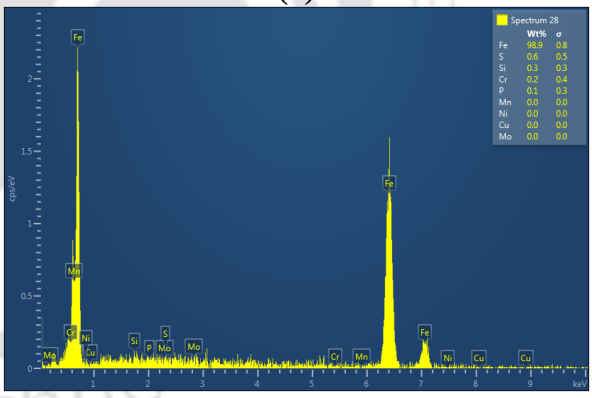

(f)

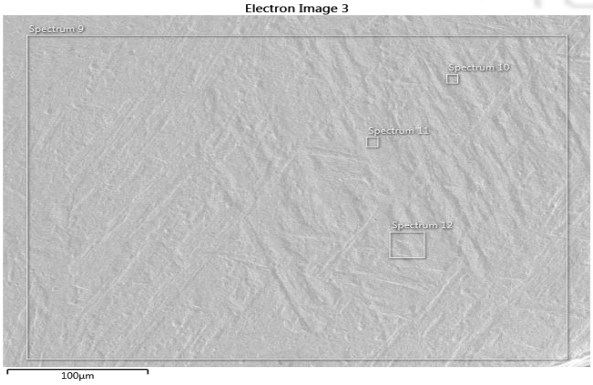

(g)

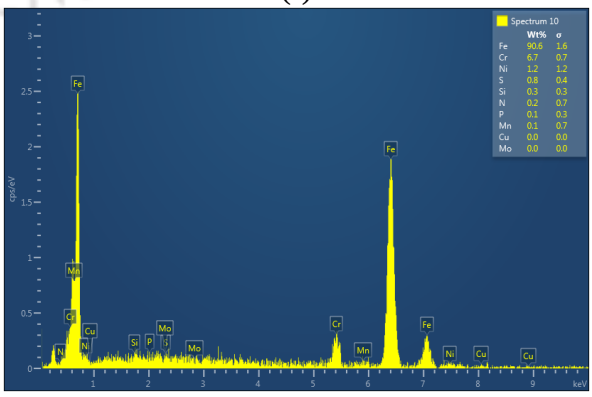

(h)

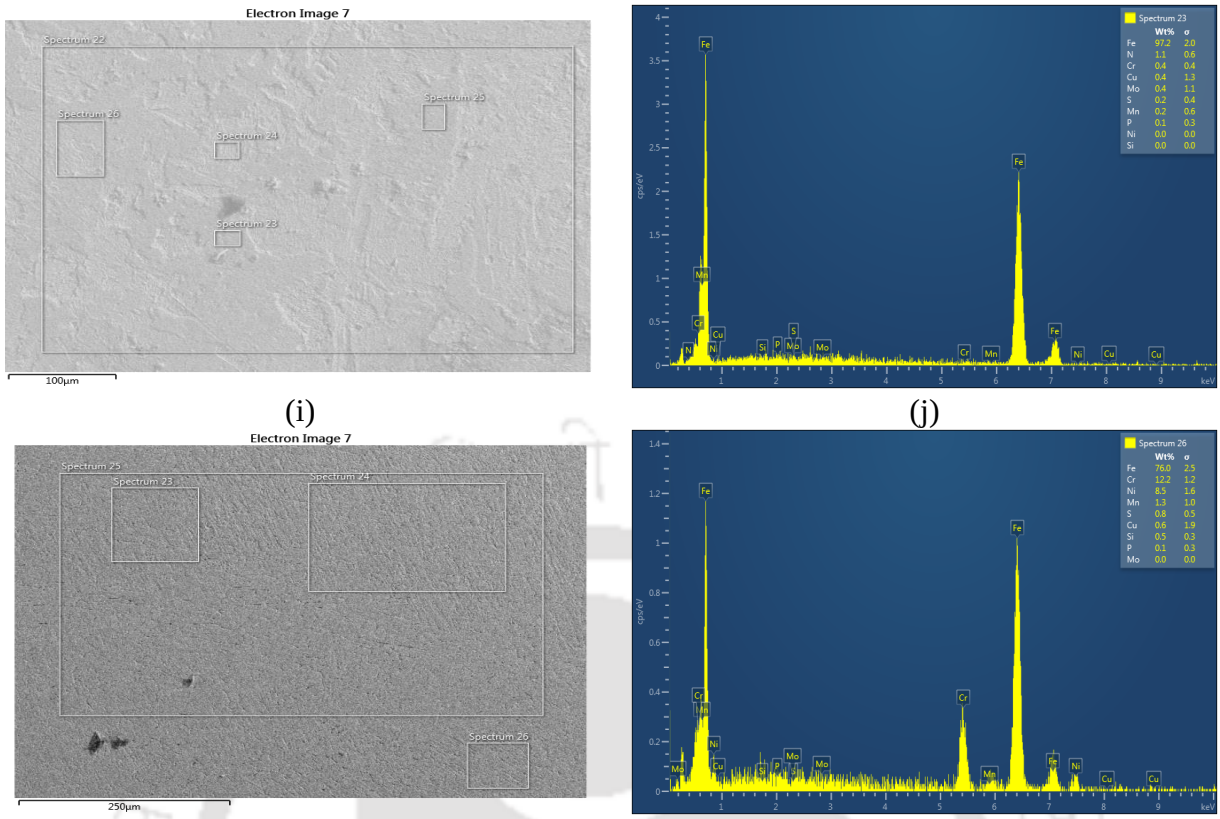

Fig. 7.7 EDX analysis: without CMF - (a-b) Exp-2, (e-f) Exp-6, (i-j) Exp-10 and with CMF – (c-d) Exp-2, (g-h) Exp- 6, and (k-l) Exp-10

7.3.4 Hardness

Figure 7.8 (a-c) depicts the micro-hardness profile of welds for both with and without magnetic field at a gap of 1 mm transverse to the welding direction from the center of weld to base metal in both the sides for Exps-2, 6 and 10. Based on the microstructural changes in the weld, the fusion zone, HAZ, and base metal were identified, as shown in the hardness graph.

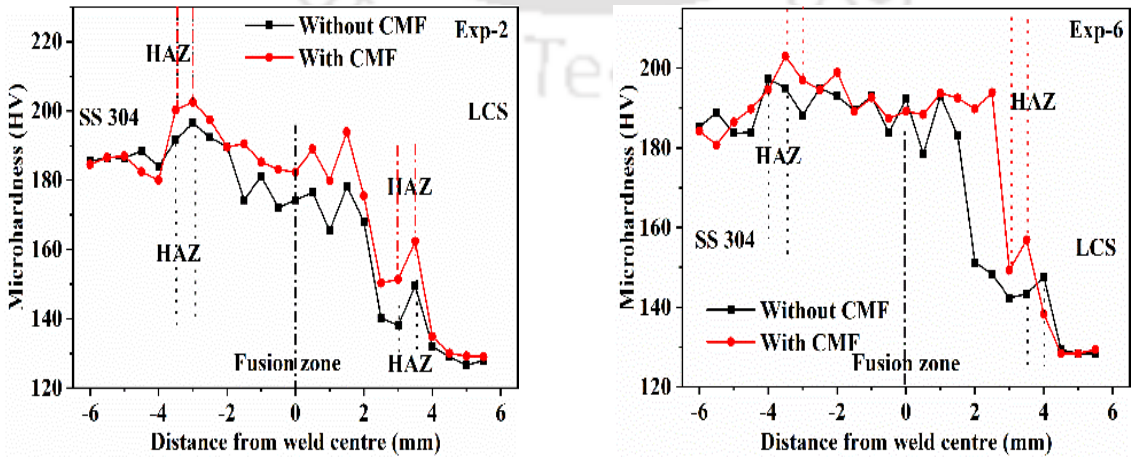

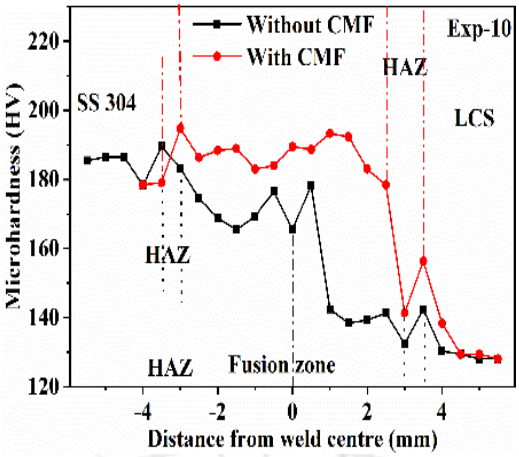

(c)

Fig. 7.8 Comparison of hardness between two welding cases (a) Exp-2, (b) Exp-6, and (c) Exp-10

The hardness in the fusion zone and HAZ were higher than the LCS base metal. In SS 304 side, the higher hardness values were also observed in HAZ and followed by fusion zone. But these hardness values were slightly higher than the base material. In both the base metals, the hardness values were slightly less in the outer side of HAZ (soft zone). In the fusion zone, maximum hardness was exhibited in the SS 304 side. In conventional welding, γ-phase present in the fusion zone of SS 304 was substituted by a low hardened δ-γ microstructure leading to decrease in hardness. The major phases observed in the fusion zone of both the cases were ferrite, acicular ferrite (AF) and Widmanstatten ferrite (WF). By the application of external magnetic field, homogeneity in microstructure was obtained in the fusion zone by forming equiaxed grains and large quantities of AF and WF compared to conventional GTAW. At higher heat inputs, wider WF structure was attained in the fusion zone, leading to higher hardness. The weld zone towards the LCS majorly consisted of WF and acicular ferrite resulting in higher hardness. Also, hardness instability was high in LCS side, due to partial inclusions of harder SS 304 alloying elements. But in CMF assisted welds, due to refinement of grains in HAZ, the hardness was slightly higher as compared to conventional GTAW as per Hall-Petch formulae. A homogeneous distribution of hardness was observed in CMF welds due to stirring action and homogenized elemental distribution in the molten pool as discussed in previous chapter. As the arc was converged and elongated in the welding direction, the arc itself acted as a pre-heat source and the trailing edge acted as a post-heat source. Preheating the base metal resulted in higher hardness and post-heating of weld pool resulted in uniform hardness in the fusion zone as compared to conventional GTAW. Also, due to grain refining, there was an increased in grain boundaries which leads to restriction of dislocation moment, thereby increasing the mechanical properties of the weld [115].

7.3.5 Tensile properties

The tensile properties for each heat input condition were measured and presented in Table 7.2. The presence of yield point phenomena was observed in the base material of LCS. However, this phenomenon was absent in both conventional and CMF assisted welded samples. Figure 7.9 (a-b) represents the UTS of LCS and SS 304 materials. All the welded samples were failed in ductile mode on the base metal of LCS. It indicates that, all the joints exhibited good UTS.

Table 7.2 Tensile test results for weld joints for all experiments

Test case	Heat input (kJ-mm^{-1})	CMF	UTS (MPa)	% Increase in UTS	% Elongation
Exp-1	0.42	No	375 ± 2	1.2	6
		Yes	380 ± 1		5
Exp-2	0.45	No	375 ± 1	3.6	5
		Yes	389 ± 4		6
Exp-3	0.48	No	360 ± 2	4.9	6
		Yes	378 ± 2		4
Exp-4	0.51	No	374 ± 4	10.3	5
		Yes	389 ± 0		5
Exp-5	0.36	No	362 ± 2	2.3	6
		Yes	370 ± 1		16
Exp-6	0.39	No	381 ± 1	1.9	10
		Yes	384 ± 5		7
Exp-7	0.41	No	377 ± 0	2.3	5
		Yes	386 ± 4		6
Exp-8	0.44	No	370 ± 2	3.5	5
		Yes	383 ± 9		5
Exp-9	0.32	No	357 ± 6	4.7	15
		Yes	374 ± 0		10
Exp-10	0.34	No	364 ± 1	2.7	5
		Yes	374 ± 1		5
Exp-11	0.36	No	365 ± 0	1.5	0
		Yes	370 ± 1		5
Exp-12	0.38	No	362 ± 2	4.6	5
		Yes	378 ± 4		6

The maximum tensile strength found was almost 100 % of the base metal strength for a heat input of 0.51 kJ-mm^{-1} in CMF assisted weld. An increment of 10 % in UTS was observed for CMF assisted welds. On an average of all the experiments, 4 % increment in UTS was observed. In CMF assisted welds, as shown in Fig. 7.3, it can be observed that the soaking periods were longer at peak temperatures than conventional GTAW process. It helped in refinement of grains which itself acted as a strengthening mechanism to improve the mechanical properties of the CMF assisted welds. Furthermore, the weld's tensile strength is

directly related to the presence of equiaxed grains in the microstructure. The density of grains can be increased by reducing the grain size. Higher the density of grains, the distribution of stress on the grains is better leading to increase in the overall stress level of a weld. By increasing the welding speed, heat input decreases. As the heat input decreased, the UTS was reduced accordingly in both the cases as shown in Fig. 7.9c. Likewise, in similar welding of LCS and SS 304, the UTS in dissimilar welding was not increased dominantly. The % elongation of the weld joints were lower than the base metals, similar results were found for LCS and SS304 weld joints. This was due to the formation of pearlite and acicular ferrite in the LCS side.

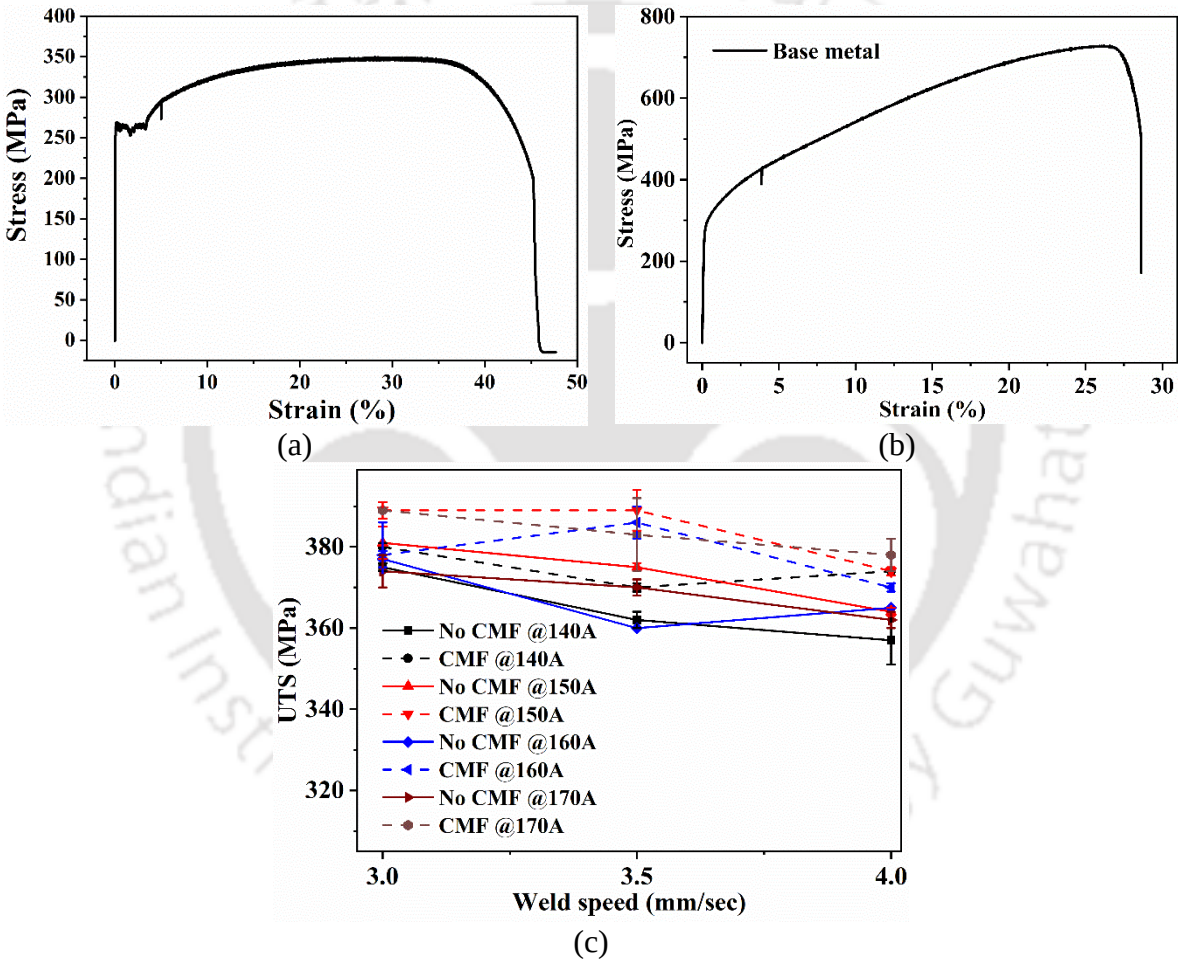

Fig. 7.9 Tensile stress-strain graph of base metal: (a) LCS, (b) SS 304 and (c) variation of UTS with welding speed

7.3.6 Fractography

Failure analysis of the samples made with and without the effect of external magnetic field were determined by using FESEM images as shown in Fig. 7.10. Fractography showed the distribution of different sizes of dimples indicating the ductile mode of failure. Size of the

dimples reflect the amount of energy absorbed per unit area. Volumes of grain boundary increased with decrease of grain size. In the magnetic field-assisted weld, higher density of small and shallow dimples were observed resulting in increase of tensile strength and ductility. On calculating the number of voids per mm^2 [20], there was significant increase in the number of voids for the sample welded under magnetic field compared to the sample welded without magnetic field. Increase in number of voids improved the strength of the joint.

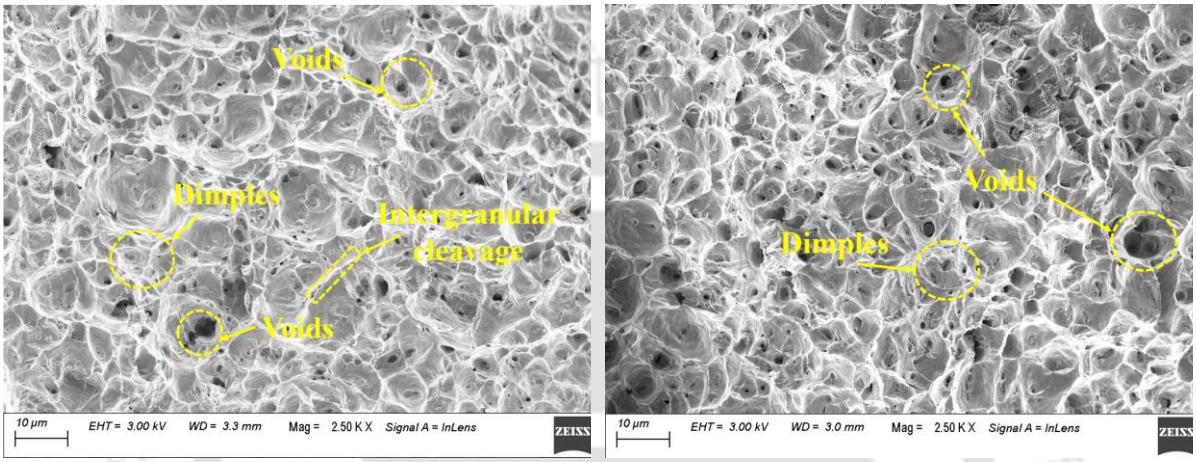

(a) (b)

Fig. 7.10 Fracture surface morphology of low carbon steel for Exp-5 (a) Without CMF, and (b) With CMF

7.4 Summary

In CMF assisted GTAW, arc was constricted and the arc force, energy density within the arc increased which further increased the plasma density within the arc. The effect of process parameters on the bead width and depth of penetration was studied. An improvement in the aspect ratio of the weld bead was observed. With increasing heat input, weld bead and grain size were increased in both the cases. Due to external magnetic field, stirring action in the molten pool led to formation of higher quantities of δ-skeletal ferrite in the weldment. Hardness in the fusion zone and HAZ was marginally higher than the base metal in the SS 304 side and significantly higher in the LCS compared to its base metal. The higher hardness in HAZ was observed in CMF assisted welds due to the presence of finer grains. UTS was increased by 4% and more amount of energy was absorbed by the CMF assisted welds. Also, homogenous distribution of alloying elements in the fusion zone was observed. In summary, the effect of magnetic field results, good improvement in metallurgical and mechanical properties of the weldment but not as better as similar welds.

Chapter 8 Conclusions and Future scope

8.1 Conclusions of the present work

In the present study, an external magnetic field is succesfully applied to gas tungsten arc welding (GTAW) process for conducting experiments in butt joint configuration. Similar welding of low carbon seels (LCS), stainless steel of grade SS 304, and dissimilar welding of LCS and SS 304 are conducted under the influence of both with and without magnetic field. The main objectives of the presetnt study are to better understanding of the effect of magnetic field on arc shape, arc-material interaction phenomena and correlate the mechanical characteristics of the welded samples with their microstructure, weld bead geometry and welding parameters. A 3D finite element model (FEM) is developed to simulate the magnetic flux density distribution around the electrode. A specially designed fixture is used to assist the cusp magnetic field to GTAW process. The welded samples are prepared for mechanical testing in accordance with ASTM E8 standards to measure ultimate tensile strength (UTS), yield strength, and elongation percentage. With the application of CMF using premanent magnets to a GTAW process results in the change of arc shape and improvement in mechanical properties. The salient findings and conclusions of the present work are highlighted below.

- The specially designed magnetic fixture along with permanent magnets was succesfully used to produce cusp magnetic field configuration around the electrode of GTAW.
- With the appliaction of CMF, the amount of energy density within the arc is increased. Also, the arc is stretched towards the welding direction in an elliptical cross-section leading to smaller contact of the heating area resulting in a narrower weld pool. A maximum of 6.15 % reduction in weld bead and 29.13 % increment in depth of penetration are observed in LCS, at heat inputs of 0.37 kJ-mm^{-1} and 0.32 kJ-mm^{-1}, respectively.
- Compression of arc results in steeper thermal gradients, thereby an increase in the undercooling that resulting in refinement of grains. Due to grain refining, grain boundaries increase and that leads to restriction of dislocation moment, thereby increasing the mechanical properties of the weld.
- CMF influenced GTAW has no significant amount of phase change in the weld. But the volume fraction of Fe_3C and Fe_2C are lower in the CMF assisted welds of low carbon steels.

- The compressed arc itself acts as a source of pre and post-heating to the ambient base metal. Higher convection rates resulted in the decrement of weld peak temperatures during application of CMF to GTAW.
- Increase in grain size is proportional to the amount of heat input. Lower heat inputs result in finer ferrite in magnetically influenced samples.
- UTS increases by 3% and 8% for two different heat inputs under CMF influenced GTAW. The decrement in size of dimples and an increase in density of dimples are observed in magnetically influenced welded samples resulting in higher mechanical properties.
- In similar welding of SS 304, weld bead width is reduced by 13% and depth of penetration is increased by 37% under the influence of cusp magnetic field. Bead width and depth of penetration increase with increasing heat input for both the cases.
- Stirring action in the molten pool leads to higher convection rate resulting in lower peak temperatures in magnetic field assisted welds.
- The amount of δ-ferrite is reduced in CMF assisted welds due to moderate cooling rates. Austenite is precipitated and grow within the ferrite boundaries resulting in increment of austenite phase in SS 304 weldments.
- Homogenous diffusion through fusion zone in CMF assisted GTAW, leads to finer grains in HAZ and narrower fusion zones.
- Amount of δ-lathy ferrite morphology is high in conventional welds due to higher cooling rates and δ-skeletal ferrite morphology is more in magnetic field assisted welds.
- Phase analysis reveals that, minimal quantities of δ-ferrite is present in both the cases. And dislocation densities are higher in CMF assisted welds indicating the presence of refined grains.
- The fusion zone average hardness is marginally higher than the conventional GTAW welds due to the existence of higher quantity of δ-ferrite. Higher hardness in HAZ is observed in CMF assisted welds due to presence of finer grains.
- The UTS is increased by 59% on an average and higher elongations are achieved in CMF influenced welds.
- Fracture morphology of the joint represents the amount of energy absorbed in the weld joint is high for CMF assisted welds.

- In dissimilar welding, full depth of penetration is achieved for all the process parameters settings except for the lower heat inputs in conventional welding. Weld bead width is reduced by a minimal of 4% in CMF assisted welds.
- In dissimilar welding, due to the difference in thermal conductivity of the base materials, SS 304 material heats faster and melts even before the melting of LCS which contributes to the formation of initial molten pool in dissimilar welding.
- Finer grains are observed in the LCS side and narrower HAZ are observed in the SS 304 side under the influence of CMF. With an increase in heat input, grain size become larger in both the cases.
- With the application of CMF, the homogenous distribution of alloying elements is observed leading to improvement in Cr, Ni elements in LCS side of the FZ.
- Significantly higher hardness in the FZ followed by HAZ and base metal are observed in LCS side whereas slightly higher hardness in the HAZ followed by FZ are observed in SS 304 side.
- UTS is increased by only 4% in CMF assisted welds. Fracture morphology of the weld joint represents the amount of energy absorbed in CMF assisted welds is higher compared to normal welds.

8.2 Future scopes of the present work

The research work presented in this thesis deals with the constriction of arc in GTAW process using a certain magnetic field configuration. The constriction of arc also increases the energy density within the arc. With and without the assistance of magnetic field, both LCS and SS 304 plates of 3 mm thickness are welded and studied with a special emphasis on mechanical characteristics and microstructural changes. For the same amount of heat input, under the influence of CMF, improvements in the weldment are observed. However, the work presented here can be expanded in the following areas:

- In this research, magnets are arranged in a cusp magnetic field configuration. Further investigation can be conducted to explore various other configurations to constrict the arc plasma.
- Welding of thicker materials in single pass can be considered for further experimental investigations as energy density increases in magnetic assisted welding, which will reduce the possible welding defects and production cost.

- Numerical modelling of arc plasma interaction with the assisted magnetic fields is needed to get more insights into the complex thermal phenomena and behavior of the arc plasma.
- External magnetic fields play major role in controlling the microstructural of the weldment. Therefore, the current work can be extended further for welding different materials such as duplex stainless steels, Aluminum alloys, etc.
- The developed magnetic field configurations can be tested in other welding processes such as metal inert gas welding, laser welding, and plasma arc welding to achieve better weldments.

REFERENCES

[1] DebRoy, T., & David SA. Physical processes in fusion welding. Rev Mod Phys 1995;67.

[2] S. A. David and T. DebRoy. Current issues and problems in welding science. Science (80-) 1992;257:497–502.

[3] Unnikrishnan R, Idury KSNS, Ismail TP, Bhadauria A, Shekhawat SK, Khatirkar RK, et al. Effect of heat input on the microstructure, residual stresses and corrosion resistance of 304l austenitic stainless steel weldments. Mater Charact 2014;93:10–23. https://doi.org/10.1016/j.matchar.2014.03.013.

[4] Saha S, Mukherjee M, Pal TK. Microstructure, Texture, and Mechanical Property Analysis of Gas Metal Arc Welded AISI 304 Austenitic Stainless Steel. J Mater Eng Perform 2015;24:1125–39. https://doi.org/10.1007/s11665-014-1374-0.

[5] Kou S. Welding metallurgy, second edition. A Wiley-Interscience publication; 2002.

[6] Sen R, Choudhury SP, Kumar R, Panda A. A comprehensive review on the feasibility study of metal inert gas welding. Mater Today Proc 2018;5:17792–801. https://doi.org/10.1016/j.matpr.2018.06.104.

[7] Eroğlu M, Aksoy M, Orhan N. Effect of coarse initial grain size on microstructure and mechanical properties of weld metal and HAZ of a low carbon steel. Mater Sci Eng A 2002;269:59–66. https://doi.org/10.1016/s0921-5093(99)00137-9.

[8] Kumar C, Das M. Exploration of Parametric Effect on Fiber Laser Weldments of SS-316L by Response Surface Method. J Mater Eng Perform 2021;30:4583–603. https://doi.org/10.1007/s11665-021-05761-w.

[9] Siddaiah A, Singh BK, Mastanaiah P. Prediction and optimization of weld bead geometry for electron beam welding of AISI 304 stainless steel. Int J Adv Manuf Technol 2017;89:27–43. https://doi.org/10.1007/s00170-016-9046-x.

[10] Choudhury B, Chandrasekaran M. Study on Gas Tungsten Arc Welding Characteristics of Nickel based Aerospace Alloys. Mater Today Proc 2018;5:7337–45. https://doi.org/10.1016/j.matpr.2017.11.403.

[11] Xiao L, Fan D, Huang J. Tungsten cathode-arc plasma-weld pool interaction in the magnetically rotated or deflected gas tungsten arc welding configuration. J Manuf Process 2018;32:127–37. https://doi.org/10.1016/j.jmapro.2018.01.026.

[12] Feng Y, Luo Z, Liu Z, Li Y, Luo Y, Huang Y. Keyhole gas tungsten arc welding of AISI 316L stainless steel. Mater Des 2015;85:24–31. https://doi.org/10.1016/j.matdes.2015.07.011.

[13] Khorrami MS, Mostafaei MA, Pouraliakbar H. Materials Science & Engineering A Study on microstructure and mechanical characteristics of low-carbon steel and ferritic stainless steel joints. Mater Sci Eng A 2014;608:35–45. https://doi.org/10.1016/j.msea.2014.04.065.

[14] Chigondo M, Chigondo F. Recent Natural Corrosion Inhibitors for Mild Steel: An Overview. J Chem 2016;2016. https://doi.org/10.1155/2016/6208937.

[15] H L, R S. Understanding the Adsorption of Quinoxaline Derivatives as Corrosion Inhibitors for Mild Steel in Acidic Medium: Experimental, Theoretical and Molecular

Dynamic Simulation Studies. J Steel Struct Constr 2016;2. https://doi.org/10.4172/2472-0437.1000111.

[16] Chen R, Jiang P, Shao X, Mi G, Wang C, Geng S. Improvement of low-temperature impact toughness for 304 weld joint produced by laser-MIG hybrid welding under magnetic fi eld. J Mater Process Tech 2017;247:306–14. https://doi.org/10.1016/j.jmatprotec.2017.04.004.

[17] Chen R, Jiang P, Shao X, Mi G, Wang C. Short Communication E ff ect of magnetic fi eld applied during laser-arc hybrid welding in improving the pitting resistance of the welded zone in austenitic stainless steel. Corros Sci 2017;126:385–91. https://doi.org/10.1016/j.corsci.2017.07.019.

[18] Mahajan S, Biradar NS, Raman R, Mishra S. Effect of mechanical arc oscillation on the grain structure of mild steel weld metal. Trans Indian Inst Met 2012;65:171–7. https://doi.org/10.1007/s12666-012-0118-9.

[19] Gharibshahiyan E, Raouf AH, Parvin N, Rahimian M. The effect of microstructure on hardness and toughness of low carbon welded steel using inert gas welding. Mater Des 2011;32:2042–8. https://doi.org/10.1016/j.matdes.2010.11.056.

[20] Yan J, Gao M, Ã XZ. Study on microstructure and mechanical properties of 304 stainless steel joints by TIG , laser and laser - TIG hybrid welding. Opt Lasers Eng 2010;48:512–7. https://doi.org/10.1016/j.optlaseng.2009.08.009.

[21] Shankar V, Gill TPS, Mannan SL, Sundarlsan S. Solidification cracking in austenitic stainless steel welds. Sadhana - Acad Proc Eng Sci 2003;28:359–82. https://doi.org/10.1007/BF02706438.

[22] Shyu SW, Huang HY, Tseng KH, Chou CP. Study of the performance of stainless steel A-TIG welds. J Mater Eng Perform 2008;17:193–201. https://doi.org/10.1007/s11665-007-9139-7.

[23] Wu H, Chang Y, Mei Q, Liu D, Liu D. Research advances in high-energy TIG arc welding. Int J Adv Manuf Technol 2019;104:391–410. https://doi.org/https://doi.org/10.1007/s00170-019-03918-5.

[24] Yelamasetti B, Vardhan TV, Ramana GV. Study of metallurgical changes and mechanical properties of dissimilar weldments developed by interpulse current TIG welding technique. Proc Inst Mech Eng Part C J Mech Eng Sci 2021;235:2985–97. https://doi.org/10.1177/0954406220960780.

[25] Nomura K, Ogino Y, Hirata Y. Shape control of TIG arc plasma by cusp-type magnetic field with permanent magnet 2012:37–41. https://doi.org/10.1080/09507116.2011.592691.

[26] Rosado-Carrasco J, Krupp U, López-Morelos VH, Giertler A, García-Rentería MA G-SJ. Effect of a magnetic field applied during fusion welding on the fatigue damage of 2205 duplex stainless steel joints. Int J Fatigue 2019;121. https://doi.org/10.1016/j.ijfatigue.2018.12.022.

[27] Curiel FF, García R, López VH, García MA, Lemus J. Transmission electron microscopy in the heat affected zone of an AISI 304 austenitic stainless steel welded with the application of a magnetic field of low intensity. Mater Trans 2013;54:122–5. https://doi.org/10.2320/matertrans.M2012260.

[28] Lin-Cun L W-DX. Effect of an axial magnetic field on a DC argon arc. Chinese Phys B 2008;17:649–54. https://doi.org/10.1088/1674-1056/17/2/048.

[29] Jian L, Zongxiang Y, Keliang X. Anti-gravity gradient unique arc behavior in the longitudinal electric magnetic field hybrid tungsten inert gas arc welding. Int J Adv Manuf Technol 2016:647–61. https://doi.org/10.1007/s00170-015-7728-4.

[30] Chen T, Xiaoning Z, Bai B, Xu Z, Wang C, Xia W. Numerical Study of DC Argon Arc with Axial Magnetic Fields. Plasma Chem Plasma Process 2015;35:61–74. https://doi.org/10.1007/s11090-014-9592-7.

[31] Lin ZQ, Li YB, Wang YS, Chen GL. Numerical analysis of a moving gas tungsten arc weld pool with an external longitudinal magnetic field applied. Int J Adv Manuf Technol 2005;27:288–95. https://doi.org/10.1007/s00170-004-2194-4.

[32] Sun Q, Wang J, Cai C, Li Q, Feng J. Optimization of magnetic arc oscillation system by using double magnetic pole to TIG narrow gap welding. Int J Adv Manuf Technol 2016;86:761–7. https://doi.org/10.1007/s00170-015-8214-8.

[33] Chen R, Wang C, Jiang P, Shao X, Zhao Z, Gao Z, et al. Effect of axial magnetic field in the laser beam welding of stainless steel to aluminum alloy. Mater Des 2016;109:146–52. https://doi.org/10.1016/j.matdes.2016.07.064.

[34] Liu S, Liu ZM, Zhao XC, Fan XG. Influence of cusp magnetic field configuration on K-TIG welding arc penetration behavior. J Manuf Process 2020;53:229–37. https://doi.org/10.1016/j.jmapro.2020.02.027.

[35] Choquet I, Degond P, Lucquin-Desreux B. A hierarchy of diffusion models for partially ionized plasmas. 2007.

[36] Fridman A, Kennedy LA. Plasma physics and engineering. CRC press; 2021.

[37] Kumar S, Shahi AS. On the influence of welding stainless steel on microstructural development and mechanical performance. Mater Manuf Process 2014;29:894–902. https://doi.org/10.1080/10426914.2013.792421.

[38] Kumar S, Shahi AS. Effect of heat input on the microstructure and mechanical properties of gas tungsten arc welded AISI 304 stainless steel joints. Mater Des 2011;32:3617–23. https://doi.org/10.1016/j.matdes.2011.02.017.

[39] Short AB. Gas tungsten arc welding of α + β titanium alloys: A review. Mater Sci Technol 2009;25:309–24. https://doi.org/10.1179/174328408X389463.

[40] Zhou W, Chew KG. Effect of welding on impact toughness of butt-joints in a titanium alloy 2003;347:180–5.

[41] Ram GDJ, Reddy AV, Rao KP, Reddy GM. Control of laves phase in inconel 718 GTA welds with current pulsing. Sci Technol Weld Join 2004;9:390–8. https://doi.org/10.1179/136217104225021788.

[42] Cortés R, Barragán ER, López VH, Ambriz RR, Jaramillo D. Mechanical properties of Inconel 718 welds performed by gas tungsten arc welding. Int J Adv Manuf Technol 2018;94:3949–61. https://doi.org/10.1007/s00170-017-1128-x.

[43] Lin HL, Wu TM. Effects of activating flux on weld bead geometry of inconel 718 alloy TIG welds. Mater Manuf Process 2012;27:1457–61.

https://doi.org/10.1080/10426914.2012.677914.

[44] Kumar R, Anant R, Ghosh PK, Kumar A, Agrawal BP. Influence of PC-GTAW Parameters on the Microstructural and Mechanical Properties of Thin AISI 1008 Steel Joints. J Mater Eng Perform 2016;25:3756–65. https://doi.org/10.1007/s11665-016-2211-4.

[45] Vargas-Arista B, Angeles-Chavez C, Albiter A, Hallen JM. Metallurgical investigation of the aging process on tensile fracture welded joints in pipeline steel. Mater Charact 2009;60:1561–8. https://doi.org/10.1016/j.matchar.2009.09.007.

[46] Sahin M. Evaluation of the joint-interface properties of austenitic-stainless steels (AISI 304) joined by friction welding. Mater Des 2007;28:2244–50.

[47] Eroğlu M, Aksoy M, Orhan N. Effect of coarse initial grain size on microstructure and mechanical properties of weld metal and HAZ of a low carbon steel. Mater Sci Eng A 1999;269:59–66. https://doi.org/10.1016/s0921-5093(99)00137-9.

[48] Curiel FF, García R, López VH, González-Sánchez J. Effect of magnetic field applied during gas metal arc welding on the resistance to localised corrosion of the heat affected zone in AISI 304 stainless steel. Corros Sci 2011;53:2393–9. https://doi.org/10.1016/j.corsci.2011.03.022.

[49] Du CW, Li XG, Liang P, Liu ZY, Jia GF, Cheng YF. Effects of Microstructure on Corrosion of X70 Pipe Steel in an Alkaline Soil. J Mater Eng Perform 2009;18:216–20. https://doi.org/10.1007/s11665-008-9280-y.

[50] Her-Hsiung Huang, Wen-Ta Tsai J-TL. The influences of microstructure and composition on the electrochemical behavior of a516 steel weldment. Corros Sci 1994;36:1027–38.

[51] Mostafa Alizadeh SB. The influence of microstructure on the protective properties of the corrosion product layer generated on the welded API X70 steel in chloride solution. Corros Sci 2013;70:170–9.

[52] K.M. Deen, R. Ahmad, I.H. Khan ZF. Microstructural study and electrochemical behavior of low alloy steel weldment. Mater Des 2010;31:3051–5.

[53] Deen KM, Ahmad R, Khan IH, Farahat Z. Microstructural study and electrochemical behavior of low alloy steel weldment. Mater Des 2010;31:3051–5. https://doi.org/10.1016/j.matdes.2010.01.025.

[54] Esfahani MN, Coupland J, Marimuthu S. Microstructure and mechanical properties of a laser welded low carbon-stainless steel joint. J Mater Process Technol 2014;214:2941–8. https://doi.org/10.1016/j.jmatprotec.2014.07.001.

[55] Tiwari A, Singh P, Pankaj P, Biswas P, Kore SD, Pal S. Effect of Tool Offset and Rotational Speed in Dissimilar Friction Stir Welding of AISI 304 Stainless Steel and Mild Steel. J Mater Eng Perform 2019;28:6365–79. https://doi.org/10.1007/s11665-019-04362-y.

[56] John Wily & Sons. Welding metallurgy and weldability of steels. New Jersey: 2005.

[57] Wang C, Yu Y, Yu J, Zhang Y, Zhao Y, Yuan Q. Microstructure evolution and corrosion behavior of dissimilar 304/430 stainless steel welded joints. J Manuf Process 2020;50:183–91. https://doi.org/10.1016/j.jmapro.2019.12.015.

[58] Jafarzadegan M, Abdollah-zadeh A, Feng AH, Saeid T, Shen J, Assadi H. Microstructure and Mechanical Properties of a Dissimilar Friction Stir Weld between Austenitic Stainless Steel and Low Carbon Steel. J Mater Sci Technol 2013;29:367–72. https://doi.org/10.1016/j.jmst.2013.02.008.

[59] Wang, Hongduo; Wang, Kuaishe; Wang, Wen; Huang, Liying; Peng, Pai; Yu H. Materials Characterization Microstructure and Mechanical Properties of Dissimilar Friction Stir Welded Type 304 Austenitic Stainless Steel to Q235 Low Carbon Steel. Mater Charact 2019;155.

[60] Kumar Singh D, Sahoo G, Basu R, Sharma V, Mohtadi-Bonab MA. Investigation on the microstructure—mechanical property correlation in dissimilar steel welds of stainless steel SS 304 and medium carbon steel EN 8. J Manuf Process 2018;36:281–92. https://doi.org/10.1016/j.jmapro.2018.10.018.

[61] Lundin CD. Dissimilar Metal Welds-Transition Joints Literature Review Emphasis is on carbon migration, the stress/strain state of welds, and transition joint failure mechanisms. Weld Res Suppl 1982;61:58–63.

[62] KLUEH RL, KING JF. Austenitic Stainless Steel-Ferritic Steel Weld Joint Failures. Weld J (Miami Fla) 1982;V 61:302–11.

[63] Pouraliakbar H, Hamedi M, Kokabi AH, Nazari A. Designing of CK45 carbon steel and aisi 304 stainless steel dissimilar welds. Mater Res 2014;17:106–14. https://doi.org/10.1590/S1516-14392013005000170.

[64] Lee, T. S. et al. Influence of welding parameters on microstructure and mechanical properties of stainless steel to low carbon steel GTAW dissimilar welds. Mater Des 2010;31:1113–21.

[65] H. Xu, M.J. Xu, C. Yu, H. Lu, X. Wei, J.M. Chen JJX. Effect of the microstructure in unmixed zone on corrosion behavior of 439 tube/308L tube-sheet welding joint. J Mater Process Technol 2017;240:162–7.

[66] Jayant Gopal Thakare, Chandan Pandey, Manas Mohan Mahapatra, Rahul S. Mulik. An assessment for mechanical and microstructure behavior of dissimilar material welded joint between nuclear grade martensitic P91 and austenitic SS304 L steel. J Manuf Process 2019;48:249–59.

[67] Lohse M, Füssel U, Schuster H, Friedel J, Schnick M. Keyhole welding with CF-TIG (cathode focussed GTA). Weld World 2013;57:735–41. https://doi.org/10.1007/s40194-013-0074-y.

[68] Fei Z, Pan Z, Cuiuri D, Li H, Wu B, Su L. Improving the weld microstructure and material properties of K-TIG welded armour steel joint using filler material. Int J Adv Manuf Technol 2019;100:1931–44. https://doi.org/10.1007/s00170-018-2787-y.

[69] Huang Y, Luo Z, Lei Y, Ao S, Shan H, Zhang Y. Dissimilar joining of AISI 304/Q345 steels in keyhole tungsten inert gas welding process. Int J Adv Manuf Technol 2018;96:4041–9. https://doi.org/10.1007/s00170-018-1791-6.

[70] Rosellini C, Jarvis L. The keyhole TIG welding process: A valid alternative for valuable metal joints. Weld Int 2009;23:616–21. https://doi.org/10.1080/09507110802543237.

[71] Morisada Y, Fujii H, Inagaki F, Kamai M. Development of high frequency tungsten inert gas welding method. Mater Des 2013;44:12–6.

https://doi.org/10.1016/j.matdes.2012.07.054.

[72] Yuan H, Lin S, Yang C, Fan C, Wang S. Microstructure and porosity analysis in ultrasonic assisted TIG welding of 2014 aluminum alloy. China Weld (English Ed 2011;20:39–43.

[73] He LB, Li LM, Hao HW, Wu MS, Zhou RL. Grain refinement and high performance of titanium alloy joint using arc-ultrasonic gas tungsten arc welding. Sci Technol Weld Join 2006;11:72–4. https://doi.org/10.1179/174329306X77083.

[74] Chen X, Shen Z, Wang J, Chen J, Lei Y, Huang Q. Effects of an ultrasonically excited TIG arc on CLAM steel weld joints. Int J Adv Manuf Technol 2012;60:537–44. https://doi.org/10.1007/s00170-011-3611-0.

[75] Leng, X., Zhang, G., & Wu L. The characteristic of twin-electrode TIG coupling arc pressure. J Phys D Appl Phys 2006;39.

[76] Schwedersky MB, Gonçalves e Silva RH, Dutra JC, Reisgen U, Willms K. Arc characteristic evaluation of the double-electrode GTAW process using high current values. Int J Adv Manuf Technol 2018;98:929–36. https://doi.org/10.1007/s00170-018-2344-8.

[77] Kumar, S. M., & Shanmugam NS. Studies on the weldability, mechanical properties and microstructural characterization of activated flux TIG welding of AISI 321 austenitic stainless steel. Mater Res Express 2018;5.

[78] Vidyarthy RS, Dwivedi DK. Activating flux tungsten inert gas welding for enhanced weld penetration. J Manuf Process 2016;22:211–28. https://doi.org/10.1016/j.jmapro.2016.03.012.

[79] Venkatesan G, Muthupandi V, Justine J. Activated TIG welding of AISI 304L using mono- and tri-component fluxes. Int J Adv Manuf Technol 2017;93:329–36. https://doi.org/10.1007/s00170-016-9002-9.

[80] Qi BJ, Yang MX, Cong BQ, Liu FJ. The effect of arc behavior on weld geometry by high-frequency pulse GTAW process with 0Cr18Ni9Ti stainless steel. Int J Adv Manuf Technol 2013;66:1545–53. https://doi.org/10.1007/s00170-012-4438-z.

[81] Wu H, Chang Y, Guan Z, Babkin A, Lee B. Arc shape and microstructural analysis of TIG welding with an alternating cusp-shaped magnetic field. J Mater Process Technol 2021;289:116912. https://doi.org/10.1016/j.jmatprotec.2020.116912.

[82] Shakya P, Singh K, Arya HK. Influence of Magnets on Arc Shape and Bead Geometry in Gas Tungsten Arc Welding. Mater Manuf Process 2022;00:1–8. https://doi.org/10.1080/10426914.2022.2075890.

[83] Liu Z, Chen S, Yuan X, Zuo A, Zhang T, Luo Z. Magnetic-enhanced keyhole TIG welding process. Int J Adv Manuf Technol 2018;99:275–85. https://doi.org/10.1007/s00170-018-2501-0.

[84] Jiuchun, Y. A. N., Chunli, Y. A. N. G., & Huijie LIU. overview on ultrasonic-assisted welding and its scientific issues. J Mech Eng 2015;51:41–9.

[85] Dey HC, Albert SK, Bhaduri AK, Mudali UK. Activated flux TIG welding of titanium. Weld World 2013;57:903–12. https://doi.org/10.1007/s40194-013-0084-9.

[86] Gao X, Dong J, Han X. Effect of RE2O3 (RE = La, Ce) fluxes on A-TIG welding of Ti6Al4V. Int J Adv Manuf Technol 2017;91:1181–8. https://doi.org/10.1007/s00170-016-9826-3.

[87] Tseng K, Hsu C. Journal of Materials Processing Technology Performance of activated TIG process in austenitic stainless steel welds. J Mater Process Tech 2011;211:503–12. https://doi.org/10.1016/j.jmatprotec.2010.11.003.

[88] Huang HY, Shyu SW, Tseng KH, Chou CP, Huang HY, Shyu SW, et al. Evaluation of TIG flux welding on the characteristics of stainless steel Evaluation of TIG flux welding on the characteristics of stainless steel 2013;1718. https://doi.org/10.1179/174329305X48329.

[89] V. Balasubramanian VR& GMR. Effect of pulsed current welding on mechanical properties of high strength aluminum alloy. Int J Adv Manuf Technol 2008:254–62. https://doi.org/10.1007/s00170-006-0848-0.

[90] Tse HC, Man HC, Yue TM. Effect of magnetic field on plasma control during CO 2 laser 1999;31:363–8.

[91] Lim YC, Yu X, Cho JH, Sosa J, Farson DF, Babu SS, et al. Effect of magnetic stirring on grain structure refinement : Part 1 – Autogenous nickel alloy welds Effect of magnetic stirring on grain structure refinement Part 1 – Autogenous nickel alloy welds 2013;1718. https://doi.org/10.1179/136217110X12720264008277.

[92] Guan ZQ, Zhang HX, Liu XG, Babkin A, Chang YL. Effect of magnetic field frequency on the shape of GMAW welding arc and weld microstructure properties. Mater Res Express 2019;6.

[93] P.E.Secker, A.E.Guile. Arc Movement in a Transverse Magnetic Field at Atmospheric Pressure. Inst Electr Eng 1959;106:311–20.

[94] Peck WF. Physics of the Welding Arc in Magnetic Fields. The Ohio State University, 1996.

[95] Schmidt, H. P., & Speckhofer G. Experimental and theoretical investigation of high pressure arcs Part II: The magnetically deflected arc column (3D-modeling). IEEE Trans Plasma Sci 1996;24.

[96] Anders A, Yushkov GY. Ion flux from vacuum arc cathode spots in the absence and presence of a magnetic field. J Appl Phys 2002;91:4824–32. https://doi.org/10.1063/1.1459619.

[97] Li Y, Lin Z, Chen G, Wang Y, Xi S. Study on moving GTA weld pool in an externally applied longitudinal magnetic field with experimental and finite element methods. Model Simul Mater Sci Eng 2002;10:781–98. https://doi.org/10.1088/0965-0393/10/6/311.

[98] Matsuda, F., Nakata, K., Miyanaga, Y., Kayano, T., & Tsukamoto K. Effect of Electromagnetic Stirring on Weld Solidification Structure of Aluminum Alloys (Report II) : Investigation on GTA in DCSP Weld Metal of 8mm Thick Plate. Trans JWRI (Japanese Weld Res Institute) 1978;7:181–93.

[99] Matsuda, F., Nakagawa, H., Nakata, K., & Ayani R. Effect of electromagnetic stirring on weld solidification structure of aluminum alloys (Report I): Investigation on GTA weld metal of thin sheet. Trans JWRI 1978;7:111–27.

[100] Matsuda, F., Nakata, K., & Sano N. Effect of electromagnetic stirring on weld solidification structure of austenitic stainless steels (materials, metallurgy & weldability). Trans JWRI (Japanese Weld Res Institute) 1986;15:327–38.

[101] Ouden G Den, Vink WJP. Effect of Electromagnetic Stirring on GTA Welds in Austenitic Stainless Steel 1990:52–9.

[102] Chen R, Wang C, Jiang P, Shao X, Zhao Z, Gao Z, et al. Effect of axial magnetic fi eld in the laser beam welding of stainless steel to aluminum alloy. JMADE 2016;109:146–52. https://doi.org/10.1016/j.matdes.2016.07.064.

[103] García-Rentería MA, López-Morelos VH, González-Sánchez J, García-Hernández R, Dzib-Pérez L, Curiel-López FF. Effect of electromagnetic interaction during fusion welding of AISI 2205 duplex stainless steel on the corrosion resistance. Appl Surf Sci 2017;396:1187–200. https://doi.org/10.1016/j.apsusc.2016.11.109.

[104] Chen R, Jiang P, Shao X, Mi G, Wang C. Effect of static magnetic field on microstructures and mechanical properties of laser-MIG hybrid welding for 304 stainless steel. Int J Adv Manuf Technol 2017. https://doi.org/10.1007/s00170-017-0006-x.

[105] Liu YB, Sun QJ, Wang H, Zhang HM, Cai SJ, Feng JC, et al. Effect of the axial external magnetic field on copper / aluminium arc weld joining Effect of the axial external magnetic fi eld on copper / aluminium arc weld joining 2016;1718. https://doi.org/10.1080/13621718.2015.1125406.

[106] Baskoro AS, Fauzian A, Basalamah H, Kiswanto G, Winarto W. Improving weld penetration by employing of magnetic poles' configurations to an autogenous tungsten inert gas (TIG) welding. Int J Adv Manuf Technol 2018;99:1603–13. https://doi.org/10.1007/s00170-018-2552-2.

[107] Chen R, Jiang P, Shao X, Mi G, Wang C. Effect of static magnetic field on microstructures and mechanical properties of laser-MIG hybrid welding for 304 stainless steel. Int J Adv Manuf Technol 2017;91:3437–47. https://doi.org/10.1007/s00170-017-0006-x.

[108] Wang J, Sun Q, Feng J, Wang S, Zhao H. Characteristics of welding and arc pressure in TIG narrow gap welding using novel magnetic arc oscillation. Int J Adv Manuf Technol 2017;90:413–20. https://doi.org/10.1007/s00170-016-9407-5.

[109] Wang J, Sun Q, Feng J, Wang S, Zhao H. Characteristics of welding and arc pressure in TIG narrow gap welding using novel magnetic arc oscillation. Int J Adv Manuf Technol 2017;90:413–20. https://doi.org/10.1007/s00170-016-9407-5.

[110] Chang Y, Liu M, Lu L, Babkin AS, Lee BY. The influence of longitudinal magnetic field on the CO2 arc shape. Plasma Sci Technol 2015;17:321–6. https://doi.org/10.1088/1009-0630/17/4/11.

[111] Pant, Pallavi and Verma, Jagesvar and Taiwade, Ravindra V and Prabhakar KP. Influence of advanced laser-arc hybrid welding and conventional MIG process on microstructure, mechanical properties and corrosion resistance of dissimilar joints. Mater Res Express 2018;5:066558.

[112] Fattahi M, Nabhani N, Vaezi MR, Rahimi E. Improvement of impact toughness of AWS E6010 weld metal by adding TiO2 nanoparticles to the electrode coating. Mater Sci Eng

A 2011;528:8031–9. https://doi.org/10.1016/j.msea.2011.07.035.

[113] Alok A, Das M. White layer analysis of hard turned AISI 52100 steel with the fresh tip of newly developed HSN2 coated insert. J Manuf Process 2019;46:16–25. https://doi.org/10.1016/j.jmapro.2019.08.016.

[114] Youdelis, W. V., Colton, D. R., & Cahoon J. On the theory of diffusion in a magnetic field. Can J Phys 1964;42:2217–37.

[115] Gao M, Zeng X, Yan J, Hu Q. Microstructure characteristics of laser-MIG hybrid welded mild steel. Appl Surf Sci 2008;254:5715–21. https://doi.org/10.1016/j.apsusc.2008.03.070.

[116] Zhengwu Z, Xiuquan M, Chunming W, Gaoyang M. Grain refinement and orientation alternation of 10 mm 316L welds prepared by magnetic field assisted narrow gap laser-MIG hybrid welding. Mater Charact 2020;164. https://doi.org/10.1016/j.matchar.2020.110311.

[117] Kwok CT, Fong SL, Cheng FT, Man HC. Pitting and galvanic corrosion behavior of laser-welded stainless steels. J Mater Process Technol 2006;176:168–78. https://doi.org/10.1016/j.jmatprotec.2006.03.128.

[118] Curiel FF, García R, López VH, González-Sánchez J. Effect of magnetic field applied during gas metal arc welding on the resistance to localised corrosion of the heat affected zone in AISI 304 stainless steel. Corros Sci 2011. https://doi.org/10.1016/j.corsci.2011.03.022.

[119] Zhengwu Z, Xiuquan M, Chunming W, Gaoyang M. Grain refinement and orientation alternation of 10 mm 316L welds prepared by magnetic field assisted narrow gap laser-MIG hybrid welding. Mater Charact 2020;164. https://doi.org/10.1016/j.matchar.2020.110311.

[120] Mirshekari GR, Tavakoli E, Atapour M, Sadeghian B. Microstructure and corrosion behavior of multipass gas tungsten arc welded 304L stainless steel. Mater Des 2014;55:905–11. https://doi.org/10.1016/j.matdes.2013.10.064.

[121] Alok A, Das M. White layer analysis of hard turned AISI 52100 steel with the fresh tip of newly developed HSN 2 coated insert. J Manuf Process 2019;46:16–25. https://doi.org/10.1016/j.jmapro.2019.08.016.

[122] Sabzi M, Obeydavi A, Anijdan SHM. The effect of joint shape geometry on the microstructural evolution , fracture toughness , and corrosion behavior of the welded joints of a Hadfield Steel. Mech Adv Mater Struct 2019;0:1–11. https://doi.org/10.1080/15376494.2018.1430268.

[123] Sabzi M, Mersagh S. Post weld heat treatment of hypereutectoid had fi eld steel : Characterization and control of microstructure , phase equilibrium , mechanical properties and fracture mode of welding joint. J Manuf Process 2018;34:313–28. https://doi.org/10.1016/j.jmapro.2018.06.009.

[124] Durgaprasad K, Pal S, Das M. Metallurgical and mechanical properties evolution in cusp-magnetic field-assisted GTAW of low carbon steel. Proc Inst Mech Eng Part C J Mech Eng Sci 2022:1–14. https://doi.org/10.1177/09544062221135520.

[125] Biradar NS, Raman R. Grain refinement in Al-Mg-Si alloy TIG welds using transverse mechanical arc oscillation. J Mater Eng Perform 2012;21:2495–502.

https://doi.org/10.1007/s11665-012-0207-2.

[126] M MA, Shrikrishna KA, Sathiya P, Goel S. The impact of heat input on the strength, toughness, microhardness, microstructure and corrosion aspects of friction welded duplex stainless steel joints. J Manuf Process 2015;18:92–106. https://doi.org/10.1016/j.jmapro.2015.01.004.

[127] Lu Y, Jing H, Han Y, Xu L. Effect of Welding Heat Input on the Corrosion Resistance of Carbon Steel Weld Metal. J Mater Eng Perform 2016;25:565–76. https://doi.org/10.1007/s11665-015-1815-4.

[128] Ravi Shankar A, Gopalakrishnan G, Balusamy V, Kamachi Mudali U. Effect of heat input on microstructural changes and corrosion behavior of commercially pure titanium welds in nitric acid medium. J Mater Eng Perform 2009;18:1116–23. https://doi.org/10.1007/s11665-008-9335-0.

[129] Sun QJ, Li JZ, Liu YB, Li BP, Xu PW, Feng JC. Microstructural characterization and mechanical properties of Al/Ti joint welded by CMT method—Assisted hybrid magnetic field. Mater Des 2017. https://doi.org/10.1016/j.matdes.2016.12.025.

LIST OF PUBLICATIONS

International SCI Journal Publication (Published)

- Durgaprasad, K., Pal, S., & Das, M. (2022). Metallurgical and mechanical properties evolution in cusp-magnetic field-assisted GTAW of low carbon steel. *Proceedings of the Institution of Mechanical Engineers, Part C: Journal of Mechanical Engineering Science*, 09544062221135520.
  Durgaprasad, K., Pal, S. & Das, M. Influence of cusp magnetic field on the evolution of metallurgical and mechanical properties in GTAW of SS 304. Int J Adv Manuf Technol 126, 5199–5214 (2023). https://doi.org/10.1007/s00170-023-11441-x

Papers to be published

- Durgaprasad, K., Pal, S., & Das, M. Influence of cusp magnetic field on dissimilar welding of low carbon steels and SS304.
- Durgaprasad, K., Pal, S., & Das, M. Improvement in corrosion characteristics of GTAW 304 stainless steels under the influence of cusp magnetic field.